Synthesis of mono-, bi-, and tri-metallic alloy nanoparticles by co-sputtering onto liquid substrate

ZHU Mingbei

Graduate School of Engineering

Hokkaido University

March 2023

ABSTRACT

Sputtering method is a widely used physical method to synthesize thin films and small NPs on solid or liquid substrates. Compared to traditional chemical reduction method for fabricating NPs, sputtering can synthesize NPs under room temperature. And this method doesn't use toxic reductants or produce by-products. Thus it's a environmentally friendly fabricating approach. Synthesizing alloy NPs by co-sputtering onto liquids enables long time sputtering, breaks the limitations of miscibility gap in bulk phase diagram and makes the obtained NPs controllable by adjusting the sputtering parameters (such as the sputtering current and so on). The particle sizes and compositions can be controlled by adjusting the sputtering currents, sputtering times and so on. As a result, the alloy NPs can be used in various applications. Sputtered Pt NPs can be applied as catalysts in oxygen reduction reaction (ORR). Nevertheless, the high cost and sluggish kinetics of Pt impede the industrial application of Pt catalysts. Alloying Pt with other metals can not only cut the cost but also enhance the catalytic activity of the catalysts. Therefore, using sputtering method to prepare Pt-based alloy NPs is expected to optimize the compositions and maximize the catalytic activity of the catalysts. Furthermore, sputtering can also be used to prepare fluorescence NPs. Fluorescence Au alloy NPs synthesized by co-sputtering can pave the way for the study of diverse applications.

Chapter two firstly synthesized Pt/Ag solid solution alloy NPs smaller than 3 nm with composition in miscibility gap by co-sputtering onto liquid PEG. The sputtering currents didn't affect particle sizes but have obvious impact on compositions and

composition distributions of the alloy NPs. The sizes of NPs sputtered onto PEG were smaller than that on glass while the composition distributions of the NPs in PEG were broader than that on glass. This reveals that PEG hindered the combination of NPs and clusters, resulting in small particle sizes even for long time sputtering and broader composition distributions. Thus, the samples obtained in PEG have the compositions mainly determined by the random atom combination in the vacuum chamber and possibly in initial landing of atom/clusters on the PEG surface.

Chapter three reports about the synthesis of trimetallic CuPt/Ag alloy NPs prepared by co-sputtering onto PEG using a CuPt alloy target and an Ag target. The fine structure analysis reveals that the obtained NPs are trimetallic solid solution alloy. Ag compositions increased with the increase of sputtering currents applied to Ag target while keeping the sputtering currents applied to CuPt target constant. Moreover, it was found that the Cu:Pt atomic ratios of single NPs measured by energy dispersive spectroscopy (EDS) coupled with scanning transmission electron miscroscope (STEM) were lower than the average value of the sputtered NPs dispersed in PEG. This suggests that NPs which are big enough to be checked by STEM-EDS are mainly Pt-rich NPs. The Cu, Ag, and Pt compositions of trimetallic NPs varied in a wide range, indicating random alloy formation. The sputtered trimetallic CuPt/Ag NPs were studied as catalysts in oxygen reduction reaction (ORR), and the catalytic performance is compared with sputtered bimetallic alloy Cu/Pt and Ag/Pt NPs and monometallic Pt NPs. Trimetallic CuPt/Ag NPs showed higher ORR catalytic activities than bimetallic alloy Cu/Pt NPs owing to their better stability and dispersibility on carbon support.

However, the trimetallic alloy NPs performed worse than bimetallic Ag/Pt NPs and Pt NPs. This is caused by Cu oxidation and dissolution of Pt and Cu. Comparable ORR catalytic performance of Ag/Pt NPs (40 atom% Ag) with Pt NPs is thought to come from the synergy between Pt and Ag in bimetallic alloy.

Chapter Four focus on the synthesis of fluorescence Au alloy NPs synthesized by co-sputtering onto PEG with MUA dispersed. The particle sizes and optical properties of the obtained bimetallic alloy NPs were checked and compared with the monometallic fluorescence NPs. For the alloy NPs composed of the same metals, the relationship between particle size and sputtering current applied to metal targets were investigated. And fluorescence wavelengths of the alloy NPs were also compared with their monometallic counterparts. It was found that the NPs with bigger sizes show longer fluorescence wavelength, however, for the alloy NPs with the same particle sizes, the sputtering currents didn't show obvious impact on fluorescence peak position.

Chapter Five summarizes about the research findings and conclusions of the thesis.

Table of contents

1 General Introduction

1.1 Brief introduction of sputtering

Vacuum sputtering is a common fabricating method for synthesizing thin films on solid substrates. The energetic gas ions formed from Ar, O_2, N_2 or H_2 hit the metal targets, to make metal atoms/clusters ejected from the targets.[1-4] The ejected atoms or clusters finally deposit onto the substrate which has been placed in the vacuum sputtering chamber and the gas ions are generated by applying current or voltage to the sputtering chamber.

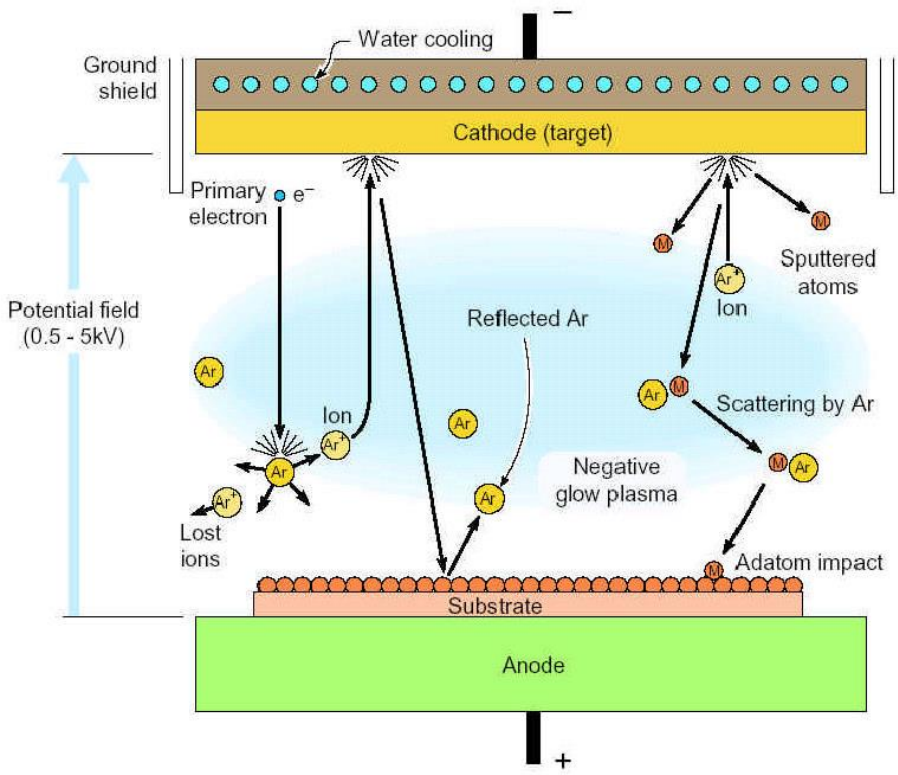

Figure 1.1. Scheme of the sputtering deposition process.

Figure 1.1 illustrates the scheme of the sputtering deposition process.[5] The target

material is bombarded with ions generated from an ionic plasma by applying a negative potential to the magnetrons, that is, producing a voltage between the target material and the grounded substrate plate. When the voltage is applied to the electrodes, the limited number of charge carriers originally exist in the sputtering gas generate a small current. As the applied voltage increases, the current density also increases, resulted from the formation of a high density of charge carriers, such as secondary electrons. While electrons are moving towards the anode (sample), an ion flow is being generated toward the cathode (target). If the voltage is up to the breakdown voltage, this phenomenon will continue to exist. The gas ions generated by collision of electrons and carrier gas will bombard the target and the metal atoms eject. The ejected atoms finally deposit on the substrate.[4,5]

During recent decades, sputtering has developed rapidly for some industrial applications, such as surface coating, functional films and so on.[1,4,6] It's also a traditional way of creating multilayer of metals, metal alloys, and metal oxides.[6-12] Therefore, the sputtering method has attracted much attention around the world due to its wide applications. F. Sanchette et al. used composite targets to sputter Al–TM (TM=Al, Ti or Fe) alloy coatings and investigated the main features in terms of structure, microhardness and open-circuit potential.[6] They discussed the structure–properties relationship of Al-TM systems and arrived at a conclusion that Al-Cr and Al-Ti systems can achieve a good balance between microhardness and low open-circuit potential, however above 10% Fe, Al–Fe alloys cannot be applied as sacrificial coatings.[6] C. Hsu

et at.[13] synthesized ZnO thin film on glass substrates using a RF reactive magnetron sputtering method and discussed the relationship between the plasma characteristics and physical properties of the thin films. They further studied the optical properties of the resulted functional films.[13]

1.2 Sputtering onto liquids

Except for the synthesis of thin films on solid substrates, the sputtering technique can also use liquids as substrates. In 1996, G. Ye et al. reported their first try of sputtering Ag thin film on silicon oil, a liquid substrate.[14] This enlightened a new way to synthesize nanoparticles (NPs) or nanoclusters (NCs) by sputtering onto a liquid substrate, and also attracted much interests of researchers to work on proper liquid substrate as well as the controlling of nanoparticle properties.[4]

Traditionally, NPs were obtained by chemical methods, which was usually to be colloidal synthesis (CS).[2] This method is based on reactions in solution between reactants, so reaction conditions and stabilizing agents are used to control the size and shape of NPs.[15] In terms of managing NP size and permitting a range of applications, chemical synthesis is quite adaptable, which is one of the advantages of chemical methods. However, it generally produces toxic byproducts and low-purity NPs. Unlike chemical methods, sputtering, as a physical method, is a clean methodology to synthesize NPs with high purity. In this case, sputtering onto liquid substrates may offer

an optimized method to control the sizes, shapes and purities of NPs.[16,17] And it allows for long time sputtering. As the development of sputtering technique over a liquid substrate, the choice of liquid also became diverse. Ionic liquids (ILs), silicon oil, vegetable oils and polymer liquids attracted much attention.[2,18-21]

E. Vanecht et al. sputtered Au NPs onto ILs and found that the size limitation of NPs depended on the viscosity and type of the ILs.[18] H. Wender et al. synthesized stable spherical gold nanoparticles (Au NPs) with particle sizes of 2.4 to 3.8 nm by sputtering onto castor oil.[19] R. Brown et al. sputtered Pt NPs onto three ILs and PEG 600 and they emphasized the influence of temperature on particle sizes.[21] The successful synthesis of NPs through sputtering onto liquid substrates proved the possibility of controlling the sizes and shapes of NPs sputtered in liquids and opened up more efficiently methodologies for obtaining high-purity NPs.

1.3 Single-target sputtering of NPs onto liquid

Since after the development of sputtering onto liquid substrates in aspect of the synthesis of metal NPs, the synthesis of alloy NPs by sputtering had also begun to enter researchers' attention. Simultaneous sputtering is one of the sputtering methods to prepare alloy NPs. Torimoto et al. took the first attempt to synthesize Au-Ag alloy NPs through the simultaneous sputter deposition of Au and Ag onto ILs.[22] They used sputtering targets composed of radially-arranged Au and Ag foils, as shown in Figure

1.2 (a). Except for the cases of pure Au or Ag deposition, each domain exhibited a fan shape with a center angle of 30, or 90º. The researchers controlled the chemical compositions and optical properties of the bimetallic Au-Ag NPs by adjusting the area ratio of the metal foils in the sputtering targets.[22] With the same simultaneous sputtering method, the research team continued to synthesize Au-Pt, Au-Pd, and Au-Cu bimetallic alloy NPs using binary sputtering targets.[23-25]

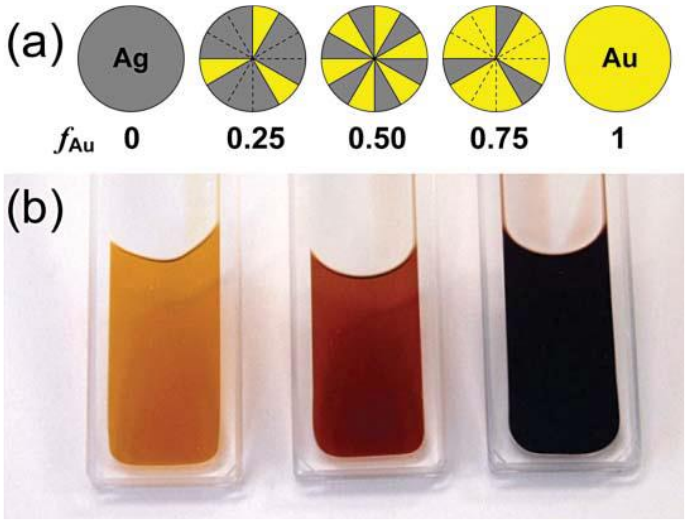

Figure 1.2. (a) Schematic illustrations of Au–Ag foil binary targets having various f_{Au}. (b) Photographs of BMI-PF6 obtained after the sputter deposition of Ag (f_{Au} = 0, left), Au–Ag (f_{Au} = 0.50, center) and Au (f_{Au} = 1, right) nanoparticles. Reproduced with permission from Ref. 22, copyright 2012 The Royal Society of Chemistry.

Except for the simultaneous sputtering, another sputtering method of single-target sputtering, successive sputtering, has also been used to obtain alloy NPs. For example, S. Wang et al. used this one-pot environmentally friendly sputtering method to Ag@Au and Ag@Pd core-shell structured alloy NPs.[26]

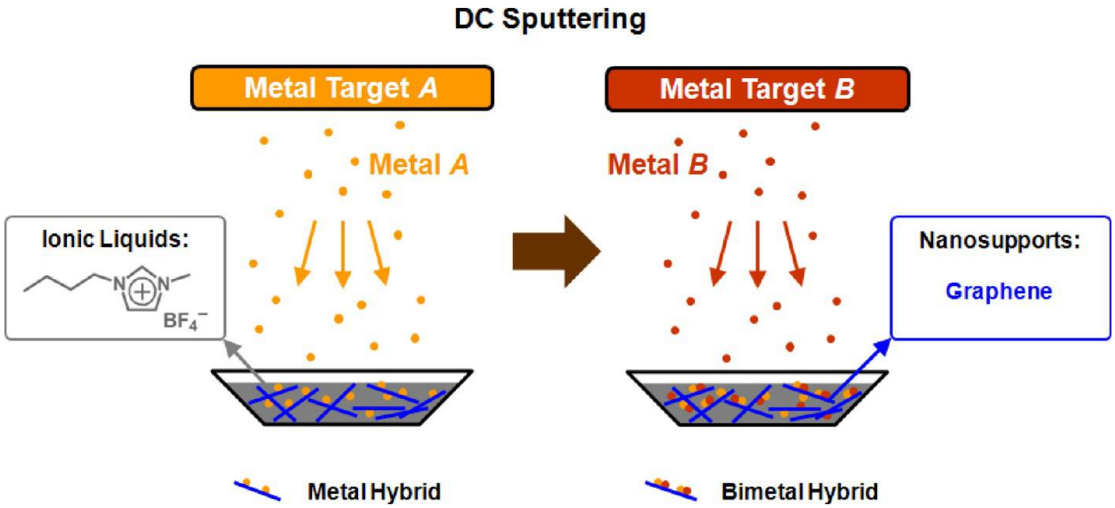

Figure 1.3. Scheme of Preparation Method for Bimetal-NP-Graphene Hybrids: Sputtering Metal A Followed by Sputtering Metal B onto RTILs, in Which Graphene is predispersed. There are neither additives nor byproducts in this simple process. Reproduced with permission from Ref. 26, copyright 2013 The American Chemical Society.

Figure 1.3 illustrates the successive sputtering process for synthesizing core-shell bimetal-nanoparticle (NP)-graphene hybrids. The NPs of A metal are firstly sputtered onto an IL containing graphene powder at room temperature, after which B metal NPs are sputtered under the same sputtering conditions by changing the metal target. The resulting bimetallic NPs have have the core-shell-like structure with a core of A metal and a shell of B metal.[26] Compare with traditional chemical reduction, this successive sputtering technique is absolutely devoid of additives and byproducts, making it environmentally beneficial. The researchers also obtained PdAu bimetallic NPs with small size, high surface density and controlled Pd-to-Au ratio using the same successive

sputtering method.[27] The Pd-to-Au ratio was adjusted by controlling the sputtering time of Au and well stabilized on graphene. The PdAu-NP-graphene hybrids were found to have higher catalytic activity than their monometallic counterparts.

After the synthesis of bimetallic NPs via successive sputtering, S. Wang et al. continued to expand in the field of trimetallic alloy NPs28. They provided this simple physical method for preparing multiwalled carbon nanotubes (CNTs)-PdAu/Pt trimetallic nanoparticles (NPs). To prepare trimetallic PdAu/Pt NPs, a PdAu alloy target was firstly sputtered for 10 min, followed by the sputtering of Pt for 5 min onto the suspension containing PdAu, as shown in Figure 1.4. By modifying the sputtering targets and conditions, this approach enables for predesign and control of the metal compositional ratio. The obtained CNTs-supported PdAu/Pt trimetallic NPs exhibited high electrocatalytic peak current and high stability. Compared to bimetallic NPs and commercial Pt/C catalyst, the results were superior. The stability of the catalytically active Pt surface is improved by adding Au, and the resistance to CO poisoning is improved by adding Pd. This successive sputtering method is a straightforward one for predesigning and tailoring the composition of CNT-supported trimetallic NPs for catalysis and energy applications.

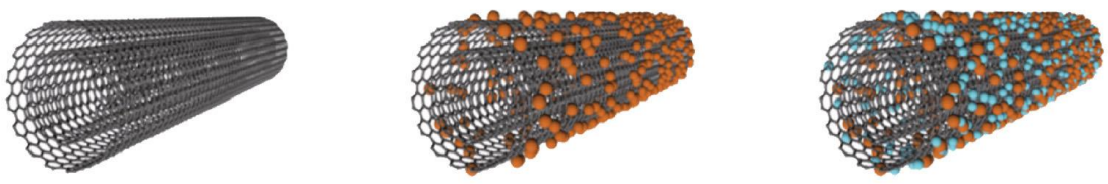

Figure 1.4. Process used to prepare CNTs-PdAu/Pt NPs. Reproduced with permission

from Ref. 28, copyright 2017 Springer.

1.4 Double-target sputtering of alloy NPs onto liquid

To synthesize bi- or trimetallic alloy NPs, using alloy sputtering target or successive sputtering method are common approaches. However, in order to control the compositions of resulted NPs, the alloy target should be designed with different compositions. What's more, for the successive sputtering, the set up of targets also need to be designed. Thus another sputtering method, co-sputtering, was used to synthesize alloy NPs.

Co-sputtering is a sputtering method which uses double-target system. Regardless of the difference in redox potentials of metals or the use of hazardous reductants, double-target sputtering can simultaneously create metal atoms and clusters of two or more metals for creating alloy NPs at room temperature29303132. Co-sputtering enables operation outside of the thermodynamic equilibrium, and appears to be the preferred way for producing alloy NPs with customized compositions without the use of chemical precursors or stabilizing agents30. As a result, this approach may allow for the creation of alloy/bimetal NPs with a wider range of compositions and fine architectures4.

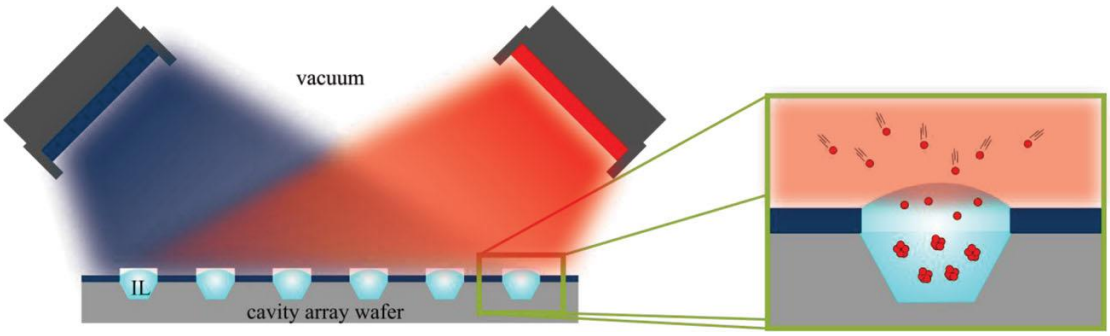

Figure 1.5. schematic (not to scale) of the combinatorial co-deposition from two sputter targets into a cavity array substrate filled with IL. Reproduced from ref. 30, copyright 2014 John Wiley & Sons.

A. Ludwig et al. used co-sputtering method to synthesize Au-Cu binary alloy NPs into an ionic liquid (IL, ($[C_1C_4im][Tf_2N]$) contained in a micromachined cavity array substrate30. Two elemental targets (Cu and Au, purity 99.995 at% and 99.99 at%, respectively) were settled opposite to each other. As shown in Figure 1.5, the target's 28° inclination angle with respect to the substrate results in a nearly linear compositional gradient on the substrate, with higher content of one material at the substrate point closest to the target. A unique substrate was devised, manufactured, and used to realize materials libraries of sputtered NPs in ILs. It comprises of a 301 square cavity array (lateral dimensions: 3 mm 3 mm) etched on a 4-in (100)-oriented Si wafer (1.5 μm thermal SiO_2) with a depth of 300 μm (See Figure 1.6). Before deposition, each of the cavities was filled with 2 μL of the IL. And if a huge amount of NPs of a specific composition were required, the entire cavity array substrate was uniformly covered by rotating the substrate at a rate of 20 rpm. The composition of binary alloy NPs was controlled by adjusting the sputtering parameter. The obtained nanoparticles (NPs) are

tiny (7 nm) and have a limited size distribution, and the size and shape of the NPs change with composition.

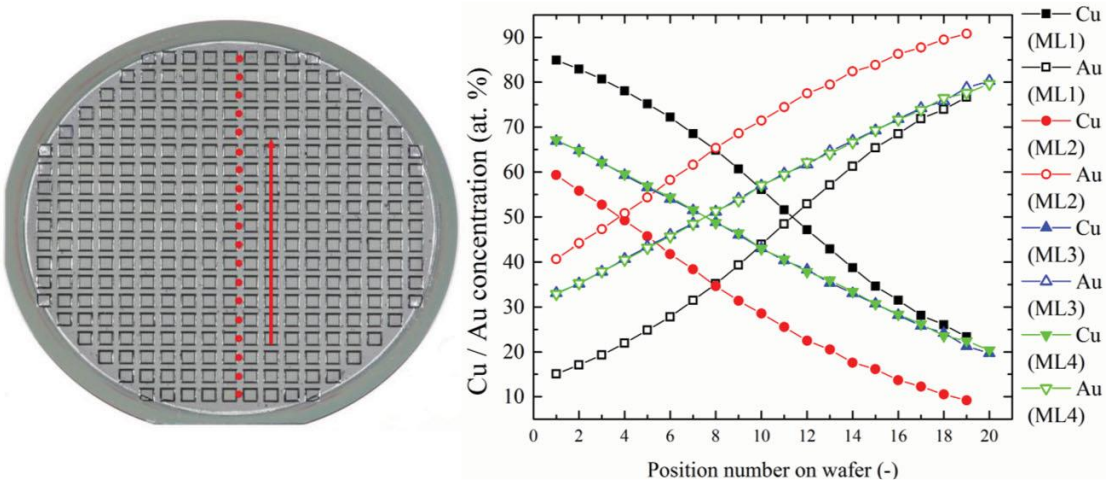

Figure 1.6. Left: Photo of a 4-in cavity array substrate used for the fabrication of NP libraries. The red dots illustrate the measurement points whereas the red arrow illustrates the direction in which the EDX line scan analysis was performed. Right: Results of EDX screening for the four materials libraries. Reproduced from ref. 30, copyright 2014 John Wiley & Sons.

A. Chauvin et al. reported the synthesis of Au/Cu alloy NPs by co-sputtering onto PEEL liquid substrate33. They co-sputtered an Au target and a Cu target which are in confocal geometry. By fixing the electrical power applied to the Cu target and adjusting the one applied to Au target, the average composition of Au in the alloy NPs was varied. The sputtering was carried out under room temperature. The obtained NPs were further annealed by heating for 5 h after 1 month of synthesis, in order to increase their size and stimulate the dealloying of the Au-Cu NPs even further. This method allows for the

manufacturing of very small NPs without the use of toxic chemicals or complicated chemical synthesis pathways, as well as the synthesis of alloy NPs, which can serve as a precursor to the generation of porous NPs.

L. Deng et al. generated Pt/Au alloy nanoparticles (NPs) with a wide composition range by sputtering two independent magnetron sources onto liquid PEG at ambient temperature34. Two metal targets (Pt and Au) were used in the sputtering process, and the sputtering currents and times were controlled. The prepared alloy NPs are face-centered cubic (fcc) structure. They found that the particle size is highly correlated with the compositions. They further investigated the interaction between PEG and NPs using density functional theory (DFT) computations to reveal the formation mechanism. On the one hand, because the calculated adsorption energy of PEG-Pt (0.20 eV) is nearly twice as large as that of PEG-Au (0.12 eV) and the bond length of O-Pt atoms (2.424 Å) is shorter than O-Au (3.133 Å), where the O in PEG is assumed to be coordinated with metal atoms, the PEG molecule adsorbs more favorably on Pt than on Au. On the other hand, the formation energy of Pt atoms is higher than that of Au atoms. As shown in Figure 1.7, the formation energy of a cluster decreases as the number of Au atoms rises in clusters with a fixed number of Pt atoms, whereas the formation energy of a cluster increases as the number of Pt atoms increases in clusters with a fixed number of Au atoms. Thus a NP with more Au atoms tend to grow bigger, on the contrary, a NP with more Pt atoms usually has a smaller size, in order to reduce the formation energy of the NP34. Based on this suggestion, L. Deng et al. proposed a possible formation

process for NPs. The NPs can form when two clusters collide in sections with a higher Au concentration on the surface of the tiny clusters. As a result, Pt on the particle surface will rise as the NP grows34. Due to the strong interaction between Pt and PEG, the NP with more Pt atoms on the surface will stop growing, as shown in Figure 1.8. As a result, even when the sputtering current is changed, particles with the same Pt/ Au ratio grow to equal sizes34.

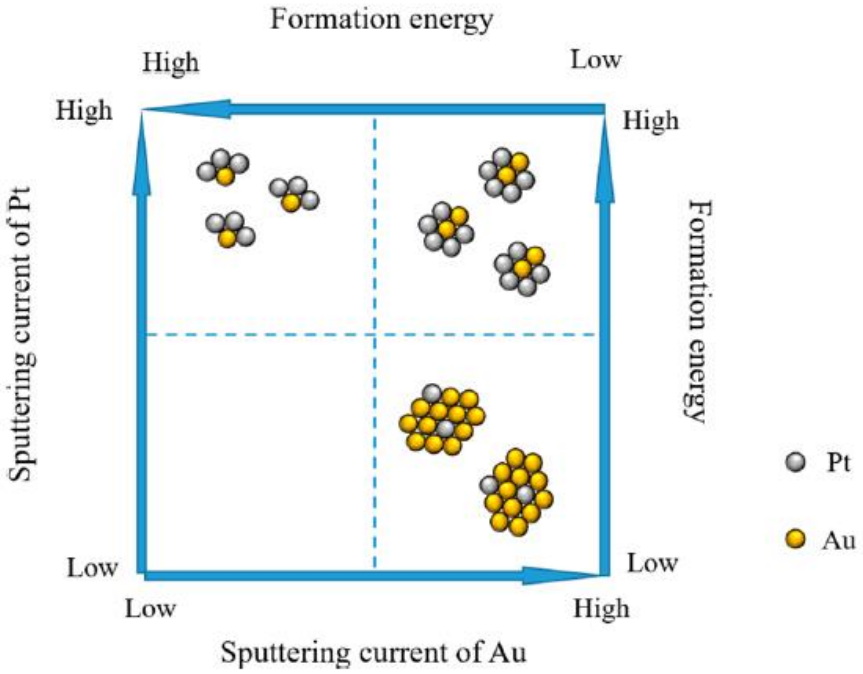

Figure 1.7. Schematic diagram illustrates the relation of sputtering current, formation energy, and particle size: when the Pt content is increased, the formation energy of the particles is increased, resulting in the formation of smaller particles. Reproduced from ref.34, copyright 2020 American Chemical Society.

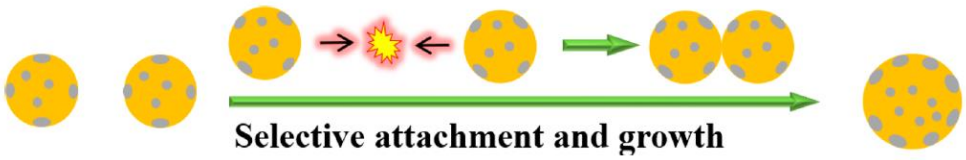

Figure 1.8. Schematic illustration for the formation of Pt/Au alloy NPs by the sputtering deposition of Pt and Au onto PEG via selective attachment and growth. The process can lead to surface-rich Pt and stop the growth of NPs. Reproduced from ref.34, copyright 2020 American Chemical Society.

1.5 Pt-based NPs

Because of the direct conversion of chemical energy contained in tiny organic molecules and hydrogen into electrical energy with great efficiency, fuel cells can be utilized as an environmentally friendly alternative to fossil fuels35. Among the various fuel cell types, the proton-exchange membrane fuel cell (PEMFC) is one of the most promising electrochemical energy conversion technologies. For diverse applications, PEMFC offers a wide operating power range of ~50 W to ~100 kW with high efficiency, low operating temperature and zero carbon emission3536. Several difficulties, however, such as the manufacture and scaling of catalysts and their supports, the durability and longevity of a fuel cell stack, and so on, are impeding the large-scale, long-term development of fuel cell technology3738. Fabricating a more active, long-lasting, and cost-effective cathode catalyst for the oxygen reduction process is one of the major challenges (ORR)3839. To save this problem, Pt is used for ORR in PEMFC because of the high catalytic activity3538.

One of the difficulties with Pt applications is the high cost, and low ORR kinetics of Pt catalysts also hinders the development of fuel cells. The sluggish kinetics of Pt for ORR cause high overpotential and require high loading of Pt35. Therefore, finding new catalytic materials with high electrocatalytic activity and stability is a top goal. Under this motive, Pt-based catalyst has attracted much attention since it can decrease the usage of Pt and shows high power density. For hydrogen fuel cell applications, Pt-based multi-structured nanocatalysts such as alloy, core-shell, and surface Pt-rich nanoparticles are widely explored35.

Traditionally, Pt NPs are loaded on some carbon supports with high surface area to reduce Pt usage as well as increasing electrochemically active surface area (ECSA). Nevertheless, this method still requires for large amount of Pt metal. Alloying Pt with other metals can reduce the use of Pt while enhancing catalytic activity.

Y. Lin et al. reported a rapid, controllable synthesis of three-dimensional PtCuCoNi quaternary alloys with low Pt-group metal by reducing metal precursors in aqueous solution40, as shown in Figure 1.9. The obtained Pt-based alloys excellent oxygen reduction and methanol oxidation reaction activities in acid solution. They proposed that the 3D PtCuCoNi quaternary alloys possess high porosity and large surface-to-volume ratio compared to the isolated Pt NPs, improving the mass transport and gas diffusion and thus leading to higher catalytic activity. Moreover, the quaternary alloys'

3D architecture and unsupported characteristic make them less susceptible to carbon corrosion-induced dissolution, aggregation, and falling off of Pt, which might reduce ECSA loss and increase catalytic stability. Another reason for the improvement of catalytic performance is alloying Pt with other metals resulted in a d-band shift of Pt-based alloys, this d-band shift can enhance the adsorption of reactants, intermediates, and products, hence improving the catalytic activity. Similarly, the modification of surface electronic structure through alloying can also enhance catalytic performance by the same mechanism40.

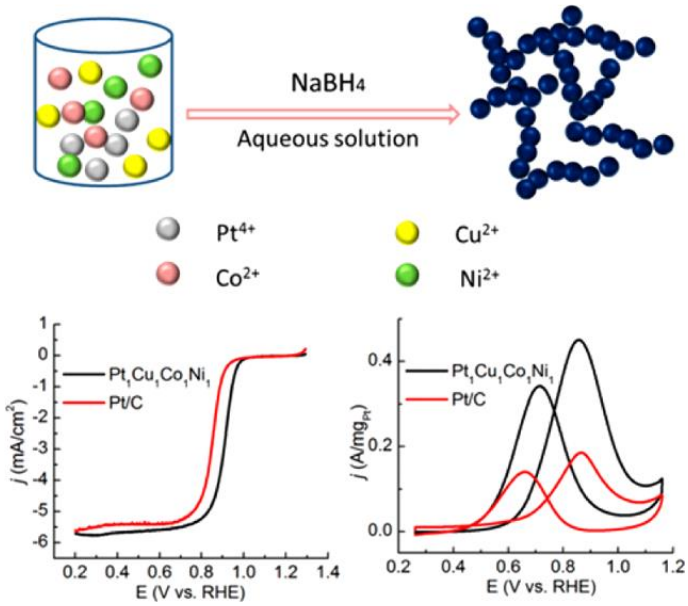

Figure 1.9. Illustration of the synthesis of PtCuCoNi quaternary alloys with three-dimensional structure and the results of electrochemical characterization. Reproduced from ref.40, copyright 2016 American Chemical Society.

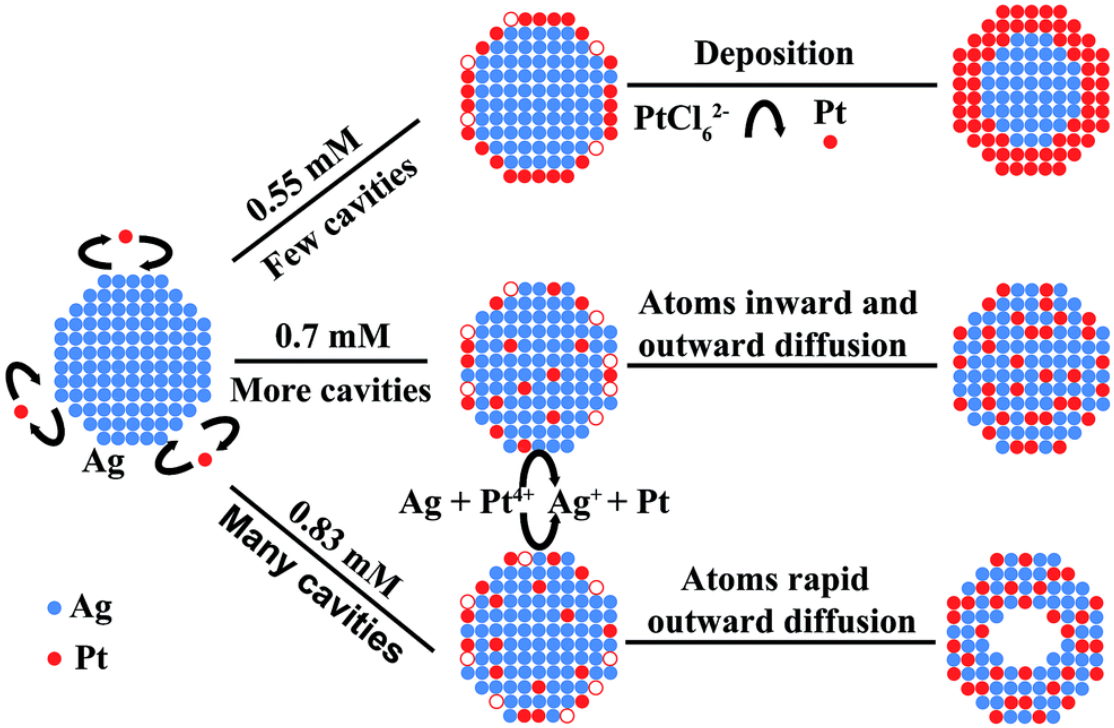

Figure 1.10. Schematic diagram of the formation of three Pt–Ag bimetallic nanoparticles with different nanostructures including $Ag_{core}@Pt_{shell}$ nanoparticles, solid and hollow Pt–Ag alloyed nanoparticles. Reproduced from ref.41, copyright 2016 The Royal Society of Chemistry.

M. Liu et al. synthesized Pt-Ag bimetallic alloy NPs by using a galvanic replacement reaction method. Three alloy nanostructures, Ag@Pt core-shell, highly alloyed solid, and hollow nanostructures were prepared by this method and the carbon supported alloy NPs were compared electrochemical performance41. Controlling nanophase structures for Pt-Ag bimetallic particles is as simple as adjusting H_2PtCl_6 concentrations in an aqueous solution (Figure 1.10). They found that the core-shell and hollow alloy NPs showed better mass and specific activities toward the ORR, which originated from the synergistic effect and/or intra-atomic electronic re-distribution between Pt and Ag

components in their bimetallic systems. On the one hand, the electron transfer from Pt to Ag can downshift the d-band center of Pt atoms, making the chemical adsorption of oxygenate intermediates weaker, facilitating O_2 adsorption on Pt surface. On the other hand, the electron transfer from Pt to Ag increased the unpaired electrons of Ag, which enhanced the O_2 adsorption and thus leading to higher catalytic activity.

1.6 Summary and perspective

Sputtering, as a physical synthesis method, can be used to directly synthesize metal NPs. As the development of sputtering technique, the sputtering substrates also developed from solid substrates to liquids, including silicon oil, ionic liquids (ILs), polymer liquids and so on. Furthermore, sputtering can also meet the requirements for synthesizing alloy NPs by using double-target systems. Normally speaking, the alloy NPs prepared by chemical methods are limited from the miscibility gaps in the bulk phase diagram. However, the enhanced metal diffusion and mixing and higher thermodynamic stability in the NPs can break this limitation and make the formation of alloy become more feasible. As a result, bimetallic even trimetallic alloy NPs can be synthesized by co-sputtering using double-target system, exempted from the inconvenience of target settings in single-target system (successive sputtering). Moreover, the sizes, compositions, and the structures of the alloy NPs can be controlled by adjusting the sputtering parameters (sputtering times, sputtering currents and so on). Thus the properties of the sputtered NPs are tunable, and the NPs can be pre-designed

for applications.

Pt NPs are potential catalysts for fuel cells because of their excellent catalytic activity especially in ORR. In recent years, many studies concentrate on lowering the Pt loading of the catalyst due to the high cost of Pt. Therefore, Pt-based alloy NPs attract much attention because of better catalytic performance and lower cost. Using sputtering technique to synthesize Pt-based alloy NPs is a novel and feasible approach, because this method is environmentally friendly, free of toxic reductant (compared with traditional chemical methods), and produce no by-products. The compositions and sizes of the resulted alloy NPs can be controlled during sputtering, so that better catalytic performance can be expected and achieved.

In conclusion, synthesizing alloy NPs via sputtering is a promising method due to its controllability and stability, and this method gives the obtained NPs wide possibilities of application. The NPs can not only be applied to the catalysts, but also some other fields, such as fluorescent NPs. No matter what the NPs are prepared for, sputtering can be a competitive approach and serves a wide variety of possible application directions.

1.7 References

1. P. J. Kelly, R. D. Arnell. Magnetron sputtering: a review of recent developments and applications. *Vacuum* **2000**, *56*, 159-172.
2. H. Wender, P. Migowski, A. F. Feil, S. R. Teixeira, J. Dupont. Sputtering deposition of nanoparticles onto liquid substrates: Recent advances and future trends. *Coordination Chemistry Reviews* **2013**, *257*, 2468–2483.
3. O. K. Alexeeva, V. N. Fateev. Application of the magnetron sputtering for nanostructured electrocatalysts synthesis. *International Journal of Hydrogen Energy* **2016**, *41*, 3373-3386.
4. M. T. Nguyen, T. Yonezawa. Sputtering onto a liquid: interesting physical preparation method for multi-metallic nanoparticles. *Sci. Technol. Adv. Mater.* **2018**, *19*, 883-898.
5. R. M. S. Martins. In-situ X-Ray diffraction studies during growth of Ni-Ti shape Memory Alloy films and their complementary ex-situ characterization. *PhD thesis*, Universidade Nova de Lisboa, **2008**.
6. F. Sanchette, A. Billard. Main features of magnetron sputtered aluminium–transition metal alloy coatings. *Surface and Coatings Technology* **2001**, *142-144*, 218-224.
7. X. W. Zhou, H. N. G. Wadley, R. A. Johnson, D. J. Larson, N. Tabat, A. Cerezo, A. K. Petford-Long, G. D. W. Smith, P. H. Clifton, R. L. Martens, T. F. Kelly. Atomic scale structure of sputtered metal multilayers. *Acta Materialia* **2001**, *49*, 4005-4015.
8. C. Imawan, H. Steffes, F. Solzbacher, E. Obermeier. A new preparation method for

sputtered MoO_3 multilayers for the application in gas sensors. *Sensors and Actuators B* **2001**, *78*, 119-125.

9. B. Song, Y. Hua, C. Zhou, Y. Li, L. Yang, Z. Song. Fabrication and anticorrosion behavior of a bi-phase TaNbHfZr/CoCrNi multilayer coating through magnetron sputtering. *Corrosion Science* **2022**, *196*, 110020.
10. J. Musil, J. Vlček. Magnetron sputtering of alloy and alloy-based films. *Thin Solid Films* **1999**, *343-344*, 47-50.
11. E. L. Miller, D. Paluselli, B. Marsen, R. E. Rocheleau. Development of reactively sputtered metal oxide films for hydrogen-producing hybrid multijunction photoelectrodes. *Solar Energy Materials & Solar Cells* **2005**, *88*, 131-144.
12. Y. Liu, A. Ishihara, S. Mitsushima, N. Kamiya, K. Ota. Transition Metal Oxides as DMFC Cathodes Without Platinum. *Journal of The Electrochemical Society* **2007**, *154 (7)*, B664-B669.
13. C. Hsu, T. Cheng, W. Huang, J. Wu, C. Cheng, K. Cheng, S. Huang. Relation between the plasma characteristics and physical properties of functional zinc oxide thin film prepared by radio frequency magnetron sputtering process. *Thin Solid Films* **2010**, *518*, 1953-1957.
14. G. Ye, Q. Zhang, C. Feng, H. Ge, Z. Jiao. Structural and electrical properties of a metallic rough-thin-film system deposited on liquid substrates. *Phys. Rev. B* **1996**, *54*, 14754-14757.
15. C. Burda, X. Chen, R. Narayanan, M. A. El-Sayed. Chemistry and Properties of Nanocrystals of Different Shapes. *Chem. Rev.* **2005**, *105*, 1025-1102.

16. H. Wender, L. F. de Oliveira, P. Migowski, A. F. Feil, E. Lissner, M. H. G. Prechtl, S. R. Teixeira, J. Dupont. Ionic Liquid Surface Composition Controls the Size of Gold Nanoparticles Prepared by Sputtering Deposition. *J. Phys. Chem. C* **2010**, *114*, 11764-11768.
17. T. Torimoto, K. Okazaki, T. Kiyama, K. Hirahara, N. Tanaka, S. Kuwabata. Sputter deposition onto ionic liquids: Simple and clean synthesis of highly dispersed ultrafine metal nanoparticles. *Appl. Phys. Lett.* **2006**, *89*, 243117.
18. E. Vanecht, K. Binnemans, J. W. Seo, L. Stappers, J. Fransaer. Growth of sputter-deposited gold nanoparticles in ionic liquids. *Phys. Chem. Chem. Phys.* **2011**, *13*, 13565-13571.
19. H. Wender, L. F. de Oliveira, A. F. Feil, E. Lissner, P. Migowski, M. R. Meneghetti, S. R. Teixeira, J. Dupont. Synthesis of gold nanoparticles in a biocompatible fluid from sputtering deposition onto castor oil. *Chem. Commun.* **2010**, *46*, 7019-7021.
20. R. N. Chauhan, R. S. Anand, J. Kumar. Structural, electrical and optical properties of radio frequency sputtered indium tin oxide thin films modified by annealing in silicon oil and vacuum. *Thin Solid Films* **2014**, *556*, 253-359.
21. R. Brown, B. Lönn, R. Pfeiffer, H. Frederiksen, B. Wickman. Plasma-Induced Heating Effects on Platinum Nanoparticle Size During Sputter Deposition Synthesis in Polymer and Ionic Liquid Substrates. *Langmuir* **2021**, *37*, 8821-8828.
22. K. Okazaki, T. Kiyama, K. Hirahara, N. Tanaka, S. Kuwabata, T. Torimoto. Single-step synthesis of gold–silver alloy nanoparticles in ionic liquids by a sputter deposition technique. *Chem. Commun.* **2008**, 691-693.

23. S. Suzuki, T. Suzuki, Y. Tomita, M. Hirano, K. Okazaki, S. Kuwabata, T. Torimoto. Compositional control of AuPt nanoparticles synthesized in ionic liquids by the sputter deposition technique. *CrystEngComm* **2012**, *14*, 4922-4926.

24. M. Hirano, K. Enokida, K. Okazaki, S. Kuwabata, H. Yoshida, T. Torimoto. Composition-dependent electrocatalytic activity of AuPd alloy nanoparticles prepared via simultaneous sputter deposition into an ionic liquid. *Phys. Chem. Chem. Phys.* **2013**, *15*, 7286-7294.

25. S. Suzuki, Y. Tomita, S. Kuwabata, T. Torimoto. Synthesis of alloy AuCu nanoparticles with the L10 structure in an ionic liquid using sputter deposition. *Dalton Trans.* **2015**, *44*, 4186-4194.

26. C. Liu, X. Chen, Y. Hu, T. Sham, Q. Sun, J. Chang, X. Gao, X. Sun, S. Wang. One-Pot Environmentally Friendly Approach toward Highly Catalytically Active Bimetal-Nanoparticle-Graphene Hybrids. *ACS Appl. Mater. Interfaces* **2013**, *5*, 5072-5079.

27. C. Liu, R. Liu, Q. Sun, J. Chang, X. Gao, Y. Liu, S. Lee, Z. Kang, S. Wang. Controlled synthesis and synergistic effect of graphene-supported PdAu bimetallic nanoparticles with tunable catalytic properties. *Nanoscale* **2015**, *7*, 6356-6362.

28. X. Cai, C. Liu, J. Liu, Y. Lu, Y. Zhong, K. Nie, J. Xu, X. Gao, X. Sun, S. Wang. Synergistic Effects in CNTs-PdAu/Pt Trimetallic Nanoparticles with High Electrocatalytic Activity and Stability. *Nano-Micro Lett.* **2017**, *9*, 48.

29. M. Hirano, K. Enokida, K. Okazaki, S. Kuwabata, H. Yoshida, T. Torimoto. Composition-dependent electrocatalytic activity of AuPd alloy nanoparticles

prepared via simultaneous sputter deposition into an ionic liquid. *Phys. Chem. Chem. Phys.* **2013**,*15*, 7286-7294.

30. D. König, K. Richter, A. Siegel, A. Mudring, A. Ludwig. High-Throughput Fabrication of Au–Cu Nanoparticle Libraries by Combinatorial Sputtering in Ionic Liquids. *Adv. Funct. Mater.* **2014**, *24*, 2049−2056.
31. M. T. Nguyena, T. Yonezawa, Y. Wang, T. Tokunaga. Double target sputtering into liquid: A new approach for preparation of Ag-Au alloy nanoparticles. *Mater. Lett.* **2016**, *171*, 75-78.
32. M. T. Nguyen, H. Zhang, L. Deng, T. Tokunaga, T. Yonezawa. Au/Cu Bimetallic Nanoparticles via Double-Target Sputtering onto a Liquid Polymer. *Langmuir* **2017**, *33*, 12389-12397.
33. A. Chauvin, A. Sergievskaya, A. E. Mel, A. Fucikova, C. A. Corrêa, J. Vesely, E. Duverger-Nédellec, D. Cornil, J. Cornil, P. Tessier, M. Dopita, S. Konstantinidis. Co-sputtering of gold and copper onto liquids: a route towards the production of porous gold nanoparticles. *Nanotechnology* **2020**, *31*, 455303.
34. L. Deng, M. T. Nguyen, J. Shi, Y. R. Chau, T. Tokunaga, M. Kudo, S. Matsumura, N. Hashimoto, T. Yonezawa. Highly Correlated Size and Composition of Pt/Au Alloy Nanoparticles via Magnetron Sputtering onto Liquid. *Langmuir* **2020**, *36*, 3004-3015.
35. M. Sharma, N. Jung, S. J. Yoo. Towards high-performance Pt-based nanocatalysts for oxygen reduction reaction through organic-inorganic hybrid concepts. *Chem. Mater.* **2018**, *30*, 2-24.

36. T. Zhang, P. Wang, H. Chen, P. Pei. A review of automotive proton exchange membrane fuel cell degradation under start-stop operating condition. Applied Energy 2018, 223, 249-262.

37. J. Wang. Barriers of scaling-up fuel cells: Cost, durability and reliability. *Energy* **2015**, *80*, 509-521.

38. S. Hussain, H. Erikson, N. Kongi, A. Sarapuu, J. Solla-Gullón, G. Maia, A. M. Kannan, N. Alonso-Vante, K. Tammeveski. Oxygen reduction reaction on nanostructured Pt-based electrocatalysts: A review. *International Journal of Hydrogen Energy* **2020**, *45*, 31775-31797.

39. K. Singh, E. B. Tetteh, H. Lee, T. Kang, J. Yu. Tailor-Made Pt Catalysts with Improved Oxygen Reduction Reaction Stability/Durability. *ACS Catal.* **2019**, *9*, 8622-8645.

40. S. Fu, C. Zhu, D. Du, Y. Lin. Enhanced Electrocatalytic Activities of PtCuCoNi Three-Dimensional Nanoporous Quaternary Alloys for Oxygen Reduction and Methanol Oxidation Reactions. ACS Appl. *Mater. Interfaces* **2016**, *8*, 6110-6116.

41. M. Liu, F. Chi, J. Liu, Y. Song, F. Wang. A novel strategy to synthesize bimetallic Pt–Ag particles with tunable nanostructures and their superior electro-catalytic activities toward oxygen reduction reaction. *RSC Adv.* **2016**, *6*, 62327-62335.

2 Pt/Ag alloy NPs prepared by co-sputtering

2.1 Introduction

Pt nanoparticles (NPs) have been used as active catalysts for various reactions.[1–5] However, the high cost of scarce Pt metal impedes their practical applications.[6–11] To solve this problem, Pt alloys have been made with cheaper metals, which can allow for attaining active catalysts at a lower cost.[6,12] For example, Pt/Ag alloy NPs show a better catalytic activity and catalyst durability compared with pure Pt NPs.[13–15] This is because the alloying could modify the electronic structure of Pt and generate lattice distortion for improving the electrocatalytic performances.[13–15] Pt and Ag form some intermetallic compounds, and there are big miscibility gaps in the bulk phase diagram.[16] The formation of alloy becomes more feasible in small NPs wherein the enhanced metal diffusion and mixing and higher thermodynamic stability can be achieved.[17,18] Pt/Ag alloy NPs with various sizes and compositions have been reported by a reduction at elevated temperature or electrochemical reduction.[6,12,19–22] For example, P. Song et al. synthesized Pt/Ag alloy NPs of about 54 at % Pt with variable sizes from 7.5 to 15 nm for catalytic electrooxidation of liquid fuels. They demonstrated the best electrocatalytic activities for Pt/Ag NPs of the smallest size.[6] Li et al. prepared Pt/Ag alloy NPs with 50 and 66 at % of Pt and an average size of ~2.5 nm supported by graphene conductive networks for advanced oxygen reduction reaction electrocatalysts.[12] However, at a lower content of Pt, they obtained segregated Ag and Pt/Ag alloys.[12] Therefore, synthesis of alloy Pt/Ag NPs of controlled size and

composition is demanded.

Sputtering is a conventional physical technique for the fabrication of thin films or creation of NPs directly on solid substrates from the bulk target in a vacuum and dry conditions.[23,24] Nonvolatile or low volatile liquids as the substrates,[25–35] e.g., silicone oils,[25] ionic liquids,[26,27,30,31] and liquid polymers,[28,32–35] have been used for obtaining NPs dispersed in liquids for a long time continuous sputtering. Compared with the traditional chemical reduction method, co-sputtering can simultaneously produce metal atoms and clusters of two or more metals for making alloy NPs at room temperature regardless of the difference in redox potentials of metals and without using toxic reductants.[30–35] Moreover, it is capable of varying the properties of NPs by varying the size, composition, composition distribution, and structures of NPs via adjusting the sputtering parameters such as the currents applied to the metal targets.[30–35] Co-sputtering onto liquid allows obtention of solid solution alloys of metal pairs that have miscibility gaps and/or form intermetallic compounds in the phase diagram such as Au/Pd, Pt/Au, Au/Cu, and Cu/Pd.[30–35] However, so far, there has been no report on co-sputtering onto liquid at room temperature of Pt/Ag NPs below 3 nm, their fine structure, and whether solid solution alloys can be attained, especially for the composition in the miscibility gap. Furthermore, the correlation of particle size and composition varied with the metal pairs; that is, the size−composition relation is not obvious in co-sputtered Au/Cu and Cu/Pd whereas highly correlated in Pt/Au NPs.[33–35] This relation has not been addressed for cosputtered Pt/Ag NPs. Therefore, we chose to synthesize Pt/Ag

alloy NPs at room temperature by cosputtering onto liquid polyethylene glycol (PEG), a biocompatible and cheap liquid, and investigate the fine structure and composition of the resulting NPs in the present study. The obtained Pt/Ag NPs were analyzed by ultraviolet−visible spectroscopy (UV−vis), transmission electron microscopy (TEM), high-resolution TEM (HR-TEM), scanning TEM (STEM), energy-dispersive X-ray spectroscopy (EDX), and X-ray diffraction (XRD). The results proved that Pt/Ag NPs have a solid solution structure. We found that the sputtering currents applied to the targets had little effect on the average sizes, but they could vary the particle compositions and had impacts on the composition distributions of the samples. Comparing the compositions and particle sizes of the NPs sputtered onto PEG and on TEM grids, we address the impact of the substrate in the formation and growth of particles. We found that in the presence of PEG, the composition could be determined by the random combination of metal atoms/clusters in the sputtering chamber with less change after the growth of NPs in PEG.

2.2 Experimental section

2.2.1 Materials

PEG (MW = 600, Junsei, Japan), the Pt target (99.99% in purity, 50 mm in diameter, Tanaka Precious Metals, Japan), the Ag target (99.99% in purity, 50 mm in diameter, Tanaka), and TEM grids (Nisshin EM, Japan) were used.

2.2.2 Synthesis of Pt-Ag Alloy NPs

The co-sputtering method has been reported elsewhere.[32–35] In the present study, PEG was stirred (650 rpm) under vacuum in a flask in an oil bath at 90 °C for at least 2 h to remove water and gases. Then, 10 mL of PEG was added into a Petri dish with a diameter of 60 mm, which was located horizontally in the center of a magnetron sputtering vacuum chamber, and a stirrer was put under the PEG surface. PEG was under stirring at 80 rpm during sputtering. Pt and Ag targets were used in this co-sputtering technique, and elemental ratios of the formed Pt/Ag NPs were controlled by adjusting the sputtering current applied to each sputtering target (10−50 mA). PEG, carbon-coated Cu TEM grids, and glass slides were used as the substrate for sputtering experiments. When a TEM grid was used as the substrate, it was placed at the center of the Petri dish. The center of the surface of PEG and TEM grids was located at a distance of 110 mm from the two metal targets. Similarly, glass slides were located at the center position of the Petri dish. After several times of vacuum and gas exchanging with inert Ar to remove O_2, the pressure of the vacuum chamber was kept constant at 2 Pa. Cooling ethanol of 0 °C was used for cooling the metal targets during sputtering. In all the sputtering experiments, before collecting NPs, Pt and Ag targets were sputtered for 10 min to clean the target surface. During this period, removable shutters located in front of metal targets and on top of the liquid polymer were used to prevent the contamination from falling onto the liquid. Sputtering onto PEG was conducted for 30 min, whereas sputtering onto the TEM grids was conducted for 1 s to 2 min with the TEM grids. The applied sputtering current was varied from 10 to 50 mA for two metal

targets, and the total mass of Pt/Ag in PEG was 0.85-2.24 mg (Table 1). The sputtering system was equipped with a thermocouple and a temperature-controlled system to keep the substrate temperature at 30 °C.

Table 2.1 Pt at % in Pt/Ag by Mass Measurement, EDX, and XPS Analysis

Sample	Nominal Pt (at. %) by mass measurement[a]	Pt (at. %) by STEM-EDS[b]	Pt (at %) by XPS[c]	Mass of NPs (mg)[a,d]
Pt50Ag10	90.9	85.1 ± 14.0	87.9	1.65
Pt50Ag50	55.9	60.2 ± 16.2	44.4	2.24
Pt10Ag50	11.9	19.8 ± 12.2	8.4	0.85

[a]sputtered onto Al foil. [b]NPs sputtered onto PEG (30 min). [c]NPs sputtered on Si (10 s). [d]estimated for 30 min sputtering.

2.2.3 Characterization

UV−vis spectra were collected immediately after sputtering deposition with a JASCO V-630 spectrophotometer using a quartz cuvette with an optical path of 1 mm. All spectra were baseline corrected using an empty quartz cuvette. The size and shape of the NPs were obtained from TEM (JEOL JEM-2000FX, 200 kV). HR-TEM and STEM images were obtained using a JEOL JEM-ARM200F operating at 200 kV and a FEI Titan cube operating at 300 kV. Samples for TEM, HR-TEM, and STEM analysis were prepared by dipping a grid into PEG dispersion for about 10 s, then immediately dipping into ethanol for at least 20 min to remove the excess amount of PEG, and finally drying

in the air at room temperature for a few minutes. Size and size distributions were collected from TEM, HR-TEM, and STEM images by measuring approximately 150 particles in at least three different regions of the grid using ImageJ software. The structure of NPs was evaluated using high-angle annular dark-field (HAADF)-STEM and XRD (Rigaku Mini Flex II, Cu Kα radiation, λ = 1.5418 Å, scanning speed of 0.5°/ min). XRD samples were prepared by addition of excess acetone into PEG-NP dispersion and then centrifuged multiple times at 10000 rpm for 10 min each time for isolating Pt/Ag NPs from PEG. The purified Pt/Ag sample precipitate in acetone after a day. The X-ray intensities for all samples were plotted as a function of 2 theta and were normalized. Elemental mapping using energy-dispersive X-ray spectroscopy (EDX) coupled with STEM (JEOL JEM-ARM200F) was carried out to verify the existence of Pt/Ag alloy NPs and their composition. An X-ray photoelectron spectroscope (XPS, JEOL, JPS-9200, Al Kα source) was used to collect XPS spectra of NPs sputtered onto PEG for 30 min and on Si wafer for 10 s. Graphite was added to PEG dispersion to collect NPs; then, the dispersion was centrifuged and washed with acetone several times to separate and purify the Pt/Ag NPs from PEG. The C 1s of graphite at 284.2 eV was used for charge correction. For samples sputtered on Si wafer, Si 2p at 99.2 eV was used for charge correction. Energy pass values of 20 and 10 eV were used for collecting XPS spectra of samples in PEG and on Si wafer. A higher energy pass was used for the sample sputtered onto PEG because at low energy pass, the intensity is insufficient to be distinguished from the background.

2.3 Results and Discussion

To distinguish the samples synthesized with different currents applied to the Pt and Ag targets, the samples are labeled with the metals and corresponding applied sputtering currents. For example, the sample Pt50Ag50 represented a sample synthesized by co-sputtering with the currents of 50 mA for Pt and Ag targets.

2.3.1 TEM Images and UV−vis Spectra of Pt/Ag NPs.

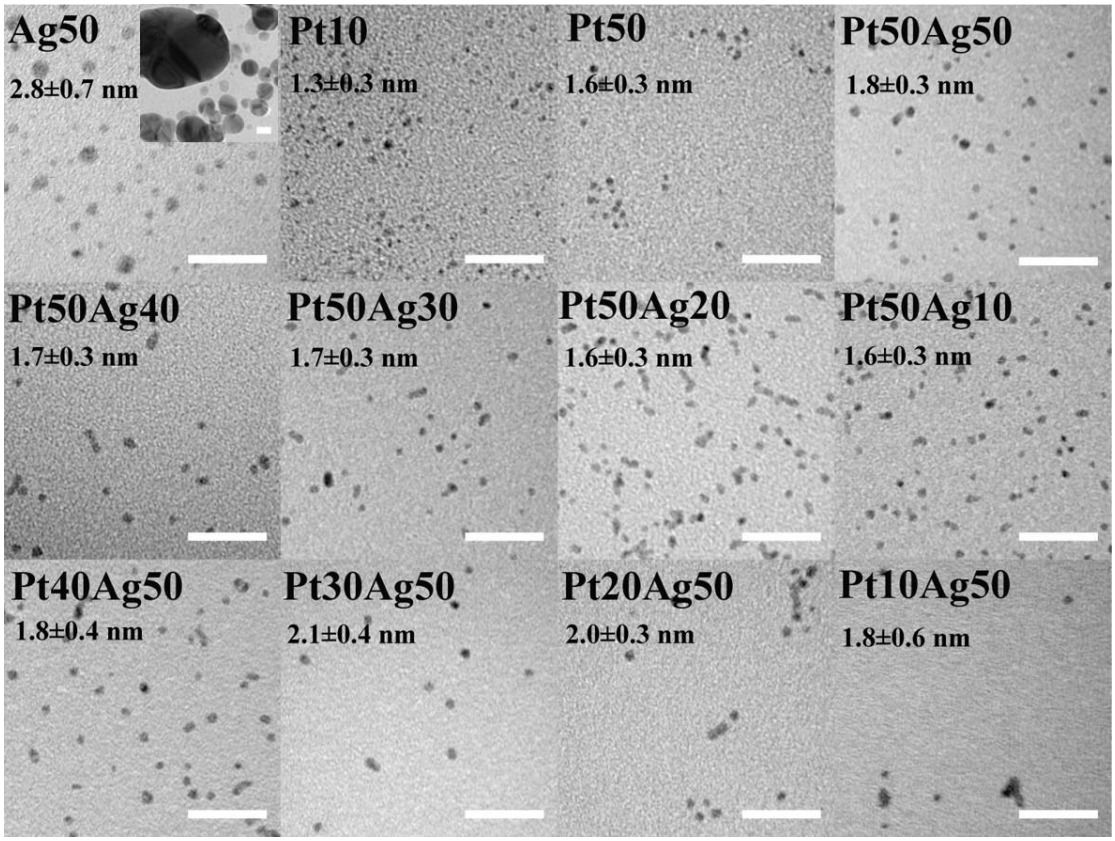

Figure 2.1 TEM images of Ag, Pt, and co-sputtered Pt/Ag samples. The scale bar in white is 20 nm. The average particle sizes are shown in the images.

Figure 1 shows the bright-field TEM images of Pt NPs, Ag NPs, and the co-sputtered Pt/Ag alloy NPs. The size distributions of samples Pt50Ag(10 ~ 50) and Pt(10 ~ 50)Ag50 are shown in Figures 2.2 and 2.3, respectively. The results were obtained by

measuring the diameters of nearly spherical NPs. Ag50 contained big Ag NPs (inset of Figure 1) and small Ag NPs of 2.8 ± 0.7 nm. Pt10 and Pt50 had average particle diameters of 1.3 ± 0.3 and 1.6 ± 0.3 nm, respectively. The average sizes of Pt50Ag(10 ~ 50) samples increased from 1.6 ± 0.3 to 1.8 ± 0.3 nm as the sputtering current of Ag increased from 10 to 50 mA and that of Pt constant at 50 mA. The Pt(10 ~ 50)Ag50 samples with average sizes of 1.8 ± 0.3, 1.8 ± 0.4, and 1.8 ± 0.6 nm were obtained when the sputtering current for Pt is 10, 40, and 50 mA, respectively. The broader size distribution was observed when using a low sputtering current for Pt, i.e., 10 mA (Figure 2.3), and some big particles were observed in the sample. The mean size of Ag/Pt NPs slightly increased to 2.0 ± 0.3 and 2.1 ± 0.4 nm for Pt20Ag50 and Pt30Ag50 samples, respectively. This result indicated that the currents applied to the metal targets in the range of 10−50 mA did not have a significant impact on the particle sizes of the samples and a sample of a higher content of Ag generally has a slightly bigger particle size. Overall, the particle sizes of Pt/Ag alloy NPs are smaller than those of pure Ag NPs. This is similar to the results observed in co-sputtered Pt/Au and Au/Cu NPs into PEG in which the alloy NPs have a size in between that of the monometallic NPs.[33,34] However, different from Pt/Au alloy NPs with a strong correlation of size and composition (regulated by sputtering current),[34] such a correlation is not obvious in Pt/Ag NPs. This is similar to co-sputtered Au/Cu NPs in PEG.[33]

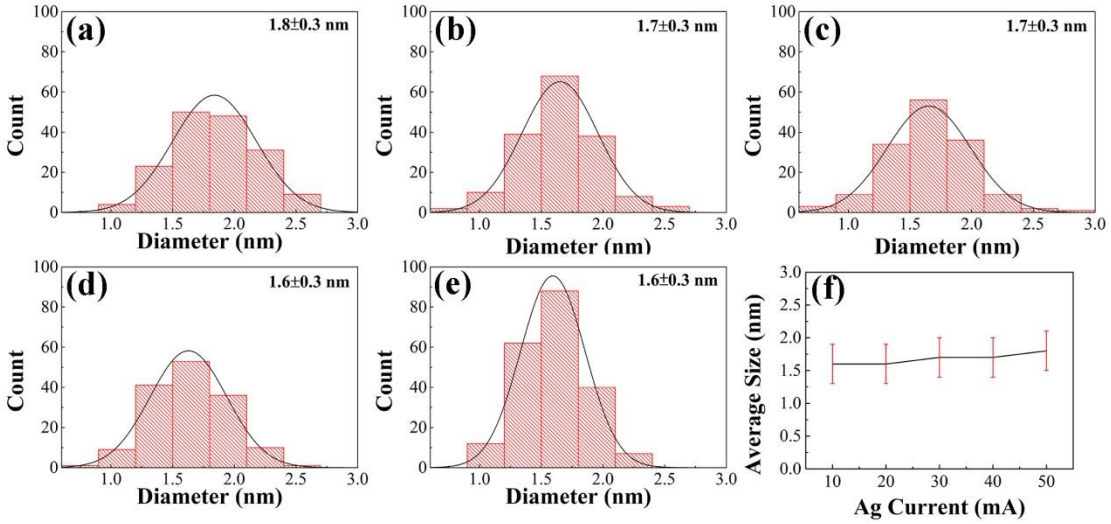

Figure 2.2 Size distributions of Pt/Ag samples shown in Figure 1: (a) Pt50Ag50, (b) Pt50Ag40, (c) Pt50Ag30, (d) Pt50Ag20, (e) Pt50Ag10. (f) Summary of the particle sizes shown in a-e with the error bar showing the standard deviation of particle sizes.

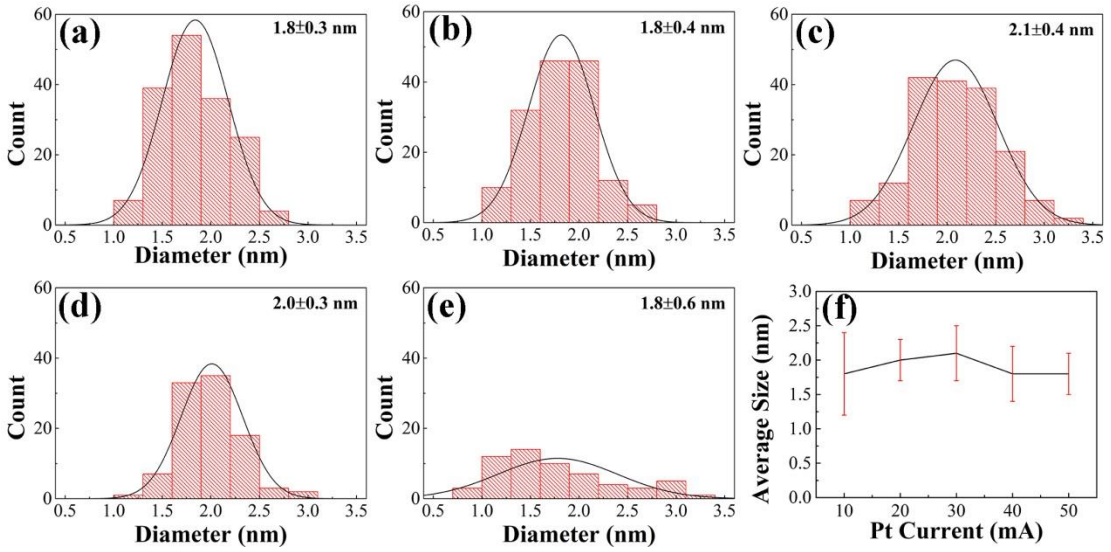

Figure 2.3 Size distributions of Pt/Ag samples shown in Figure 1: (a) Pt50Ag50, (b) Pt40Ag50, (c) Pt30Ag50, (d) Pt20Ag50, (e) Pt10Ag50. (f) Summary of the particle sizes shown in a-e with the error bar showing the standard deviation of particle sizes.

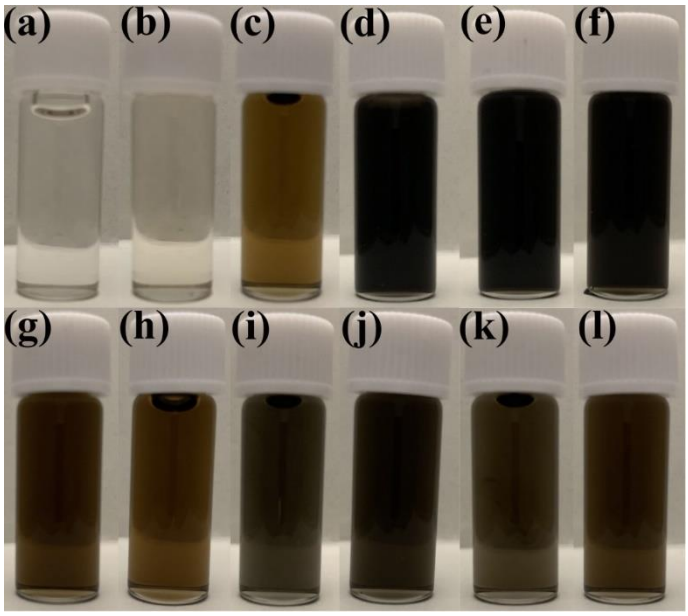

Figure 2.4 The photographs of samples (a) Ag50, (b) Pt10, (c) Pt50, (d) Pt50Ag50, (e) Pt50Ag40, (f) Pt50Ag30, (g) Pt50Ag20, (h) Pt50Ag10, (i) Pt40Ag50, (j) Pt30Ag50, (k) Pt20Ag50 and (l) Pt10Ag50.

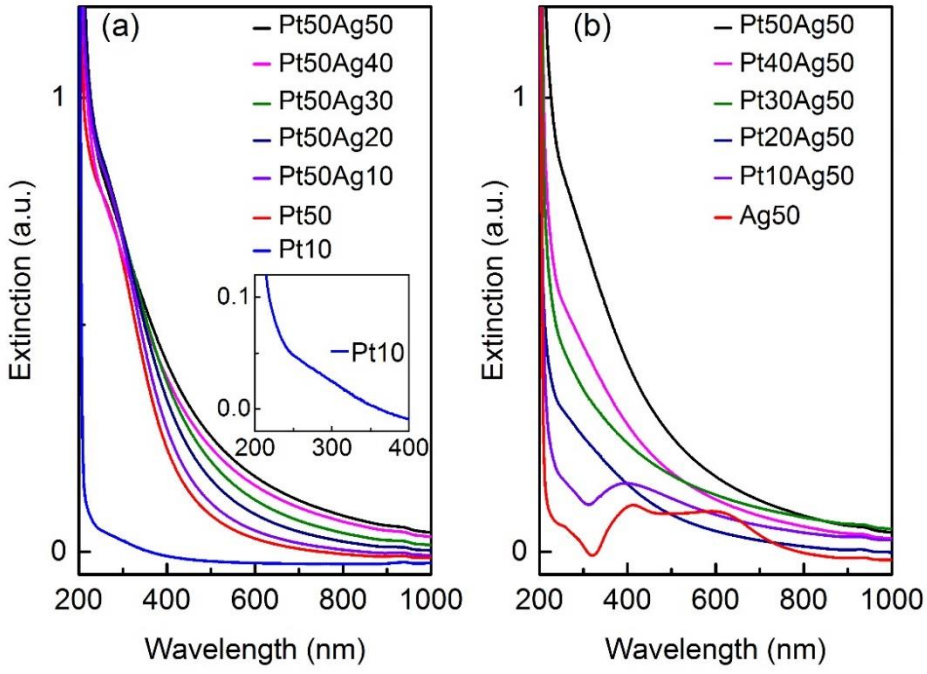

Figure 2.5 UV-Vis spectra of the Pt/Ag alloy NPs synthesized under different sputtering

currents: (a) 50 mA for Pt and 0~50 mA for Ag target; (b) 0~50 mA for Pt and 50 mA for Ag target. UV-Vis spectrum of Pt NPs sputtered at 10 mA is shown in Figure 2.5a and its inset shows the magnified spectrum with the horizontal axis from 200 to 400 nm.

After sputtering, the samples (Figure 2.5) were collected and analyzed with UV-Vis. Figure 2.5a shows the UV-Vis spectra of the samples Pt50Ag50, Pt50Ag40, Pt50Ag30, Pt50Ag20, Pt50Ag10, and Pt50. There was an absorption shoulder at around 280 nm in these samples, which indicated the presence of Pt in the PEG dispersion. The intensity of this shoulder for Pt/Ag samples sputtered using the applied current to Pt target of 50 mA and Pt50 sample did not vary significantly because it was related to the concentration of Pt. It could be seen that sample Pt10 (inset of Figure 2.5a) had a similar absorption shoulder with lower intensity compared with sample Pt50. This is because the lower sputtering current for Pt target produced the more dilute Pt/PEG dispersion. There was no localized surface plasmon resonance (LSPR) of pure Ag NPs in all of these co-sputtering samples Pt50Ag(10~50). Further, the absorption intensity above 350 nm of these samples increased with the increase of the applied current for Ag thereby increase of Ag content in the Pt/Ag NPs. These results indicated a possible alloy formation between Pt and Ag.

For the samples Pt(0~50)Ag50, the UV-Vis spectra (Figure 2.5b) also showed the broad absorption shoulder around 280 nm associated with the presence of Pt in the samples.

Overall in low wavelength region (below 400 nm) the absorption intensity increased as the applied current of Pt increased. This demonstrated the correlation between the concentration of Pt and the intensity of the absorption shoulder at 280 nm. Further, the spectra of Ag50 and Pt10Ag50 showed an LSPR peak at around 400 nm, which is the typical characteristic of Ag NPs. And there is also an absorption peak at around 600 nm in the spectrum of Ag50 owing to the existence of some aggregation and/or agglomeration in the sample. This result is consistent with TEM results and suggests that PEG stabilizes Pt better than Ag and Ag-rich Pt/Ag NPs. This absorbance decreased with increasing the applied currents to Pt from 0 to 20 mA, indicating that alloying Pt and Ag suppressed the formation of pure Ag NPs and the agglomeration. Further increasing the sputtering currents applied to Pt from 20 to 50 mA, the absorption peak at 400 nm belongs to pure Ag NPs disappeared. Thus, the UV-Vis results obtained by varying the sputtering currents of Ag and Pt suggested the formation of Pt/Ag alloys in the co-sputtered samples. To confirm the formation of solid solution alloy in Pt/Ag NPs, we further analyzed the structure and composition of samples with XRD, HAADF images, STEM-EDX mappings, and XPS.

2.3.2 Crystal structures of Pt/Ag NPs

To analyze the structure of the co-sputtered Pt/Ag alloy NPs, the NPs synthesized by double head sputtering onto PEG were separated from PEG and their XRD patterns were collected. The XRD results are shown in Figure 2.6a. The diffraction peaks of samples Pt50Ag50 and Pt10Ag50 were located between the peaks of Pt and Ag

reference. The (111) peak position of Pt50Ag50 (2θ = 39.4°) was closer to that of reference Pt (2θ = 39.8°) and farther to that of reference Ag (2θ = 38.1°) when compared to that of Pt10Ag50 (2θ = 38.1°). This indicated sample Pt50Ag50 had a higher composition of Pt compared with the sample Pt10Ag50. Further, the (111) peak of Pt50Ag50 was symmetric whereas that of Pt10Ag50 was somehow as-symmetric with more broadening to the right. This indicates that in the sample Pt10Ag50, Pt/Ag grains with the sharp feature may contain slightly more Ag compared to the sample with smaller grain sizes, which we will confirm later with STEM-EDS mapping (Figure 2.7). The average grain size estimated from line broadening of (111) XRD peak using Scherrer equation resulted in a size of 4 and 15 nm for Pt50Ag50 and Pt50Ag10 NPs, respectively. The large grain size found in Pt50Ag10 is understandable as larger crystals even in a smaller population can contribute more significant signals compared with the small ones. We observed that Pt10Ag50 and Pt50Ag50 NPs could be separated from PEG by centrifugation. However, this method was not sufficient to obtain the precipitate of Pt50Ag10 NPs. This is consistent with the TEM results that this sample had the smallest size (1.6 ± 0.3 nm) among all co-sputtered Pt/Ag samples (Figure 2.1). Besides, Pt50Ag10 sample with the highest content of Pt in Pt/Ag alloy NPs and small sizes can be stable enough in PEG, which was similar to our previous observation for sputtered Pt and Pt-rich Pt/Au NPs.[34] In an attempt to collect the Pt50Ag10 NPs, we added some fume SiO_2 into the PEG dispersion containing Pt50Ag10 NPs first to adsorb Pt/Ag NPs before using the centrifugation to separate NPs/SiO_2 from PEG. Unfortunately, there was no peak detectable in Pt50Ag10. Judging from the results, we

think that the amount of Pt50Ag10 NPs separated from PEG was too small and/or their crystallinity was not good.

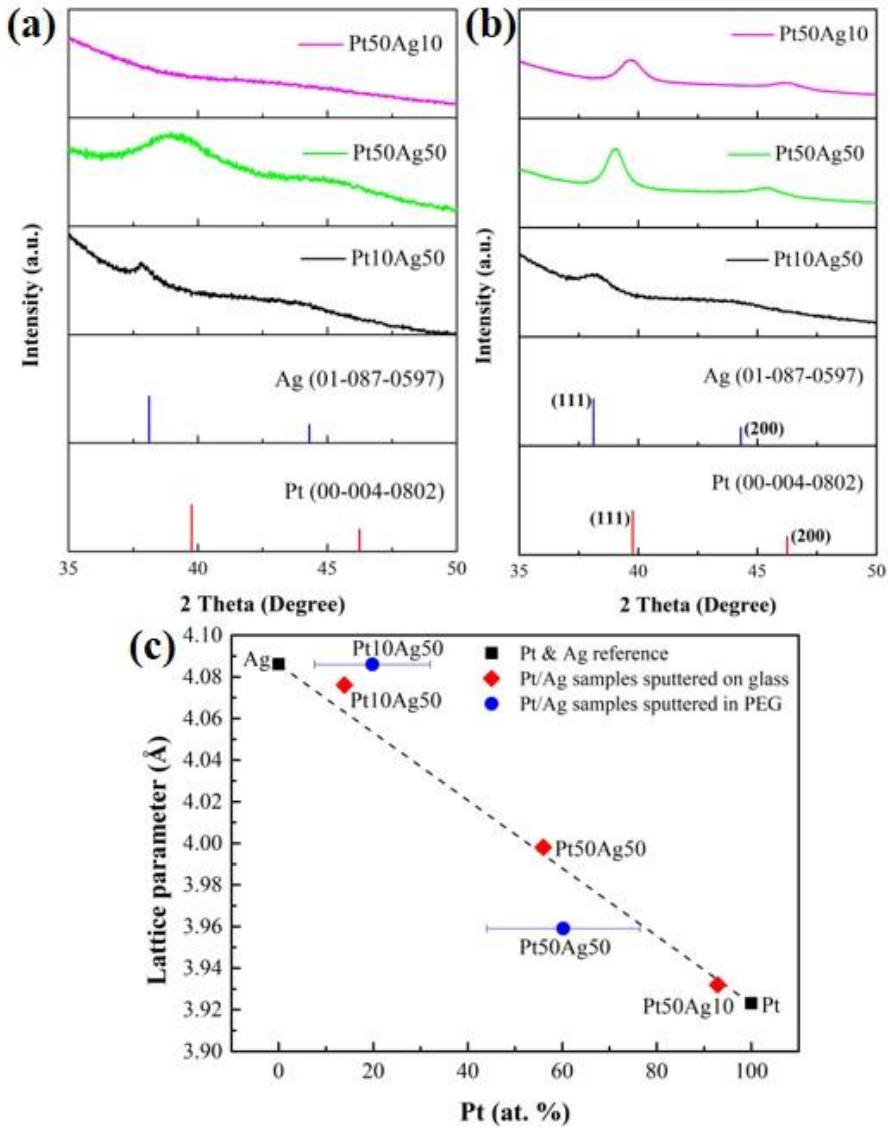

Figure 2.6 (a) XRD patterns of Pt50Ag10, Pt50Ag50, and Pt10Ag50 deposited in PEG. (b) XRD patterns of Pt50Ag10, Pt50Ag50, and Pt10Ag50 sputtered on glass for 2-5 min. Stick patterns are characteristic diffraction peaks from (111) and (200) planes of reference Pt (JCPDS No. 00-004-0802) and Ag (JCPDS No. 01-087-0597). (c) Relation between lattice parameter estimated from XRD peak positions of (111) planes and atomic compositions of Pt in Pt/Ag. The compositions of Pt/Ag in PEG and on glass

were measured with STEM-EDS and mass measurement (Table 2.1), respectively. Error bars are standard deviations of the compositions measured by STEM-EDS for Pt/Ag obtained in PEG. The lattice parameters of Ag and Pt from the above XRD reference in Figures 2.6a and b were used. The black, dashed line connecting Ag and Pt shows the ideal relation for Pt/Ag alloys which follows Vegard's law[36].

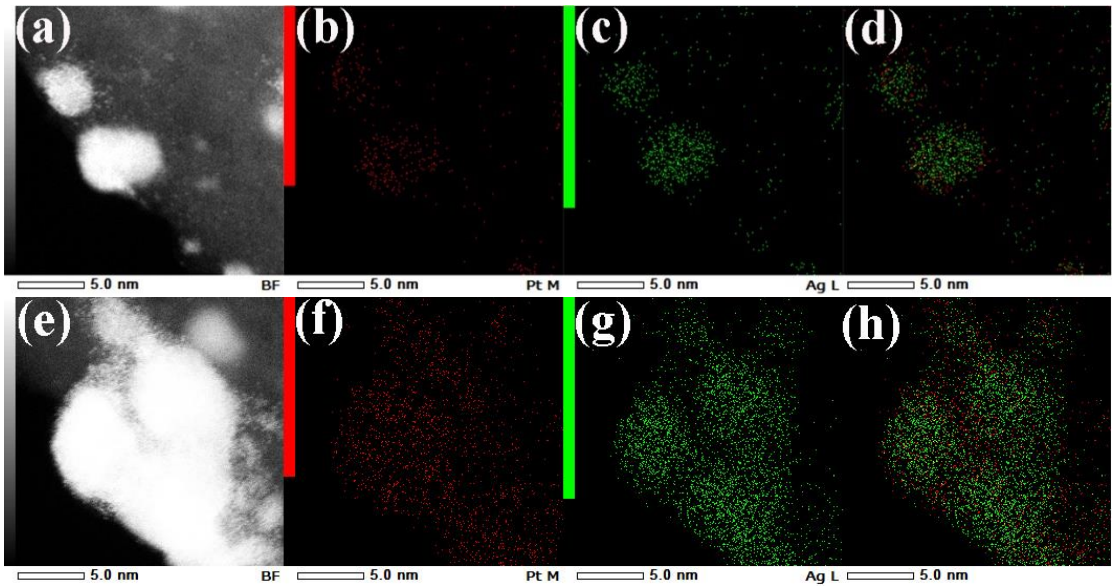

Figure 2.7 (a, e) HAADF and (b-d, f-h) STEM-EDX mapping images of Pt10Ag50 sample with (b, f) Pt M, (c, g) Ag L, and (d, h) overlapping image of Pt and Ag. The average Pt atomic composition measured from STEM-EDX is 19.8 ± 12.2 at %. Figures (e-h) show an agglomeration of big and small Pt10Ag50 NPs in PEG where the big particle contain more Ag.

Consequently, the experiments of co-sputtering of Pt and Ag directly on glass slides for different sputtering currents and times were carried out to get more insight (Figures 2.6b and 2.8). Figure 2.6b shows that the (111) peak positions of Pt10Ag50, Pt50Ag50,

and Pt50Ag10 samples that sputtered on glass slides for 5 min were 38.21, 39.01, and 39.67°, respectively. The peaks were between (111) peaks of the reference Ag and Pt. Further, there was a clear trend in the peak positions among 3 samples, that is the (111) peak shifts in the direction from Ag towards Pt with increasing Pt content by varying the sputtering currents applied to Pt and Ag targets. The lattice parameters obtained from the (111) XRD peak positions of the samples sputtered on glass showed a linear relationship with the sample composition (Figure 2.6c). This followed Vegard's law[36] and indicated the formation of solid solution alloys of Pt/Ag on glass. The results for Pt/Ag NPs sputtered onto PEG show certain deviations from the ideal relation. This indicated that (i) some sputtered NPs with different compositions may remain in PEG and not able to be separated for XRD analysis, (ii) formation of the crystal structure is incomplete, and/or (iii) the measured composition distributed in a large range.

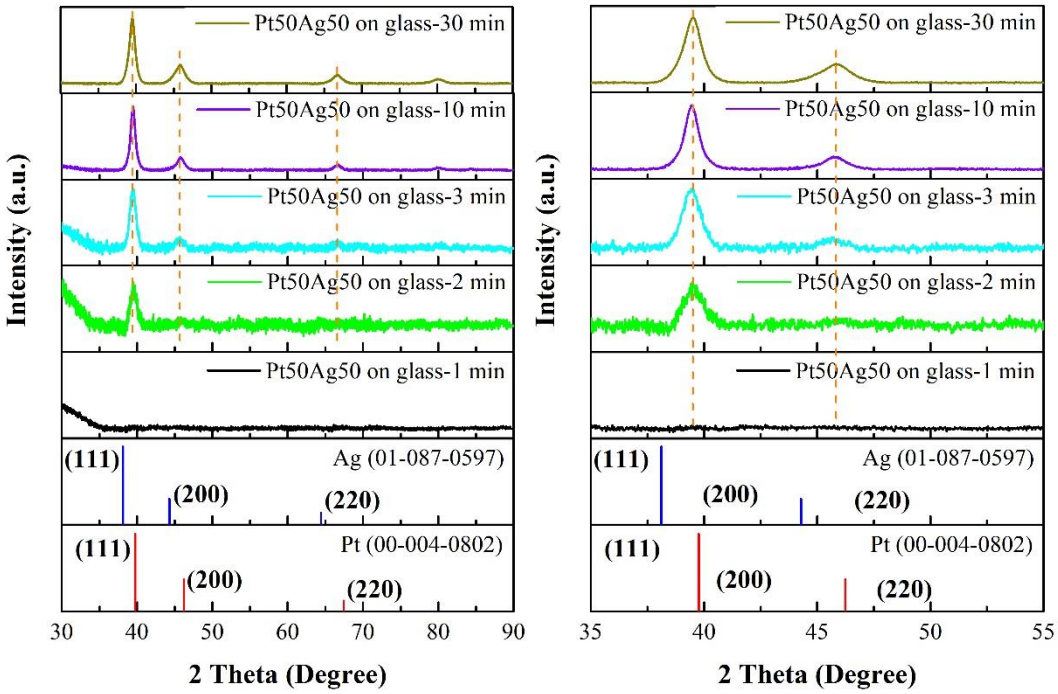

Figure 2.8 (left) XRD results of Pt50Ag50 samples that sputtered on glass slides with

a sputtering time of 1, 2, 3, 10, and 30 min. (right) Enlarged XRD patterns of samples shown on the left.

We also observed that varying the sputtering times onto glass substrate from 2 min to 30 min did not change the peak position for sample Ag50Pt50 (Figure 2.8). However, the smallest time of sputtering for the Bragg diffraction peaks appearing in the XRD pattern was different depending on the samples. For example, when the sputtering time on glass was 2 min, fairly weak (111) diffraction peak of Pt50Ag10 (Figure 2.9) and clear (111) peak of Pt50Ag50 sample (Figure 2.6b) were detected whereas no peak was observed for Pt10Ag50 (Figure 2.9). It required 5 min sputtering to observe weak signals of typical diffraction peak in the sample Pt10Ag50 (Figure 2.6b). The possible reason could relate to the amount and crystallinity of Pt/Ag NPs. Higher sputtering currents and time resulted in more metal atoms in the sputtering chamber, thus leading to a higher amount of NPs and possibly the formation of larger grain size, for which the XRD signals of Pt/Ag crystals were more significant. On this basis, for the same sputtering time, Pt50Ag50 had the largest amounts of atoms and thus, it had the most profound peaks among 3 samples. The sputtering rate of Pt is slightly higher than that of Ag (Table 2.2) and it took a shorter time of sputtering for Pt50Ag10 compared with Pt10Ag50 for the clear appearance of XRD peaks.

Table 2.2 Amount of sputtered Pt and Ag for 1 h sputtering* on Al foil

Sample	Sputtering current (mA)		Amount of Pt	Amount of Ag
	Pt target	Ag target		
Pt50	50	0	3.12 mg	

			(16.0 µmol)	
Pt10	10	0	0.34 mg	
			(1.7 µmol)	
Ag50	0	50		1.36 mg
				(12.6 µmol)
Ag10	0	10		0.17 mg
				(1.6 µmol)

*The sputtering was conducted using only one head of the double head target

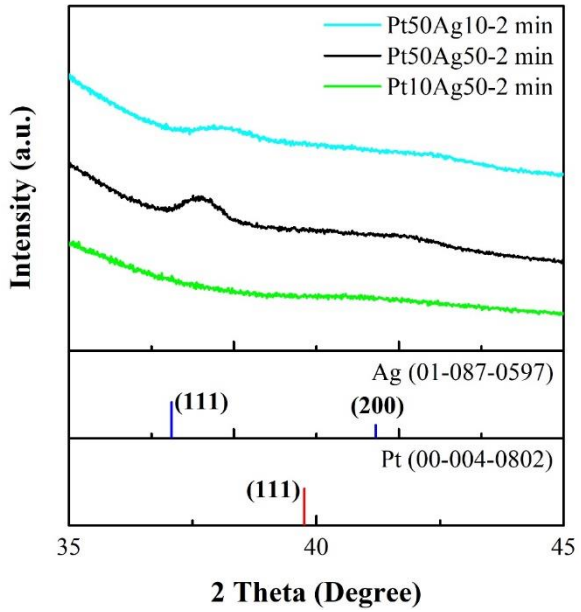

Figure 2.9 XRD patterns of Pt50Ag50, Pt50Ag10, and Pt10Ag50 samples prepared by co-sputtering on the glass slides for 2 min.

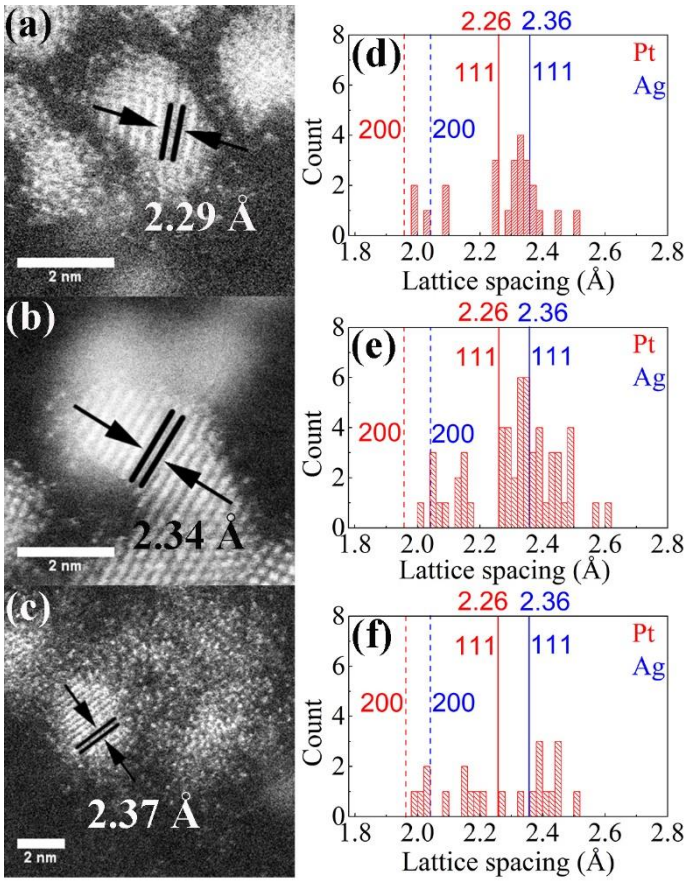

Figure 2.10 HAADF images of (a) Pt50Ag10, (b) Pt50Ag50 and (c) Pt10Ag50 samples obtained in PEG. The lattice spacings are shown in the pictures. Lattice parameter distributions of (d) Pt50Ag10, (e) Pt50Ag50 and (f) Pt10Ag50. Solid and dashed lines represent the lattice parameters of (111) and (200) planes, respectively, of Pt (in red) and Ag (in blue). The numbers of the particles measured are 24, 55, and 23 for samples Pt50Ag10, Pt50Ag50, and Pt10Ag50, respectively.

Figures 2.10 a-c present the STEM-HAADF images of co-sputtered Pt/Ag alloy NPs with clear lattice fringes. The lattice spacings of samples Pt50Ag10 Pt50Ag50, and Pt10Ag50 were measured to be 2.29 Å, 2.34 Å, and 2.37 Å, respectively. The lattice spacing of (111) plane in reference Pt (JCPDS No. 00-004-0802) and Ag (JCPDS No.

01-087-0597) are 2.26 Å and 2.36 Å, respectively. The lattice spacing of Pt10Ag50 was slightly larger than that of Pt50Ag50 and Pt50Ag10, which was caused by a larger content of Ag in Pt10Ag50, and the lattice spacing of reference Ag is bigger than that of Pt. It was noticed that the lattice spacing of Pt10Ag50 (2.37 Å) was a little bit larger than that of reference Ag (2.36 Å), this could be caused by the small sizes and thus, swelling of the crystal structure. The statistical analysis of the lattice spacings using HAADF images (Figures 2.10 d-f) of three samples, Pt50Ag10, Pt50Ag50 and Pt10Ag50, consistently showed the lattice spacing distributions and the peaks of this distribution varied with the sample compositions wherein sample with more Pt had the peak of (111) lattice spacings closer to pure Pt. Further, the higher composition of Ag in Pt/Ag samples likely caused an increase in the fraction of NPs with larger lattice spacings compared with that of (111) plane in pure Ag as observed in HAADF images. The exact reason is not clear, but, this can associate with the expansion in crystal structures of Ag rich Pt/Ag NPs under STEM observation.

2.3.3 Discussion in solid solution and intermetallic compound structure of Pt/Ag NPs

Three intermetallic compounds[16] with Pt at. % of 45 ($Ag_{55}Pt_{45}$), 50 (AgPt), and 75 ($AgPt_3$) and only intermetallic compound[37] of $Ag_{15}Pt_{17}$ (53 at. % Pt) are shown in the phase diagram given by Karakaya et al[16] and Okamoto,[37] respectively. These intermetallic compounds are at 400 °C or more. Experimental data for the annealed samples at high temperature 750 °C for 80 days by Hart et al.[38] supports the existence

of the ordered $L1_1$ structure at about 50 at. % Pt. The calculated structures of bimetallic Pt-Ag (including un-stable phases) suggest AgPt trigonal, AgPt hexagonal, $AgPt_3$ cubic, Ag_3Pt cubic, and $AgPt_4$ trigonal structure.[39] Two un-stable phases (cubic $AgPt_3$ and Ag_3Pt) can decompose as: $AgPt_3 \leftrightarrow AgPt_4 + AgPt$ and $Ag_3Pt \leftrightarrow Ag + AgPt$.

Our XRD results indicate the co-sputtered Ag/Pt NPs have a cubic structure, thus, we exclude the existence of trigonal, hexagonal intermetallic compounds. $Pt_{50}Ag_{50}$ NPs have a composition of 60.2 ± 16.2 at % Pt (Table 2.1). The composition range locates in the miscibility gap in the above phase diagrams and possibly contains cubic $AgPt_3$ (75 at. % Pt) and $L1_1$ AgPt (50 at. % Pt) compounds. However, no obvious peak separation or as-symmetry in the XRD pattern of Ag50Pt50 (Figure 2.6), suggesting that the XRD peaks do not comprise two intermetallic compounds.

If $L1_1$ ordered AgPt NPs (50 at. % Pt) are the majority of Ag50Pt50 sample, 13 % of NPs can have the right orientation with the zone axis parallel to (111) plane to be observed with the ordered $L1_1$ structure (assuming the random orientation of NPs on the grid for STEM).[40] We analyzed the STEM-HAADF images of Pt50Ag50 NPs (>200 particles) with many NPs align in the zone axis along (111) planes. However, the arrangement of the ordered $L1_1$ structure with alternating dark and brighter contrast for Ag and Pt (111) was not found. The uniform and random contrast of the atom columns belong to (111) planes in NPs was observed (an example is shown in Figure 2.11). This indicates the disordered solid solution structure with mixed Pt and Ag in each atom

column of (111) planes.

Besides, annealing at high temperatures is often necessary to form the intermetallic compounds (ordered structures). Torimoto reported the conversion of the sputtered fcc-solid solution alloy AuCu NPs to the ordered $L1_0$ intermetallic compound by annealing (> 150 °C).[41] Peng et al. reported that chemically synthesized Pt/Ag NPs at 260 °C for 1 h are solid solution alloy for Pt of 20-80 at. %.[42] This suggests that 260 °C and 1 h reaction is insufficient to form the intermetallics. Under simultaneously atomic condensation of Ag and Pt sources in an ultra-high vacuum chamber, Pirat et al. observed fcc disordered Ag/Pt alloy NPs (50 at. % Pt).[40] After annealing at 400 °C, they observed the ordered $L1_1$ Ag/Pt intermetallic NPs.[40] However, no annealing was conducted for our samples and this fact must be taken into account when considering the crystal structure of Pt/Ag. Hence, based on the results of XRD, the relation of lattice-parameter and composition among samples of different Pt at %, d-spacings, and intensity profile we assign the obtained structure in our co-sputtered Ag/Pt NPs as solid solution alloy. Though we could not prove that there is completely no intermetallic compound, we are confident that the disordered solid solution alloy NPs are the majority under our synthesis conditions.

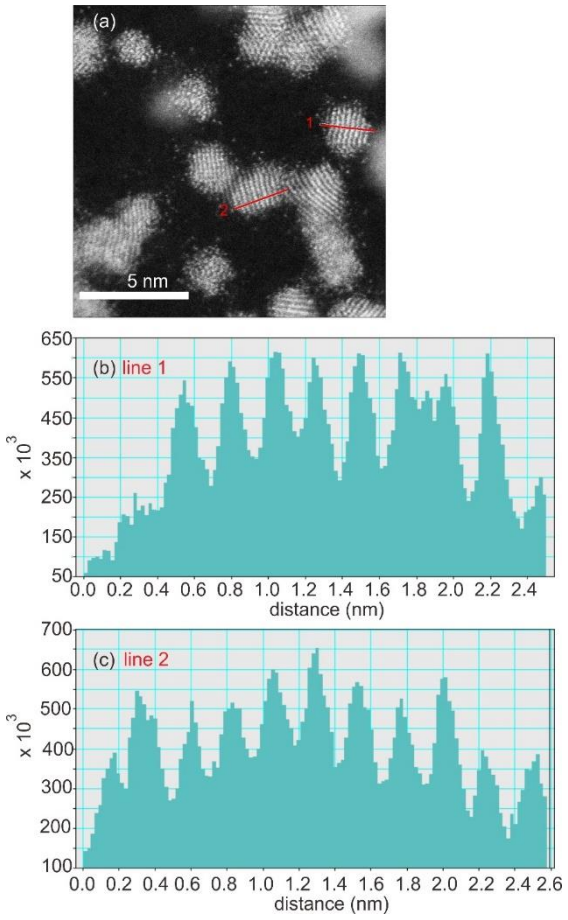

Figure 2.11 (a) HAADF image of Pt50Ag50 NPs sputtered onto PEG with particles showing (111) planes parallel to the zone axis. (b,c) Intensity profiles for atom columns of (111) planes in the red lines 1 and 2 in (a), respectively. (b) Uniform and (c) random intensity contrast show the mixed Pt and Ag in each atom column of the (111) planes.

2.3.4 XPS analysis of Pt/Ag NPs

Figure 2.12 shows XPS narrow scans of Pt 4f and Ag 3d of Pt50Pt50 sputtered onto PEG. Two components, namely, Pt-1 at 71.29 ($4f_{7/2}$), 74.59 eV ($4f_{5/2}$) and Pt-2 at 73.01 ($4f_{7/2}$) and 76.31 eV ($4f_{5/2}$) can be used to fit Pt 4f spectrum. The spin-orbit splitting of

both components (3.3 eV) is the same as the reference for Pt.[43] However, the binding energy of Pt 4f of Pt-1 is close to whereas that of Pt-2 is 2.2 eV larger than the reference value (70.9 eV for Pt $4f_{7/2}$).[43] Ag 3d spectrum can be deconvoluted using 4 components, that is, Ag-1 at 367.36 ($3df_{5/2}$) and 373.35 eV ($3df_{3/2}$), Ag-2 at 368.27 ($3df_{5/2}$) and 373.97 eV ($3df_{3/2}$), and 2 plasmon loss feature peak at 371.41 and 372.25 eV. The spin orbit-splitting of Ag-1 and Ag-2 component in Ag 3d spectrum is of 5.97 and 5.70 eV, respectively, which is lower than the reference value for Ag metal (6 eV).[43] The shoulder around 370 eV in Ag 3d is not completely fitted. Fitting Ag $3d_{5/2}$ and $3d_{3/2}$ with two curves still leaves a part of the shoulder unfitted and results in $3d_{5/2}$ and $3d_{3/2}$ with different FWHM (Figure 2.13). Possibly, a non-uniform charging effect occurred or a higher signal to noise ratio and higher intensity is required to distinguish the signal from noise. Ag-2 component has binding energy similar to metallic Ag whereas Ag-1 is closed to Ag oxide (note that binding energy of Ag^0 is higher than Ag oxide).[43] From the Ag 3d and Pt 4f narrow scans, the sample can contain Pt/Ag metal (Pt-1 and Ag-2) and partially oxidized Pt-Ag (Pt-2 and Ag-1). However, we cannot exclude the possibility of the size effect in the energy shift of Pt-2 and Ag-1.

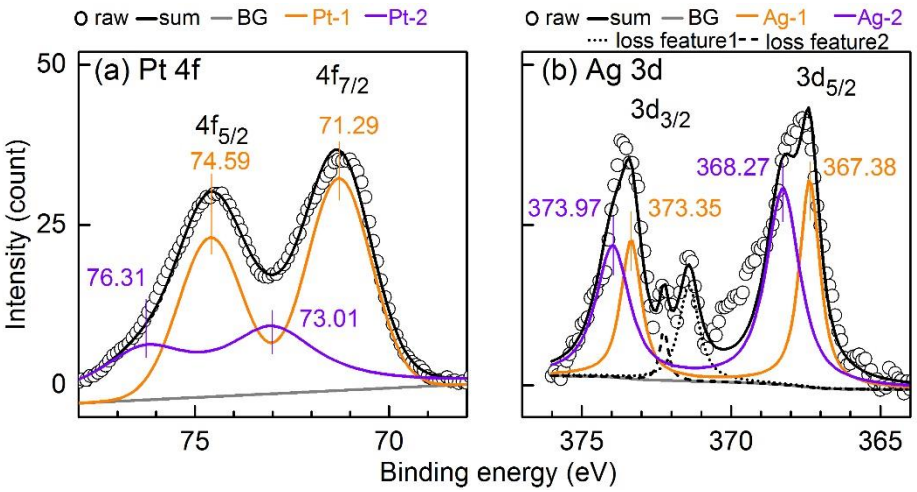

Figure 2.12 XPS spectra of Pt50Ag50 sputtered onto PEG for 30 min: (a) Pt 4f, (b) Ag 3d.

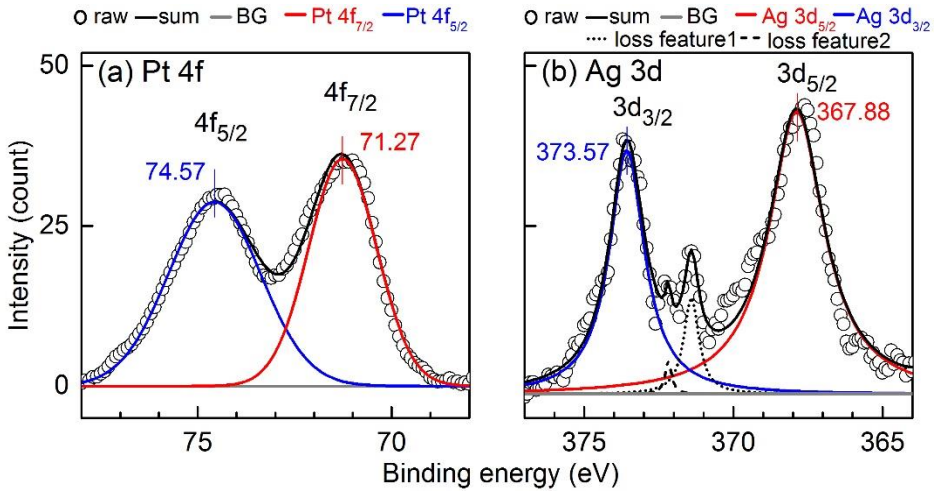

Figure 2.13 XPS narrow scan spectra of (a) Pt 4f and (b) Ag 3d regions of Pt50Ag50 NPs sputtered onto PEG. Single peak is used to fit each XPS spin-orbit component in the spectra. Larger full-width at half maximum (FWHM) of the high energy component is observed for Pt and reversed phenomenon is observed for Ag. The spectrum near 370 eV of Ag 3d could not be fit well with a single peak.

It is difficult to judge the alloying formation for NPs in PEG with confidence based on XPS. This is because the intensity is low (count < 50), high pass energy of 20 eV was required to increase the intensity (this lowers the spectrum resolution), the effect of Ar etching to remove PEG on the particle surface (e.g., oxidation), and possible interference of the non-uniform charging effect after Ar etching (Figures 2.12 and 2.13). Thus, we also collected XPS spectra for Pt/Ag, Pt, and Ag NPs sputtered on Si wafer for 10 s with high energy resolution (pass energy of 10 eV) and sufficient intensity (more than 40 times higher than the samples obtained in PEG) as shown in Figure 2.14.

10 s sputtering allows to obtain separated NPs with size between 1.6 ± 0.3 (5 s sputtering) and 2.6 ± 0.3 nm (20 s sputtering) (Figure 2.15). This size range covers the size of NPs obtained in PEG. The spin-orbit splitting of Pt 4f and Ag 3d are the same as the reference for Pt and Ag, respectively. The binding energies of Pt 4f and Ag 3d peaks are given in Table 2.3. Figure 2.16 shows that for an increase of Pt at. % in NPs, the binding energy shift of Pt $4f_{7/2}$ is more positive compared with the bulk reference Pt whereas the shift of Ag $4d_{5/2}$ is more negative compared with the bulk reference Ag (Ag is more oxidized). This can be caused by the dilution of Pt by alloying with Ag in small NPs and the charge transfer from Ag to Pt.[44,45] Both of the effects indicate the alloying between Ag and Pt. The composition estimated from XPS quantitative analysis is given in Table 2.1, which is close to the nominal composition by mass measurement.

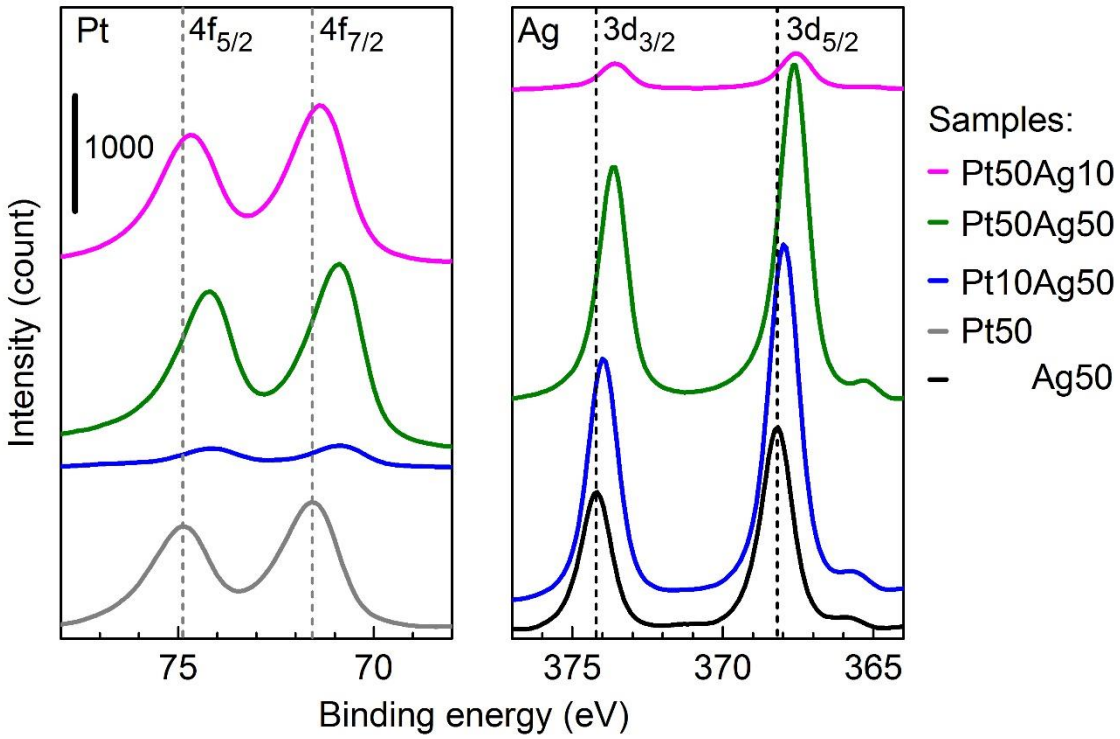

Figure 2.14 Narrow scan XPS spectra of Pt 4f and Ag 3d of the Pt50Ag10, Pt50Ag50, Pt10Ag50, Pt50, and Ag50 NPs sputtered on silicon wafers for 10 s. The dashed lines mark the peaks for the samples of Pt50 and Ag50 NPs.

Table 2.3 XPS peak position of Ag 3d and Pt 4f core levels of NPs sputtered on Si

Sample	Peak position (eV)			
	Pt $4f_{7/2}$	Pt 4f5/2	Ag $3d_{5/2}$	Ag $3d_{3/2}$
Pt50Ag10	71.4	74.7	367.6	373.6
Pt50Ag50	70.9	74.2	367.6	373.6
Pt10Ag50	70.9	74.2	368.0	374.0
Pt50	71.6	74.9	-	-
Ag50	-	-	368.2	374.2

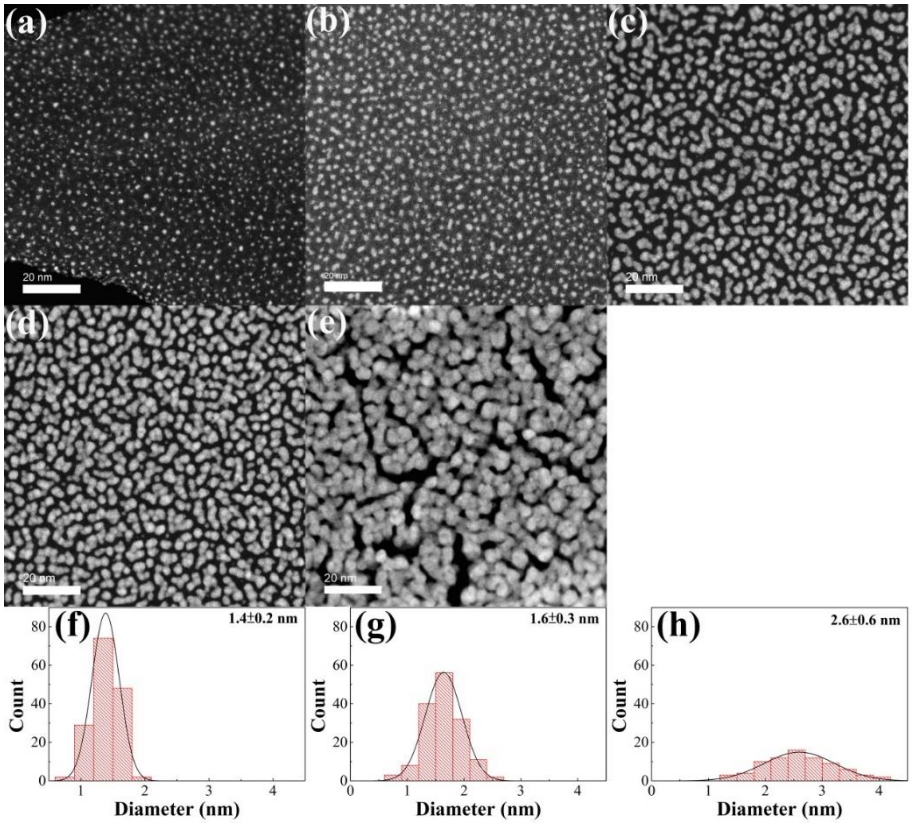

Figure 2.15 STEM-HAADF images of Pt50Ag50 sputtered on the TEM grids with a sputtering time of (a) 1 s, (b) 5 s, (c) 20 s and (d) 30 s, and (e) 2 min. The scale bar is 20 nm. The size distributions are given for NPs obtained by sputtering for (f) 1s, (g) 5 s, and (h) 20 s. The average sizes of the samples are 1.4, 1.6, and 2.6 nm, respectively.

Severe aggregation, necking, and growth to film like structure were observed for samples obtained after sputtering for 30 s and 2 min.

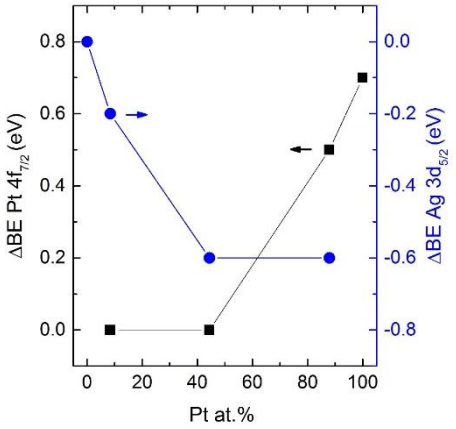

Figure 2.16 The correlation of the binding energy shift of Pt $4f_{7/2}$ and Ag $3d_{5/2}$ peaks and Pt atomic composition in Pt/Ag, Pt, and Ag NPs sputtered on Si for 10 s. The shift was obtained by subtracting the binding energy of Pt $4f_{7/2}$ and Ag $3d_{5/2}$ of NPs to the reference value of metallic Pt $4f_{7/2}$ (70.9 eV) and Ag $3d_{5/2}$ (368.2 eV), respectively. The composition was estimated using XPS analysis.

2.3.5 Composition Distribution of Pt/Ag NPs

To analyze the composition of the samples, the STEM-EDX mapping was carried out. Figure 2.17 is the STEM-EDX mapping images of the Pt50Ag50 obtained in PEG. The presence of Pt and Ag in the same position was observed for all single NPs in Figure 2.17, indicating the formation of Pt/Ag alloy NPs. The EDS spectrum for the map area of a single particle (Figure 2.18) shows the signal of Pt and Ag is low but distinguishable from the background. The elemental line profile of several single NPs (Figure 2.19) shows the Pt and Ag at the same regions. However, the count number in the line profile is also low, which can be insufficient to assess the elemental ratio for some positions in

the particle with high confidence. This is because the NPs are small and they moved or were damaged so we could not have a long time scan to increase the count numbers. The STEM-EDX mapping images of Pt50Ag10 and Pt10Ag50 are shown in Figures 2.20 and 2.7, respectively. Aside from Pt/Ag alloy, pure Pt NPs and some pure Ag NPs were observed in Pt50Ag10 and Pt10Ag50 samples, respectively.

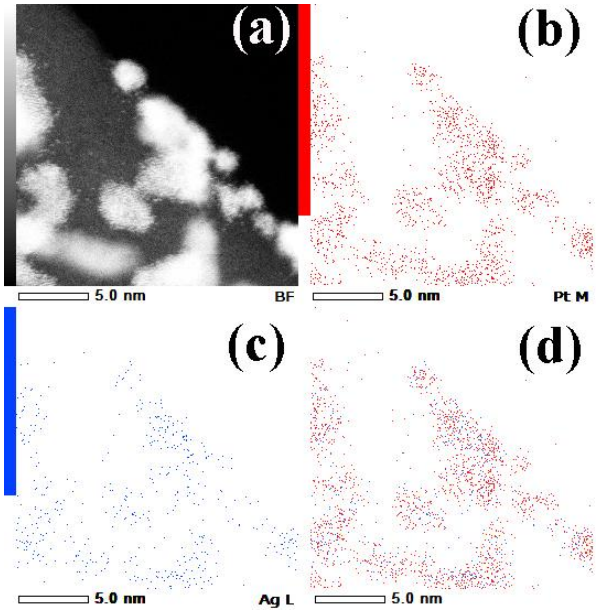

Figure 2.17 (a) HAADF image and (b-d) STEM-EDS mapping images of Pt50Ag50 NPs: (b) Pt M, (c) Ag L, and (d) overlapping image of Pt and Ag.

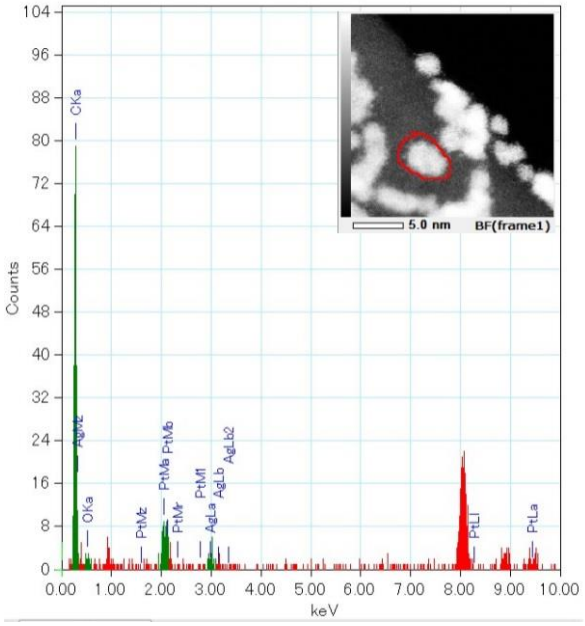

Figure 2.18 EDS spectra for single particle (in red circle in the STEM-HAADF image) shown in STEM-EDS mapping for Pt50Ag50 in PEG in Figure 9. The signals of Pt Mα and Ag Lα are distinguished from the background.

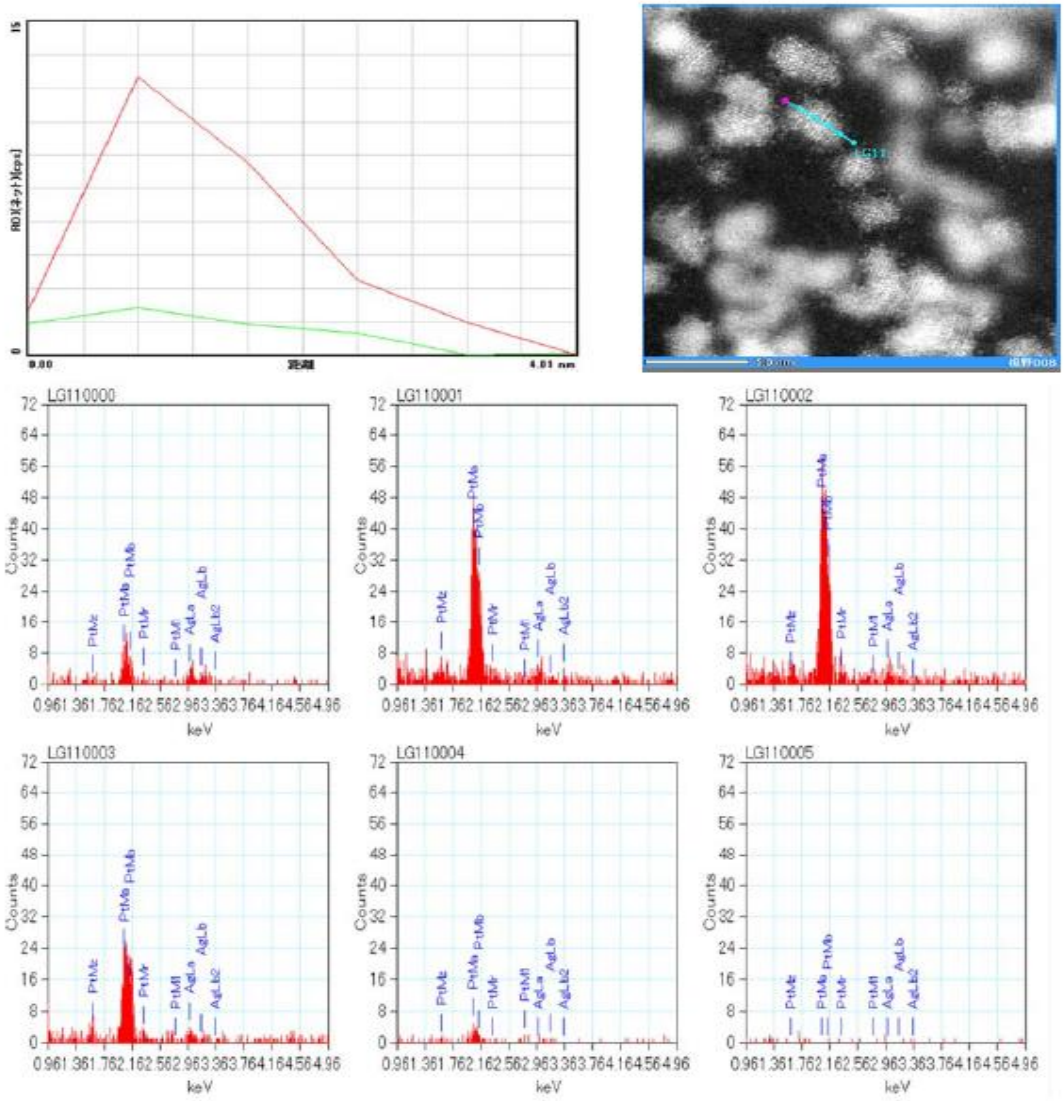

Figure 2.19 (top-left) STEM-EDS line profile for Pt Mα (red) and Ag Lα (green) of a Pt50Ag50 NP sputtered onto PEG along the green line in the HAADF image (top-right). (bottom) EDS spectra collected at the points shown in the line in HAADF image for taking the line profile.

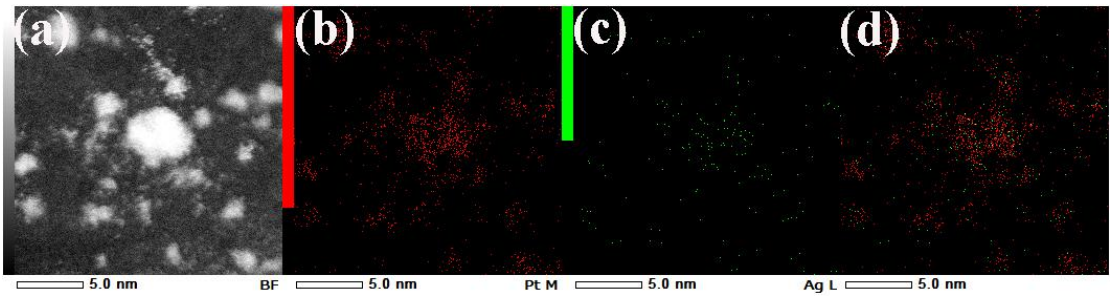

Figure 2.20 (a) HAADF and (b-d) mapping images of Pt50Ag10 sample with (b) Pt M, (c) Ag L, and (d) overlapping image of Pt and Ag. The average Pt atomic composition of this sample measured from STEM-EDX results is 90.5 at %.

Based on EDS mapping results, the composition distributions in Pt/Ag NPs for 3 samples sputtered onto PEG and on TEM grids are plotted in Figure 2.21 wherein the horizontal axis is the atomic composition of Pt over the total amount of Pt and Ag and the vertical axis shows the population of the composition detected in the samples.

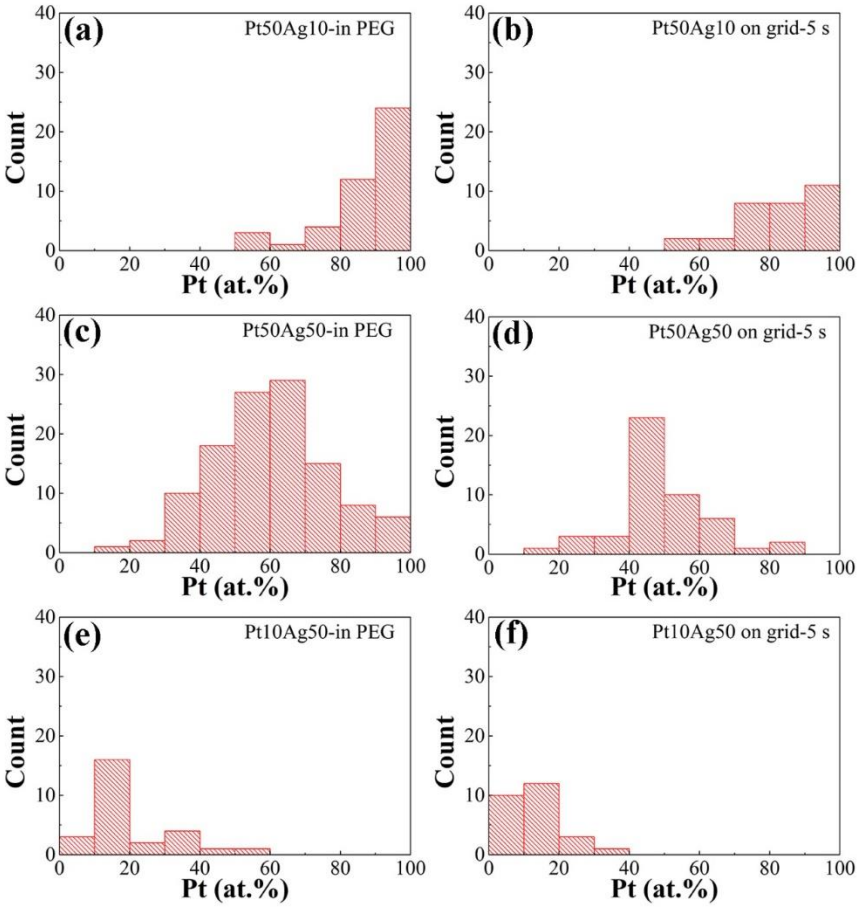

Figure 2.21 Composition distributions of sample Pt50Ag10, Pt50Ag50, and Pt10Ag50 sputtered onto PEG (a, c, e) and on TEM grids for 5 s (b, d, f). The numbers of the NPs measured with STEM-EDX for plotting in Figures 2.21 a-f are 45, 31, 117, 49, 28, and 26, respectively.

For the samples sputtered onto PEG, the result showed that Pt50Ag10 contained Pt/Ag NPs with Pt of more than 50 at. % and a large number of pure Pt NPs, Pt10Ag50 contained Pt/Ag NPs with Pt less than 60 at. % and a small number of pure Ag NPs whereas the composition of Pt in Pt50Ag50 ranged from 10 to 100 at. % in standard Gaussian distribution without pure Ag but with a small number of pure Pt NPs. The average values of Pt content in Pt50Ag10, Pt50Ag50, and Pt10Ag50 sputtered onto

PEG were 85.1 ± 14.0, 60.2 ± 16.2, and 19.8 ± 12.2 at. %, respectively. This result revealed that a higher current of Pt leads to the higher content of Pt in Pt/Ag samples, which is consistent with the above XRD and HAADF results. Further, for each pair of sputtering currents, it was observed that the composition distributions of the samples sputtered onto PEG and on the TEM grid for 5 s shared a similar feature (the STEM-EDX mappings of samples with 5 s sputtering on grids are in Figures 2.22-2.24). Thus, it was suspected that the initial combination and nucleation in the vacuum and/or nucleation/growth on the PEG surface regulated the composition distributions. In particular, compositions of Pt50Ag10 and Pt10Ag50 were primarily determined by the element with a dominant population in the sputtering chamber via homogenous nucleation and growth by the collision of atoms/clusters from the same element. As a result, pure Pt and Ag were obtained in Pt50Ag10 and Pt10Ag50, respectively. When the amounts of the ejected Pt and Ag atoms are relatively sufficient and balanced to each other, as in Pt50Ag50, the atoms/clusters from different elements could combine more effectively at a higher probability during both nucleation and growth, thus, decreasing the amount of pure Pt and Ag and increasing Pt/Ag alloy NPs.

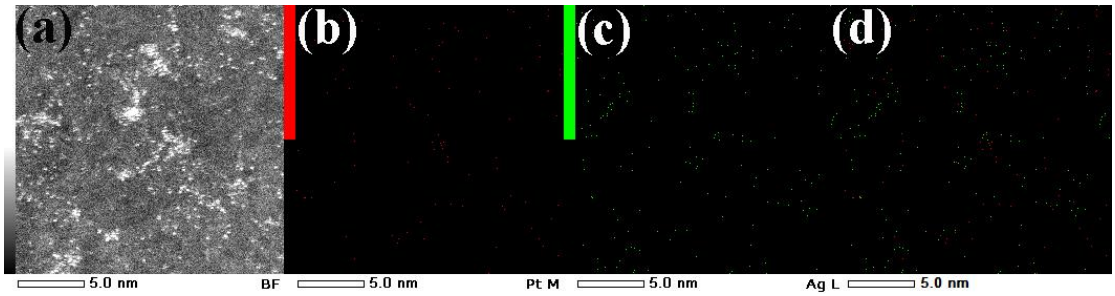

Figure 2.22 (a) HAADF and (b-d) STEM-EDX mapping images of Pt10Ag50 sample sputtered on TEM grid for 5 s with (b) Pt M, (c) Ag L, and (d) overlapping image of Pt and Ag. The average Pt atomic composition measured from STEM-EDX results is of

13.3 ± 8.0 at %.

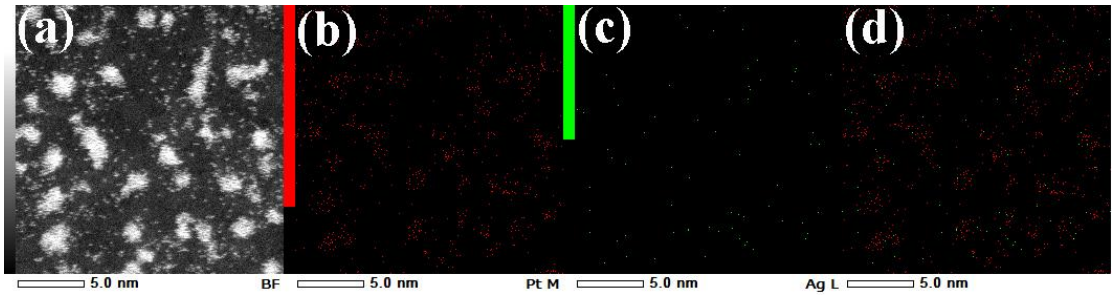

Figure 2.23 (a) HAADF and (b-d) STEM-EDX mapping images of Pt50Ag10 sample sputtered on TEM grid for 5 s with (b) Pt M, (c) Ag L, and (d) overlapping image of Pt and Ag. The average Pt atomic composition measured from STEM-EDX results is of 83.8 ± 11.2 at %.

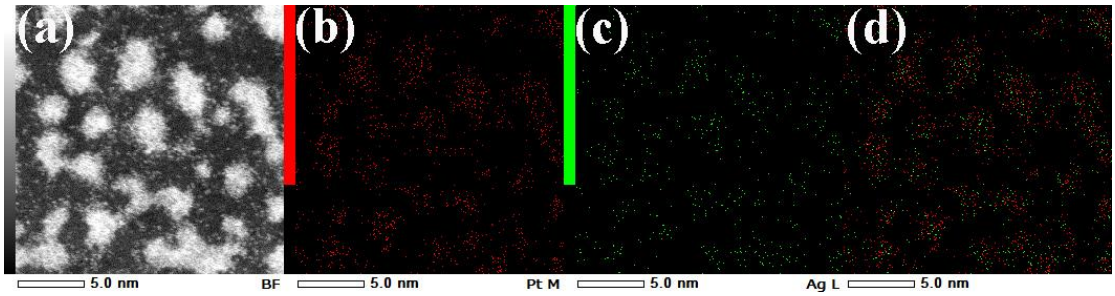

Figure 2.24 (a) HAADF and (b-d) STEM-EDX mapping images of Pt50Ag50 sample sputtered on TEM grid for 5 s with (b) Pt M, (c) Ag L, and (d) overlapping image of Pt and Ag. The average Pt atomic composition measured from STEM-EDX results is of 50.3 ± 13.0 at %.

Table 2.1 shows the nominal composition of Pt and Ag estimated from the weight of Pt and Ag sputtered on Al foils (Table 2.2). The Pt nominal compositions of Pt50Ag10, Pt50Ag50, and Pt10Ag50 are 90.9, 55.9, and 11.9 at. %, respectively. Sample Pt50Ag50

sputtered in PEG had Pt content of 60.2 ± 16.2 at. %, close to the nominal composition (55.9 at. %), whereas bigger differences between the nominal and measured Pt at. % of Pt/Ag NPs in PEG were observed for samples Pt50Ag10 and Pt10Ag50. Especially, in Pt10Ag50 sputtered in PEG, agglomerates of Ag (Figure 2.5) further decreased the content of Ag in Pt/Ag alloy NPs and made the composition of Pt became higher than the nominal value. On the other hand, there may exist some pure and small Pt NPs and/or nanoclusters in sample Pt50Ag10 sputtered onto PEG of which the composition could not be measured accurately in STEM-EDS, leading to a lower composition of Pt in the alloy NPs compared to the nominal value.

2.3.6 Relation of Composition Distribution, Particle Size, and Particle Formation in Pt/Ag NPs

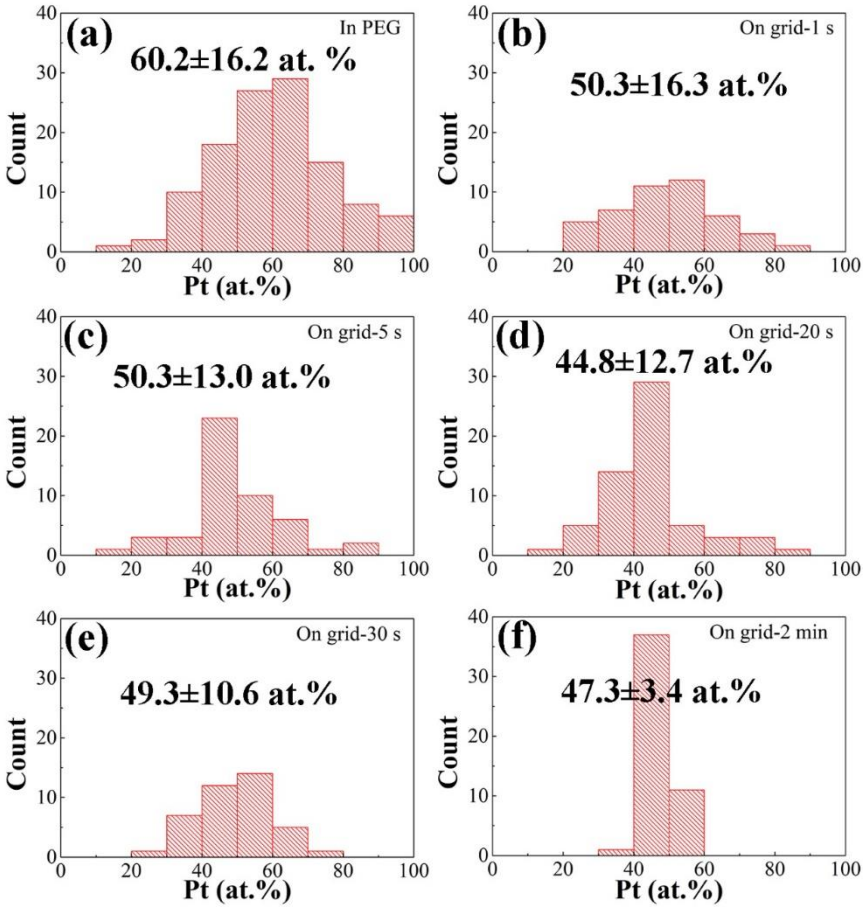

Figure 2.25 Composition distributions of (a) Pt50Ag50 sputtered in PEG for 30 min and Pt50Ag50 sputtered on grid for (b) 1 s, (c) 5 s, (d) 20 s, (e) 30 s and (f) 2 min.

To investigate the impact of PEG on the particle composition and growth as well as the impact of particle growth on the composition distribution, the composition and size distribution of Pt50Ag50 NPs sputtered onto PEG were compared with that on TEM grids for different sputtering times (1 s-2 min) as shown in Figure 2.25. The compositions from STEM-EDS mappings (Figures 2.25-2.29) were collected by measuring single particles or grains of about 2 nm (in the 30 s and 2 min sputtering). The composition distributions of the samples sputtered on the TEM grids became narrower along with the increase of the particle sizes for a longer sputtering time from

1.4 (1 s) to 2.6 nm (20 s) and bigger sizes with aggregation, necking (30 s), and connecting matrix (2 min sputtering) (Figure 2.15). This suggested that Pt atoms and Ag atoms randomly distributed and combined initially in a wide composition distribution and small particle size. On the solid substrate, these particles could not move. Thus, as sputtering time increased, the small NPs combined with more sputtered atoms. Consequently, the particle size became bigger and composition at one position (grain) became more uniform. It was observed that the sample Pt50Ag50 obtained in PEG had the composition distribution close to that obtained by sputtering on the TEM grid for 5 s and 20 s but broader than Pt50Ag50 sputtered on TEM grids for longer times (30 s, 2 min). The particle size of the sample in PEG (1.8 ± 0.3 nm, Figure 2.2) was somehow larger than that of Pt/Ag NPs sputtered on TEM grid for 5 s (1.6 ± 0.3 nm) and much smaller than that on the TEM grids for 20 s (2.6 ± 0.3 nm) (Figure 2.15) or more. This result indicated that PEG could hinder the formed NPs from combining with other atoms/clusters and growing to bigger sizes, to some extent. Hence, PEG supported the formation and growth of NPs with more uniform sizes. The effect comes from the high viscosity of PEG and its binding to NPs via the terminal –OH group and O in -CH_2-CH_2-O- units as suggested by Hatakeyama et al.[28] The -CH_2-CH_2- units of PEG can surroundadd a steric hindrance to NPs.[28] We observed a bigger size and some agglomerations of Pt50Ag50 NPs sputtered in silicone oil (KF-96-100cs, Shin-Etsu) of similar viscosity with PEG but without –OH and -CH_2-CH_2-O- units to stabilize NPs (Figure 2.30). Further, the results of composition distribution and size are in good agreement with the above hypothesis that the composition distribution of this sample is

regulated by the initial nucleation and growth of Pt/Ag clusters in the vacuum and/or PEG surface.

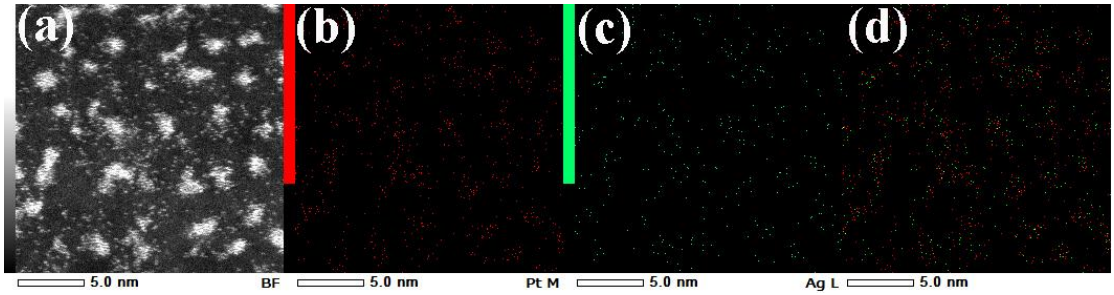

Figure 2.26 (a) HAADF and (b-d) STEM-EDX mapping images of Pt50Ag50 sample sputtered on TEM grid for 1 s with (b) Pt M, (c) Ag L, and (d) overlapping image of Pt and Ag. The average Pt atomic composition measured from STEM-EDX results is of 50.3 ± 16.3 at %.

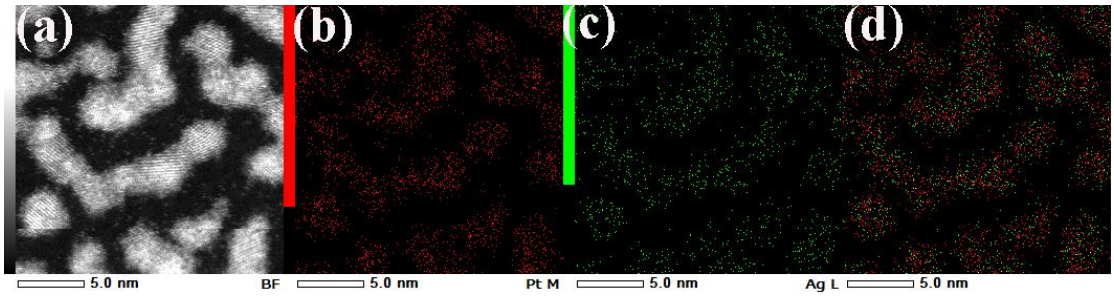

Figure 2.27 (a) HAADF and (b-d) STEM-EDX mapping images of Pt50Ag50 sample sputtered on TEM grid for 20 s with (b) Pt M, (c) Ag L, and (d) overlapping image of Pt and Ag. The average Pt atomic composition measured from STEM-EDX results is of 44.8 ± 12.7 at %.

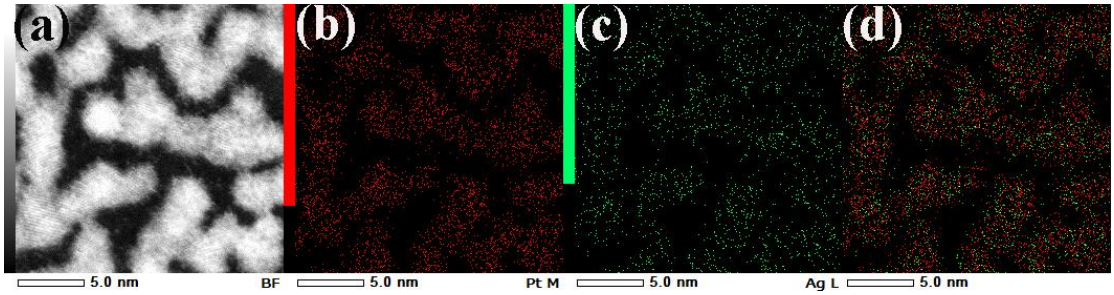

Figure 2.28 (a) HAADF and (b-d) STEM-EDX mapping images of Pt50Ag50 sample sputtered on TEM grid for 30 s with (b) Pt M, (c) Ag L, and (d) overlapping image of Pt and Ag. The average Pt atomic composition measured from STEM-EDX results is of 49.3 ± 10.6 at %.

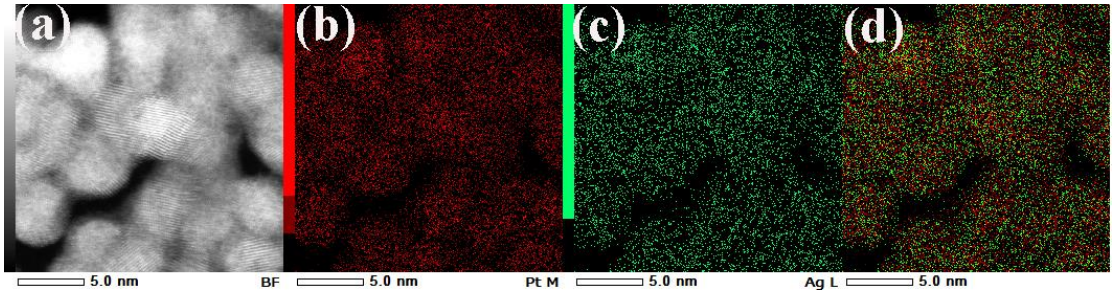

Figure 2.29 (a) HAADF and (b-d) STEM-EDX mapping images of Pt50Ag50 sample sputtered on TEM grid for 2 min with (b) Pt M, (c) Ag L, and (d) overlapping image of Pt and Ag. The average Pt atomic composition measured from STEM-EDX results is of 47.3 ± 3.4 at %.

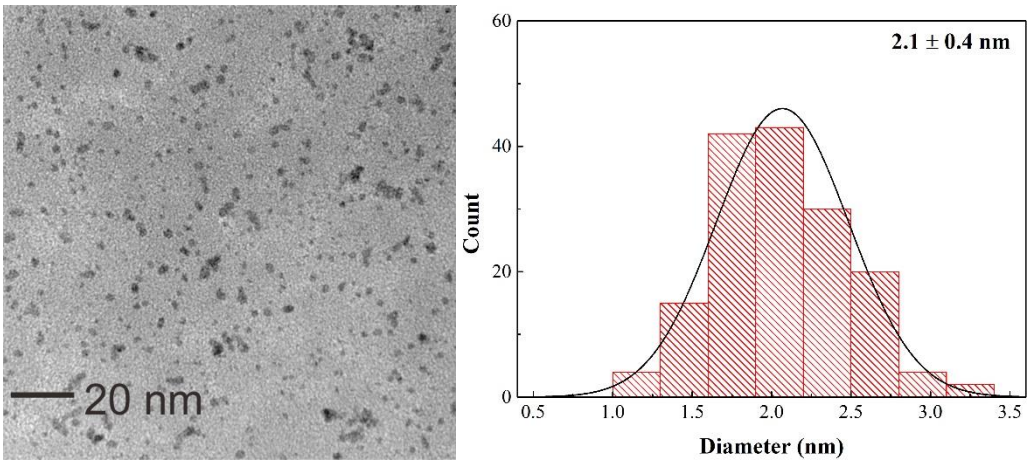

Figure 2.30 TEM image and size distribution of Pt50Ag50 NPs sputtered onto silicone oil for 30 min.

2.4 Conclusion

In this work, Pt/Ag alloy NPs were successfully synthesized by co-sputtering method and the alloy NPs were proved to be solid-solution of PtAg. The average sizes Pt/Ag samples had no obvious change with different sputtering currents in the range of 10-50 mA. However, the sputtering currents could affect the peak positions in XRD results, which was mainly caused by the distribution of the alloy composition in the samples. By comparing the composition distributions and size distributions of the samples sputtered onto PEG and on glass, it is found that PEG could hinder the NPs from growing to larger sizes as well as agglomerating. However, this also contributed to the formation of the broader size distribution of Pt/Ag NPs formed in PEG compared with NPs and thin films formed on TEM solid substrates or glass. The relationship between the sputtering currents, thereby particle compositions, and the formation of the samples, can pave the way to a better understanding of the solid solution alloy formation via sputtering technique onto liquid polymer.

2.5 References

1. Li, Y.; Gao, W.; Ci, L.; Wang, C.; Ajayan, P. M. Catalytic performance of Pt nanoparticles on reduced graphene oxide for methanol electro-oxidation. *Carbon* **2010**, *48*, 1124-1130.
2. Mostafa, S.; Behafarid, F.; Croy, J. R.; Ono, L. K.; Li, L.; Yang, J. C.; Frenkel, A. I.; Cuenya, B. R. Shape-dependent catalytic properties of Pt nanoparticles. *J. Am. Chem. Soc.* **2010**, *132*, 15714-15719.
3. Liu, Z.; Gan, L. M.; Hong, L.; Chen, W.; Lee, J. Y. Carbon-supported Pt nanoparticles as catalysts for proton exchange membrane fuel cells. *J. Power Sources* **2005**, *139*, 73-78.
4. Xiong, B.; Zhou, Y.; Zhao, Y.; Wang, J.; Chen, X.; O'Hayre, R.; Shao, Z. The use of nitrogen-doped graphene supporting Pt nanoparticles as a catalyst for methanol electrocatalytic oxidation. *Carbon* **2013**, *52*, 181-192.
5. Mu, Y.; Liang, H.; Hu, J.; Jiang, L.; Wan, L. Controllable Pt nanoparticle deposition on carbon nanotubes as an anode catalyst for direct methanol fuel cells. *J. Phys. Chem. B* **2005**, *109*, 22212-22216.
6. Song, P.; Xu, H.; Yan, B.; Wang, J.; Gao, F.; Zhang, Y.; Shiraishi, Y.; Du, Y. Particle size effects of PtAg nanoparticles on the catalytic electrooxidation of liquid fuels. *Inorg. Chem. Front.* **2018**, *5*, 1174-1179.
7. Zhou, X.; Gan, Y.; Du, J.; Tian, D.; Zhang, R.; Yang, C.; Dai, Z. A review of hollow Pt-based nanocatalysts applied in proton exchange membrane fuel cells. *J. Power Sources* **2013**, *232*, 310-322.

8. Zhang, G.; Yang, Z.; Zhang, W.; Hu, H.; Wang, C.; Huang, C.; Wang, Y. Tailoring the morphology of Pt_3Cu_1 nanocrystals supported on graphene nanoplates for ethanol oxidation. *Nanoscale* **2016**, *8*, 3075-3084.
9. Fu, G.; Xia, B.; Ma, R.; Chen, Y.; Tang, Y.; Lee, J. Trimetallic PtAgCu@PtCu core@shell concave nanooctahedrons with enhanced activity for formic acid oxidation reaction. *Nano Energy* **2015**, *12*, 824-832.
10. Zheng, L.; Yang, D.; Chang, R.; Wang, C.; Zhang, G.; Sun, S. Crack–tips enriched platinum–copper superlattice nanoflakes as highly efficient anode electrocatalysts for direct methanol fuel cells. *Nanoscale* **2017**, *9*, 8918-8924.
11. Zhang, B.; Zhang, Z.; Liao, H.; Gong, Y.; Gu, L.; Qu, X.; You, L.; Liu, S.; Huang, L.; Tian, X.; Huang, R.; Zhu, F.; Liu, T.; Jiang, Y.; Zhou, Z.; Sun, S. Tuning Pt-skin to Ni-rich surface of Pt_3Ni catalysts supported on porous carbon for enhanced oxygen reduction reaction and formic electro-oxidation. *Nano Energy* **2016**, *19*, 198-209.
12. Li, Z.; Li, Y.; He, C.; Shen, P. K. Bimetallic PtAg alloyed nanoparticles and 3-D mesoporous graphene nanosheet hybrid architectures for advanced oxygen reduction reaction electrocatalysts. *J. Mater. Chem. A* **2017**, *5*, 23158-23169.
13. Dutta, S.; Ray, C.; Sasmal, A. K.; Negishi, Y.; Pal, T. Fabrication of dog-bone shaped Au NR_{core}–Pt/Pd_{shell} trimetallic nanoparticle-decorated reduced graphene oxide nanosheets for excellent electrocatalysis. *J. Mater. Chem. A* **2016**, *4*, 3765-3776.
14. Mahmood, A.; Xie, N.; Din, M. A. U.; Saleem, F.; Lin, H.; Wang, X. Shape

controlled synthesis of porous tetrametallic PtAgBiCo nanoplates as highly active and methanol-tolerant electrocatalyst for oxygen reduction reaction. *Chem. Sci.* **2017**, *8*, 4292-4298.

15. Chen, Q.; Cao, Z.; Du, G.; Kuang, Q.; Huang, J.; Xie, Z.; Zheng, L. Excavated octahedral Pt-Co alloy nanocrystals built with ultrathin nanosheets as superior multifunctional electrocatalysts for energy conversion applications. *Nano Energy* **2017**, *39*, 582-589.
16. Karakaya, I.; Thompson, W. T. The Ag-Pt (Silver-Platinum) system. *Bull. Alloy Phase Diagrams* **1987**, *8*, 334-340.
17. Fu, T.; Fang, J.; Wang, C.; Zhao, J. Hollow porous nanoparticles with Pt skin on a Ag–Pt alloy structure as a highly active electrocatalyst for the oxygen reduction reaction. *J. Mater. Chem. A* **2016**, *4*, 8803-8811.
18. Ramirez-Caballero, G. E.; Ma, Y.; Callejas-Tovar, R. and Balbuena, P. B. Surface segregation and stability of core–shell alloy catalysts for oxygen reduction in acid medium. *Phys. Chem. Chem. Phys.* **2010**, *12*, 2209-2218.
19. Peng, Z.; You, H.; Yang, H. An electrochemical approach to PtAg alloy nanostructures rich in Pt at the surface. *Adv. Funct. Mater.* **2010**, *20*, 3734-3741.
20. Douk, A. S.; Saravani, H.; Noroozifar, M. One-pot synthesis of ultrasmall Pt-Ag nanoparticles decorated on graphene as a high-performance catalyst toward methanol oxidation. *Int. J. Hydrogen* **2018**, *43*, 7946-7955.
21. Lam, B. T. X.; Chiku, M.; Higuchi, E.; Inoue, H. PtAg Nanoparticle Electrocatalysts for the Glycerol Oxidation Reaction in Alkaline Medium. *Adv.*

Nanopart. **2016**, *5*, 167-175.

22. Yousaf, A. B.; Imran, M.; Zeb, A.; Wen, T.; Xie, X.; Jiang, Y. Single Phase PtAg Bimetallic Alloy Nanoparticles Highly Dispersed on Reduced Graphene Oxide for Electrocatalytic Application of Methanol Oxidation Reaction. *Electrochim. Acta* **2016**, *197*, 117-125.
23. Ishida, Y.; Corpuz, R. D.; Yonezawa, T. Matrix Sputtering Method: A Novel Physical Approach for Photoluminescent Noble Metal Nanoclusters. *Acc. Chem. Res.* **2017**, *50*, 2986−2995.
24. Nguyen, M. T.; Yonezawa, T. Sputtering onto a liquid: interesting physical preparation method for multi-metallic nanoparticles. *Sci. Technol. Adv. Mater.* **2018**, *19*, 883-898.
25. Ye, G.; Zhang, Q.; Feng, C.; Ge, H.; Jiao, Z. Structural and electrical properties of a metallic rough-thin-film system deposited on liquid substrates. *Phys. Rev. B* **1996**, *54*, 14754-14757.
26. Torimoto, T.; Okazaki, K.; Kiyama, T.; Hirahara, K.; Tanaka, N.; Kuwabata, S. Sputter deposition onto ionic liquids: Simple and clean synthesis of highly dispersed ultrafine metal nanoparticles. *Appl. Phys. Lett.* **2006**, *89*, 243117.
27. Torimoto, T.; Tsuda, T.; Okazaki, K.; Kuwabata, S. New Frontiers in Materials Science Opened by Ionic Liquids. *Adv. Mater.* **2010**, *22*, 1196-1221.
28. Hatakeyama, Y.; Morita, T.; Takahashi, S.; Onishi, K.; Nishikawa, K. Synthesis of Gold Nanoparticles in Liquid Polyethylene Glycol by Sputter Deposition and Temperature Effects on their Size and Shape. *J. Phys. Chem. C* **2011**, *115*, *8*, 3279–

3285.

29. Wender, H.; Gonçalves, R. V.; Feil, A. F.; Migowski, P.; Poletto, F. S.; Pohlmann, A. R.; Dupont, J.; Teixeira, S. R. Sputtering onto Liquids: From Thin Films to Nanoparticles. *J. Phys. Chem. C* **2011**, *115*, *33*, 16362–16367.
30. Hirano, M.; Enokida, K.; Okazaki, K.; Kuwabata, S.; Yoshida, H.; Torimoto, T. Composition-dependent electrocatalytic activity of AuPd alloy nanoparticles prepared via simultaneous sputter deposition into an ionic liquid. *Phys.Chem. Chem. Phys.* **2013**, *15*, 7286-7294.
31. König, D.; Richter, K.; Siegel, A.; Mudring, A.; Ludwig, A. High-Throughput Fabrication of Au–Cu Nanoparticle Libraries by Combinatorial Sputtering in Ionic Liquids. *Adv. Funct. Mater.* **2014**, *24*, 2049–2056.
32. Nguyen, M. T.; Yonezawa, T.; Wang, Y.; Tokunaga, T. Double Target Sputtering into Liquid: A New Approach for Preparation of Ag-Au Alloy Nanoparticles. *Mater. Lett.* **2016**, ***171***, 75-78.
33. Nguyen, M. T.; Zhang, H.; Deng, L.; Tokunaga, T.; Yonezawa, T. Au/Cu Bimetallic Nanoparticles via Double-Target Sputtering onto a Liquid Polymer. *Langmuir* **2017**, *33*, 12389-12397.
34. Deng, L.; Nguyen, M. T.; Shi, J.; Chau, Y. R.; Tokunaga, T.; Kudo, M.; Matsumura, S.; Hashimoto, N.; Yonezawa, T. Highly Correlated Size and Composition of Pt/Au Alloy Nanoparticles via Magnetron Sputtering onto Liquid. *Langmuir* **2020**, *36*, 3004-3015.
35. Chau, Y. R.; Nguyen, M. T.; Zhu, M.; Romier, A.; Tokunaga, T.; Yonezawa, T.

Synthesis of composition-tunable Pd–Cu alloy nanoparticles by double target sputtering. *New J. Chem.* **2020**, *44*, 4704-4712.

36. Vegard, L. Die Konstitution der Mischkristalle und die Raumfüllung der Atome. *Z. Phys.* **1921**, *5*, 17-26.
37. H. Okamoto. Ag-Pt (silver-platinum), *J. Phase Equilibria*, **1997**, *18* (5), 485.
38. G. L. W. Hart, L. J. Nelson, R. R. Valfleet, B. J. Campbell, M. H. F. Sluiter, J. H. Neethling, E. J. Olivier, S. Allies, C. I. Lang, B. Meredig, C. Wolverton. Revisiting the revised Ag-Pt phase diagram. *Acta Mater.* 2017, **124**, 325-332.
39. http://materialsproject.org (A. Jain*, S.P. Ong*, G. Hautier, W. Chen, W.D. Richards, S. Dacek, S. Cholia, D. Gunter, D. Skinner, G. Ceder, K.A. Persson *(*=equal contributions). The Materials Project: A materials genome approach to accelerating materials innovation.* APL Materials, 2013, 1(1), 011002.)
40. J. Pirat, A. Font, D. Rapetti, C. Andreazza-Vignolle, P. Andreazza, C. Mottet, R. Ferrando. Reversed size-dependent stabilization of ordered nanophases. *Nat. Commun.*, **2019**, *10*, 1982.
41. S. Suzuki, Y. Tomita, S. Kuwabata, T. Toromoto. Synthesis of alloy AuCu nanoparticles with the $L1_0$ structure in an ionic liquid using sputter deposition. *Dalton Trans.*, **2015**, *44*, 4186-4194.
42. Z. Peng, H. Yang. Ag-Pt alloy nanoparticles with the compositions in the miscibility gap. *J. Solid State Chem.*, **2008**, *181*, 1546-1551.

43. Handbook of X-ray Photoelectron Spectroscopy, JEOL 1991, Ed. by N. Ikeo, Y. Iijima, N. Nishimura, M. Sigematsu, T. Tazawa, S. Matsumoto, K. Kojima, Y. Nagasawa.

44. T. Diemant, K. M. Schüttler, R. J. Behm. Ag on Pt(111): Changes in Electronic and CO Adsorption Properties upon PtAg/Pt(111) Monolayer Surface Alloy Formation. *ChemPhysChem*, **2015**, *16*, 2943 – 2952.

45. N. Sui, K. Wang, X. Shan, Q. Bai, L. Wang, H. Xiao, M. Liu, V. L. Colvin, W. W. Yu. Facile synthesis of hollow dendritic Ag/Pt alloy nanoparticles for enhanced methanol oxidation efficiency. *Dalton Trans.*, **2017**, *46*, 15541–15548.

3 Co-sputtered CuPt/Ag alloy nanoparticles and comparative catalytic performance of mono-, bi-, and tri-metallic nanoparticles in oxygen reduction reaction

3.1 Introduction

Pt nanoparticles (NPs) have attracted a lot of attention due to excellent performances in electrochemical applications.[1,2] However, Pt is scarce and expensive. Fortunately, metallic alloys are widely applied as electrocatalysts and synthesized in a variety of ways.[2-8] Therefore, people have been working on alloying Pt with other cheaper metals and on more effective synthesis methods to avoid waste of Pt.[9-13] Sputtering is a conventional physical technique for preparing thin films on solid substrates from the bulk targets in vacuum and dry conditions.[14-18] In 1999, Wagner and Günter proposed the preparation of Fe and Ag nanoparticles by sputtering into an oil.[19] In 2006, Torimoto *et al.* obtained Au NPs by sputtering Au onto a capturing liquid such as an ionic liquid (IL).[20] These studies opened up a new method for the synthesis of metal NPs.[21-24] Various no or low volatile liquids such as ionic liquids, oils and liquid polymers can also be applied as capturing liquids.[18,25-27] Fluorescent metal clusters could also be obtained by sputtering with metal-coordinating ligands in a capturing liquid.[28-32] They also applied the method with single sputtering target containing two metals in alternative configuration to synthesize alloy nanoparticles with controllable composition in ILs.[24,33,34]

Co-sputtering simultaneously uses two or more metal targets to create metal alloy NPs.[34-36] This method does not require toxic chemical reductants and the alloy formation is not limited by the difference in redox potentials of metals.[34-36] Furthermore, the metal compositions of the alloy NPs can be controlled with more facility and versatility by adjusting the parameters such as the relative position of the liquid substrate with respect to the target, the applied sputtering powers and currents. König *et al*. obtained Au-Cu alloy NPs in ILs by co-sputtering wherein the particle composition was varied with the position of the cavities containing ILs in the vacuum chamber.[35] Chauvin et al. co-sputtered Au and Cu targets by varying the electric powers applied to Cu target to obtain Au, Cu oxide, and Au/Cu alloy NPs in pentaerythritol ethoxylate.[37] We successfully synthesized bimetallic Ag/Au, Cu/Au, Cu/Pd, Pt/Au, and Ag/Pt solid solution alloy NPs with tunable composition by co-sputtering onto liquid polyethylene glycol (PEG) and varying the sputtering currents applied to metal targets.[13,36,38-41] Besides, we also shed light on the formation mechanism of alloy NPs.[13] Synthesis of trimetallic alloy NPs by sputtering onto liquid has been reported by Cai *et al*.[42] They prepared PdAu/Pt NPs by successively sputtering onto ionic liquid (IL) containing carbon nanotubes and applied PdAu/Pt on carbon nanotube to methanol oxidation reaction (MOR). Pt-based NPs also showed good catalytic performance for other reactions.[43,44] However, there is still no report about using co-sputtering onto liquid substrates to synthesize trimetallic alloy NPs, their structure, and catalytic applications, which is the focus of the present paper.

Cu is not a noble metal. Both Cu and Ag are much cheaper than Pt (as of September 30, 2022, Cu: 7.64 USD per Kg, referred from https://markets.businessinsider.com/; Pt: 28148 USD per Kg, Ag: 618 USD per Kg, referred from https://www.kitco.com/). Alloying Pt with Ag and Cu can reduce cost and the amount of Pt in the catalyst. Moreover, our previous works demonstrated that co-sputtered Ag/Pt and Cu/Pt NPs are solid solution alloy throughout the miscibility gaps and intermetallic compositions.[13,39] In addition, alloying Pt with a second metal can modify the electronic and geometric structures of NPs and enhance their catalytic performance. Pt has been successfully alloyed with noble metals such as Au and Pd, as well as 3d transition metals such as Mn, Fe, Ni, Co, and Cu, to create enhanced ORR electrocatalysts[45-48]. R. Wojcieszak reported their discovery of synergetic effect of Au-Cu bimetallic catalysts, in which Cu can activate oxygen molecules[49]. And the excellent catalytic activity and stability of Pt/Ag alloy catalysts have also attracted much attention and been studied[50-54]. Thus, we can expect the formation of catalytically active Cu/Pt/Ag trimetallic solid solution alloy NPs by co-sputtering. PEG was chosen as the liquid substrate in the present study because it is cheap and does not strongly bind to the surface of NPs where electrochemical reactions occur. The latter is good in the sense that PEG can be washed away and does not block contacts between catalysts and electrolytes.[1]

In this paper, CuPt/Ag trimetallic solid solution alloy NPs were synthesized by co-sputtering using a CuPt alloy target (25 atom% Pt) and an Ag target. The alloy compositions were varied by adjusting the sputtering currents applied to Ag target. The

Cu to Pt ratios of the synthesized CuPt/Ag NPs were found to be smaller than that of CuPt target. The synthesized trimetallic alloy NPs were examined as catalysts for oxygen reduction reaction (ORR) in an acidic electrolyte. Compared with the sputtered Pt NPs and co-sputtered Ag/Pt bimetallic alloy NPs, bimetallic alloy CuPt NPs and trimetallic alloy CuPt/Ag NPs showed worse ORR performance, that is, lower onset ORR potential and smaller electron transfer number. This is caused by the oxidation and dealloying of Cu as well as the dissolution of the catalysts.

3.2 Experimental section

3.2.1 Materials

PEG (M. W. = 600, Junsei, Japan), CuPt alloy target (50 wt. % of Pt and 50 wt. % of Cu, 50 mm in diameter, 3 mm in thickness, Tanaka Precious Metals, Japan), Ag target (99.99 %, 50 mm in diameter, Tanaka Precious Metals, Japan), and transmission electron microscope (TEM) grids (Nisshin EM, Japan) were used for sputtering experiments. Vulcan XC 72 (Fuel Cell Earth), isopropyl alcohol (IPA, Junsei, Japan), Nafion^{TM} perfluorinated resin solution (5 wt% in mixture of lower aliphatic alcohol and 45 % water, Sigma-Aldrich, America), and Pt/C as the reference catalyst (5 wt.% Pt loading, Wako, Japan) were used for ORR catalytic test. Water was purified by an Organo Puric System (> 18 MΩ·cm).

3.2.2 Synthesis of CuPt/Ag alloy NPs

Before sputtering, PEG was stirred under vacuum at 650 rpm in a flask in an oil bath for 2 h to remove water and gases; the temperature of the oil bath was set at 90 °C. After that 10 mL of PEG was added into a petri dish with a diameter of 60 mm. The petri dish was then placed horizontally in the center of the sputtering vacuum chamber. A stirrer was put in the petri dish under the surface of PEG. To synthesize CuPt/Ag trimetallic alloy NPs, CuPt alloy target and Ag target were co-sputtered. The elemental ratios of CuPt/Ag NPs were controlled by adjusting the sputtering currents applied to Ag target (0 - 50 mA) while keeping the electrical current applied to CuPt target constant at 50 mA. When a glass slide was used as the substrate, it was placed in the center of the petri dish. The center of the petri dish was located at a distance of 110 mm from the two metal targets. PEG was stirred at 80 rpm. No stirring was carried out if glass slides were used. After several times of vacuum and purging with inert Ar to remove O_2, the pressure of the vacuum chamber was kept at 2 Pa. Cooling ethanol of 4 °C was used for cooling the metal targets during sputtering. Before collecting the NPs, the metal targets were sputtered for 10 min to clean the surfaces. During cleaning, removable shutters were located in front of the metal targets and above the petri dish to prevent contamination from falling onto the PEG. The sputtering time was 30 min for collecting NPs in PEG. The sputtering system was equipped with a thermocouple and a temperature-controlled system to keep the substrate temperature at 30 °C. Samples are labeled as (CuPt)*x*Ag*y* according to the sputtering currents, *x* and *y* (mA), applied to the

CuPt and Ag targets, respectively. For example, sample (CuPt)50Ag10 was obtained by co-sputtering CuPt target at 50 mA and Ag target at 10 mA.

3.2.3 Characterization

UV-Vis spectra were collected immediately after sputtering deposition using a JASCO V-630 spectrophotometer and a quartz cuvette with an optical path of 1 mm. The baseline was collected using an empty quartz cuvette. The size and shape of the NPs were analyzed using TEM (JEOL JEM-2000FX, 200 kV) and scanning TEM (STEM, JEOL JEM-ARM200F, 200 kV and FEI Titan3 G2 60-300, 300 kV). Samples for TEM and STEM analysis were prepared by immersing TEM grids into NPs/PEG dispersions for 10 s, then immediately immersing the grids into ethanol for at least 20 min to remove excess PEG, and finally drying in air at room temperature for a few minutes. The size distributions were collected from TEM and STEM images by measuring approximately 150 particles in at least three different regions of the grid using ImageJ software. The crystal structure of NPs was evaluated using STEM high-angle annular dark-field (HAADF) images. The samples sputtered on glass slides were analyzed with X-ray diffraction (XRD, Rigaku Mini Flex II, Cu Kα radiation, $\lambda = 1.5418$ Å, scanning speed of 0.5° min^{-1}). The X-ray diffraction intensities for all samples were plotted as a function of 2 theta. Area analysis using energy-dispersive X-ray spectroscopy (EDS) coupled with STEM (JEOL JEM-ARM200F) was carried out to verify the existence of CuPt/Ag alloy NPs and their compositions. The metal compositions of NPs/PEG dispersions and metal loading on carbon of the catalysts were obtained by Inductively

Coupled Plasma-Atomic Emission Spectrometer (ICP-OES, Shimadzu ICPE-9000). For preparing the samples, aqua regia or nitric acid was added into 1 mL of NPs/PEG dispersion or 10 mg catalyst powders. Aqua regia was used to prepare samples for measuring Pt and Cu, and nitric acid was used to prepare samples for measuring Ag. The mixtures were then kept for at least 30 min. After the metals were entirely dissolved, the mixtures were centrifuged, the precipitates were discarded, and the supernatants were diluted to 10 mL for ICP-OES measurements. The durability of the catalysts after electrochemical tests were analyzed by X-ray photoelectron spectroscopy (XPS, JEOL, JPS-9200, Mg Ka source). The catalysts before and after electrochemical tests were collected and XPS was performed using 20 eV pass energy, and scanned 300 times.

3.2.4 Electro-catalytic test

For the preparation of catalysts, carbon (Vulcan XC 72) was added into the sputtered NPs/PEG dispersions. After that acetone was added into the mixture and the mixture was sonicated. The sample was then centrifuged, the precipitate was washed with acetone, and the process was repeated for two more times. Finally, the solid (NPs/C) was dried and used as catalysts. Catalyst inks were prepared by dispersing the dried NPs/C solids (3 mg) in solutions of pure water (0.6 mL), Nafion (0.15 mL), and IPA (2.25 mL) by. Before electrochemical tests, the catalyst ink (4 μL) was sonicated and dropcast onto a glassy carbon rotating disk electrode (RDE, 5 mm in diameter) using a pipette. Then the RDE was dried overnight.

The ORR electrochemical tests were performed in aqueous 0.1 M $HClO_4$ at 293 K using three-electrode system. Ag/AgCl in saturated (sat.) KCl and Pt wire are the reference and counter electrode, respectively. RDE with catalyst film is the working electrode. Ar was bubbled (100 mL/min) in the electrolyte for 30 min to obtain Ar sat. electrolyte. After cyclic voltammetry (CV) baseline was measured in Ar sat. electrolyte, O_2 was bubbled (100 mL/min) in the electrolyte for 30 min to obtain O_2 sat. electrolyte. The CV and linear sweep voltammetry (LSV) results in the O_2 sat. electrolyte were used to evaluate catalytic performance. CV was collected with a stationary electrode using a sweep rate of 10 mV s^{-1} from 1.1 to 0 V vs. RHE. LSV was measured using the RDE rotating at various rotation speeds (400, 900, 1225, 1600, 2025, 2500, and 3600 rpm) and a sweep rate of 5 mV s^{-1}. CV and LSV measurements were carried out without bubbling of Ar or O_2 gas. Electron transfer numbers (n) were calculated from the LSV results using Koutecký–Levich (K-L) plot and Levich equation (explained in SI). All reported potentials in this paper are referred to the reversible hydrogen electrode (RHE).

3.3 Results and Discussion

3.3.1 Morphology and Crystal Structure of the Sputtered NPs

Figure 3.1 shows the STEM-HAADF results of the co-sputtered samples. The NPs dispersed well in the PEG and no agglomeration was found in the images. The size distributions of the samples are presented in Figure 3.2. The average particle sizes and the sputtering currents of all samples are listed in Table 3.1. The average particle diameters of samples (CuPt)50Ag0, (CuPt)50Ag10, (CuPt)50Ag20, (CuPt)50Ag30,

(CuPt)50Ag40, and (CuPt)50Ag50 are 1.3 ± 0.3, 1.4 ± 0.4, 1.3 ± 0.3, 1.6 ± 0.5, 1.6 ± 0.4, and 1.9 ± 0.4 nm, respectively. In general, the particle sizes of CuPt/Ag increase with the increase of the sputtering current of Ag.

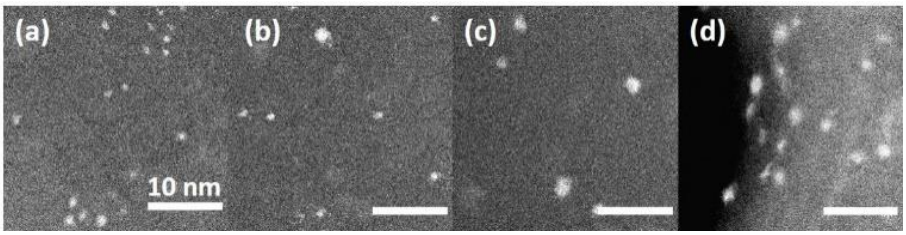

Figure 3.1 STEM-HAADF images of the CuPt/Ag NPs sputtered onto PEG for 30 min: (a) (CuPt)50Ag0, (b) (CuPt)50Ag10, (c) (CuPt)50Ag30, and (d) (CuPt)50Ag50. All scale bars are 10 nm.

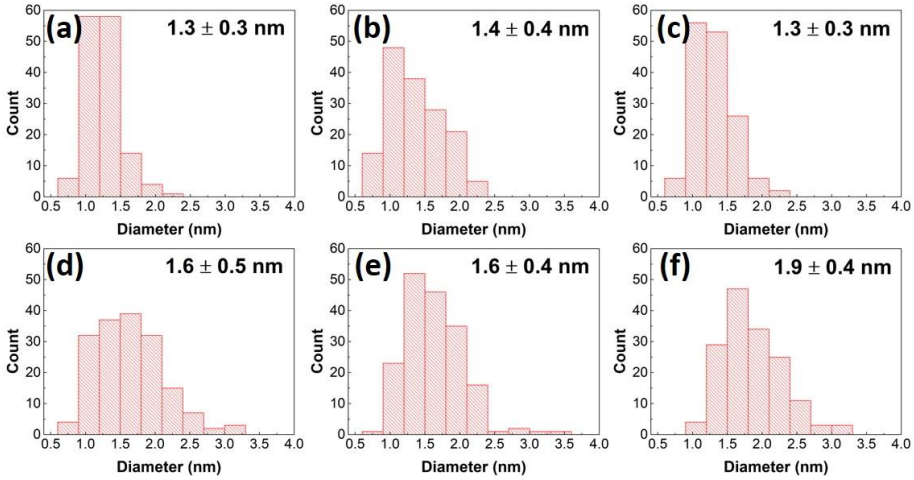

Figure 3.2 Size distributions and (inset) average sizes of Pt/Ag/Cu NPs sputtered onto PEG for 30 min: (a) (PtCu)50Ag0, 1.3 ± 0.3 nm; (b) (PtCu)50Ag10, 1.4 ± 0.4 nm; (c) (PtCu)50Ag20, 1.3 ± 0.3 nm; (d) (PtCu)50Ag30, 1.6 ± 0.5 nm; (e) (PtCu)50Ag40, 1.6 ± 0.4 nm; and (f) (PtCu)50Ag50, 1.9 ± 0.4 nm.

Table 3.1 Preparative conditions and sizes of CuPt/Ag NPs co-sputtered onto PEG

Sample	ICuPt (mA)	IAg (mA)	Particle diameter measured

			by TEM/STEM (nm)
(CuPt)0Ag50	0	50	2.8 ± 0.7 (TEM)
(CuPt)50Ag0	50	0	1.3 ± 0.3 (STEM)
(CuPt)50Ag10	50	10	1.4 ± 0.4 (STEM)
(CuPt)50Ag20	50	20	1.3 ± 0.3 (TEM)
(CuPt)50Ag30	50	30	1.6 ± 0.5 (STEM)
(CuPt)50Ag40	50	40	1.6 ± 0.4 (TEM)
(CuPt)50Ag50	50	50	1.9 ± 0.4 (STEM)

Figure 3.3 shows the UV-Vis spectra of the CuPt/Ag samples. (CuPt)0Ag50 NPs (only Ag NPs, 2.8 ± 0.7 nm, Figure 3.4) have a surface plasmon absorption peak at ≈420 nm, which is the characteristic property of Ag NPs. Note that Ag NPs > 1 nm show plasmon absorbance at about 400 nm or more.[55,56] The UV-Vis spectra of pure Pt, Ag and Cu NPs sputtered onto PEG are shown in Figure 3.5. There is an absorption shoulder at ~280 nm in the Pt spectrum. However, in the spectra of other CuPt/Ag samples (average particle size ⩾ 1.3 ± 0.3 nm), this typical peak does not appear, indicating the formation of CuPt/Ag alloy and without pure Ag NPs. The extinction increases in the order of (CuPt)50Ag0 < (CuPt)50Ag10 < (CuPt)50Ag30 < (CuPt)50Ag20 < (CuPt)50Ag40 < (CuPt)50Ag50. Thus, in general, the extinction of trimetallic CuPt/Ag NPs increases with the increase of sputtering currents applied to Ag target, suggesting that the extinction is related to the presence of more Ag in the alloy NPs. However, despite the fact that (CuPt)50Ag30 is expected to have a higher Ag content than

(CuPt)50Ag20, the extinction of (CuPt)50Ag30 is lower than that of (CuPt)50Ag20 sample. The reason for this is not clear, further investigation is still needed. Possibly, the increase of extinction by having Ag content in (CuPt)50Ag30 higher than in (CuPt)50Ag20 sample is compensated by larger particle sizes of (CuPt)50Ag30 (1.6 ± 0.5 nm) compared with (CuPt)50Ag20 (1.3 ± 0.3 nm). Especially, (CuPt)50Ag20 sample has a higher number of small clusters (< 1 nm) which contribute to increasing the extinction.[25,57]

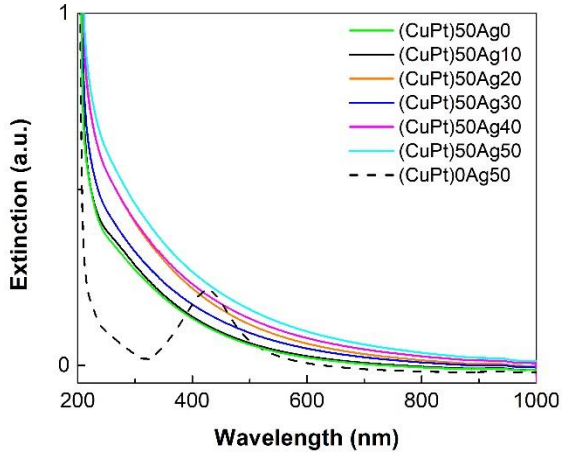

Figure 3.3 UV-Vis spectra of the co-sputtered (CuPt)50Ag0-50 and (CuPt)0Ag50 NPs in PEG.

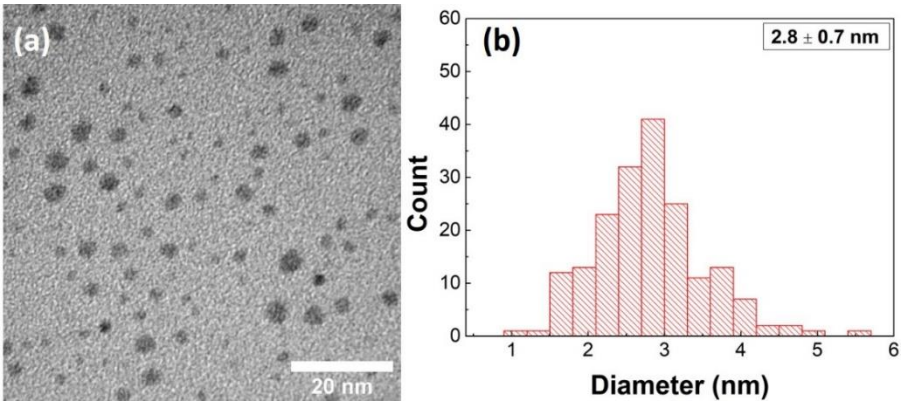

Figure 3.4 (a) TEM image and (b) size distribution of sample (CuPt)0Ag50 sputtered

onto PEG. The average size of this sample is 2.8 ± 0.7 nm.

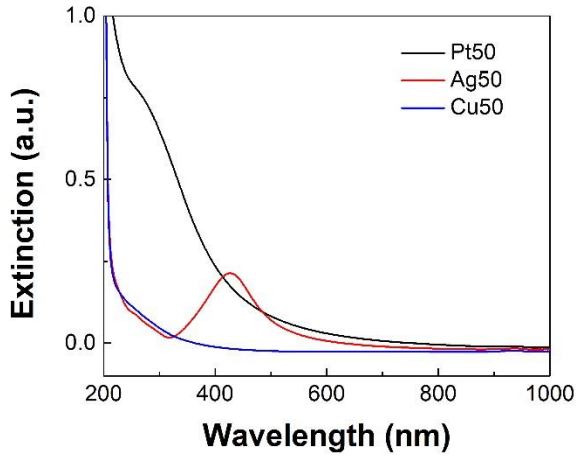

Figure 3.5 UV-Vis spectra of pure Pt, Ag and Cu NPs sputtered onto PEG with 50 mA sputtering current.

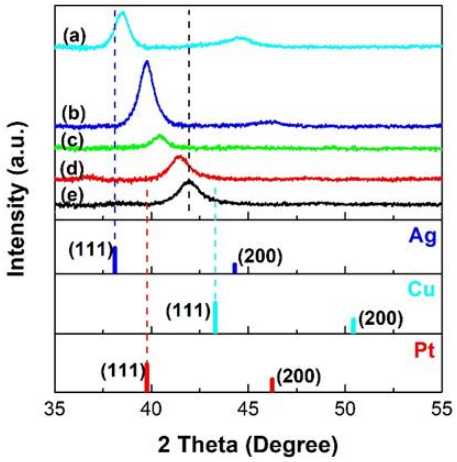

Figure 3.6 XRD patterns of (a) (CuPt)0Ag50, (b) (CuPt)50Ag50, (c) (CuPt)50Ag30, (d) (CuPt)50Ag10, and (e) (CuPt)50Ag0 samples synthesized by co-sputtering using Ag and CuPt alloy targets onto glass slides for 10 min. Reference patterns (stick patterns) of Ag (JCPDF No. 01-087-0597, blue), Cu (JCPDF No. 00-004-0836, cyan), and Pt (JCPDF No. 00-004-0802, red) are shown at the bottom of the figure with the peak index.

In order to analyze the crystal structure of the sputtered NPs using powder XRD, NPs should be separated from PEG. In general, the NPs/PEG dispersion was mixed with acetone and then centrifuged. However, because the co-sputtered CuPt/Ag NPs are small and stable in the PEG, they could not be separated from PEG by the mentioned method. Consequently, the sputtering experiments on the glass slides to obtain aggregation of NPs/thin film with larger material quantities were carried out.

Figure 3.6 shows the XRD patterns of the samples co-sputtered on the glass slides for 10 min. The (111) diffraction peak of sample (CuPt)50Ag0 is between the reference peaks of Pt and Cu, suggesting that it is a Cu/Pt solid solution alloy. The diffraction peaks of the trimetallic (CuPt)50Ag10-50 samples are between that of the samples (CuPt)50Ag0 and (CuPt)0Ag50, which are CuPt alloy and Ag, respectively. Particularly, in the range between (111) peaks of the reference Ag (2θ = 38.05°) and the sputtered Cu/Pt alloy (2θ = 41.94°, (CuPt)50Ag0 sample), each (CuPt)50Ag10-50 sample shows a single diffraction peak. Furthermore, as the sputtering currents applied to Ag target increases, the (111) peaks of the trimetallic samples shift towards that of Ag. These results suggest (CuPt)50Ag10-50 samples are trimetallic solid solution alloy. From the (111) XRD peak broadening, crystallite sizes were calculated as 5, 7, and 11 nm for (CuPt)50Ag10, (CuPt)50Ag30, and (CuPt)50Ag50 samples, respectively. TEM image of the trimetallic samples sputtered on the TEM grids for 10 min (Figure 3.7) show that they have film-like structures of NPs with average particle sizes of 5.4 nm ((CuPt)50Ag10), 8.4 nm ((CuPt)50Ag30), and 9.7 nm ((CuPt)50Ag50). This agrees

with crystallite sizes from XRD result. The lattice spacings of (111) planes of the trimetallic samples measured from SAED images (Figure 3.7) also increase with the increase of sputtering current applied to Ag target, which corresponds to the increase of Ag composition. Ag has atomic radius bigger than Pt and Cu, hence, trimetallic alloy NPs with a higher Ag content show a larger lattice spacing. Therefore, SAED result is consistent with the XRD results in showing the formation of solid solution alloy in CuPt/Ag NPs of sizes > 5 nm. It is noted that the (111) peak of (CuPt)0Ag50 (sputtered Ag) in XRD pattern shifts to a higher angle compared with that of reference Ag. This is possibly caused by the lattice contraction of sputtered Ag with small size (Figure 3.7).[58]

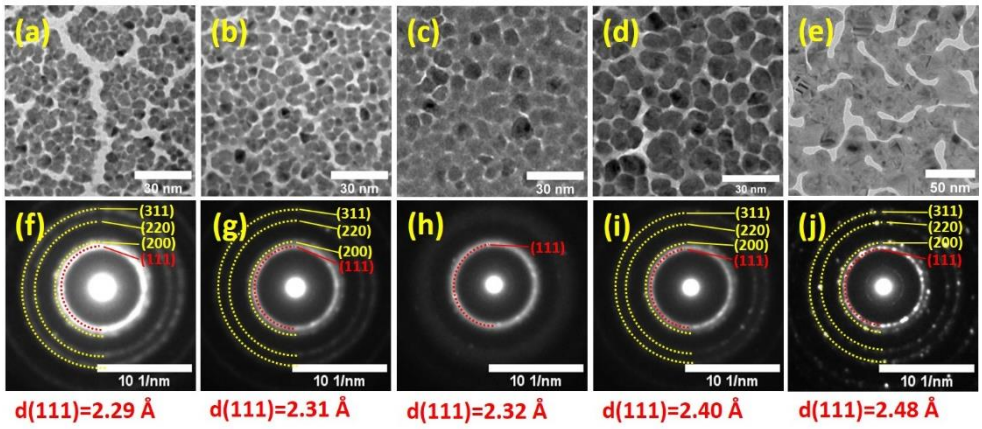

Figure 3.7 (a-e) TEM images and (f-j) SAED results of the samples co-sputtered on the TEM grids for 10 min: (a,f) (PtCu)50Ag0, (b,g) (PtCu)50Ag10, (c,h) (PtCu)50Ag30, (d,i) (PtCu)50Ag50, and (e,j) (PtCu)0Ag50. The lattice spacings of (111) planes of the corresponding samples are 2.29 Å, 2.31 Å, 2.32 Å, 2.40 Å, and 2.48 Å, as written below the SAED patterns.

The XRD, TEM, and SAED results of the samples sputtered on glass slides and TEM grids indicate that trimetallic alloy NPs (5-11 nm) were synthesized by co-sputtering. The sizes of trimetallic alloy NPs in the thin film on TEM grid/glass substrate (5-11 nm) are larger than trimetallic NPs synthesized in PEG (1.3-1.9 nm). It is known that atom diffusion and mixing to form alloy for small clusters/NPs are more facile than those for bigger particles. Hence, the small NPs sputtered onto PEG can be trimetallic alloy. In addition, as reported previously, the bimetallic alloy formed in the sputtering chamber before they grow on the solid surface or inside of PEG.[13] Therefore, with the formation of trimetallic alloy on glass slides and on TEM grids, we can expect trimetallic alloy formation when the substrate is liquid PEG. In order to check the fine structure and compositions of the NPs sputtered onto PEG, HAADF imaging and STEM-EDS were carried out and the results are discussed below.

3.3.2 Fine Structure and Composition of the Sputtered NPs

Fine structure of the co-sputtered trimetallic NPs was analyzed with STEM-HAADF images (Figure 3.8). Crystal structures of NPs were observed and the lattice spacings of (111) planes were 2.30, 2.32, and 2.35 Å for (CuPt)50Ag10, (CuPt)50Ag30, and (CuPt)50Ag50 NPs, respectively. The lattice spacings of the trimetallic NPs are between that of CuPt (2.29 Å, Figure 3.7) and Ag (2.36 Å, JCPDF No. 01-087-0597). The lattice spacing of each sample is distributed in a range (Figure 3.9). This is consistent with the fact that the composition of the sample is in a range (Figures 3.10 and 3.11). In addition, overall lattice spacing distributions shift to higher value with the

increase of the sputtering currents applied to Ag target. These results indicate the CuPt/Ag solid solution formation of a trimetallic alloy and is consistent with the XRD and SAED results of samples sputtered on solid substrates.

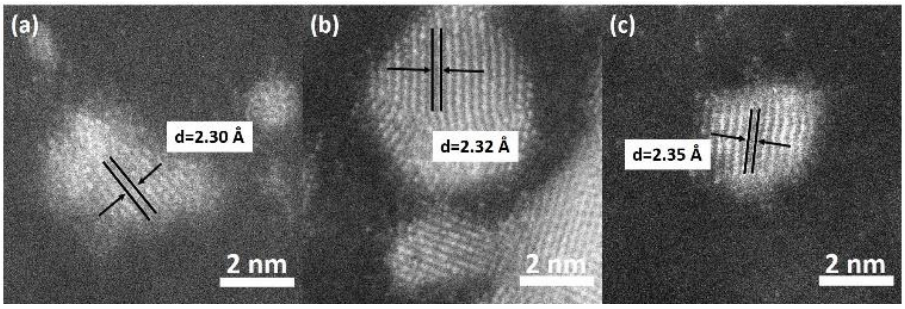

Figure 3.8 HAADF images of (a) (CuPt)50Ag10, (b) (CuPt)50Ag30, and (c) (CuPt)50Ag50 NPs and the lattice spacing values of (111) planes.

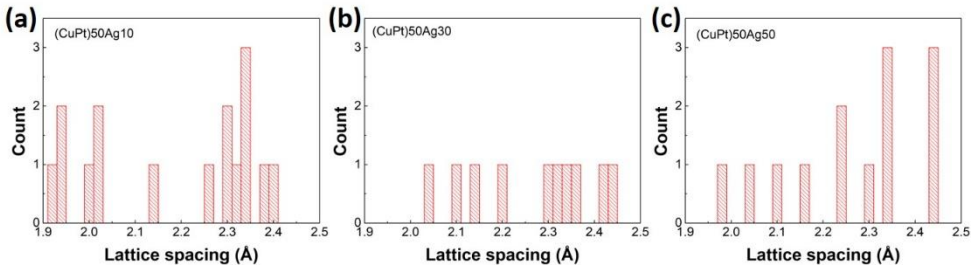

Figure 3.9 Lattice spacing distributions of the NPs co-sputtered onto PEG: (a) (CuPt)50Ag10, (b) (CuPt)50Ag30, and (c) (CuPt)50Ag50.

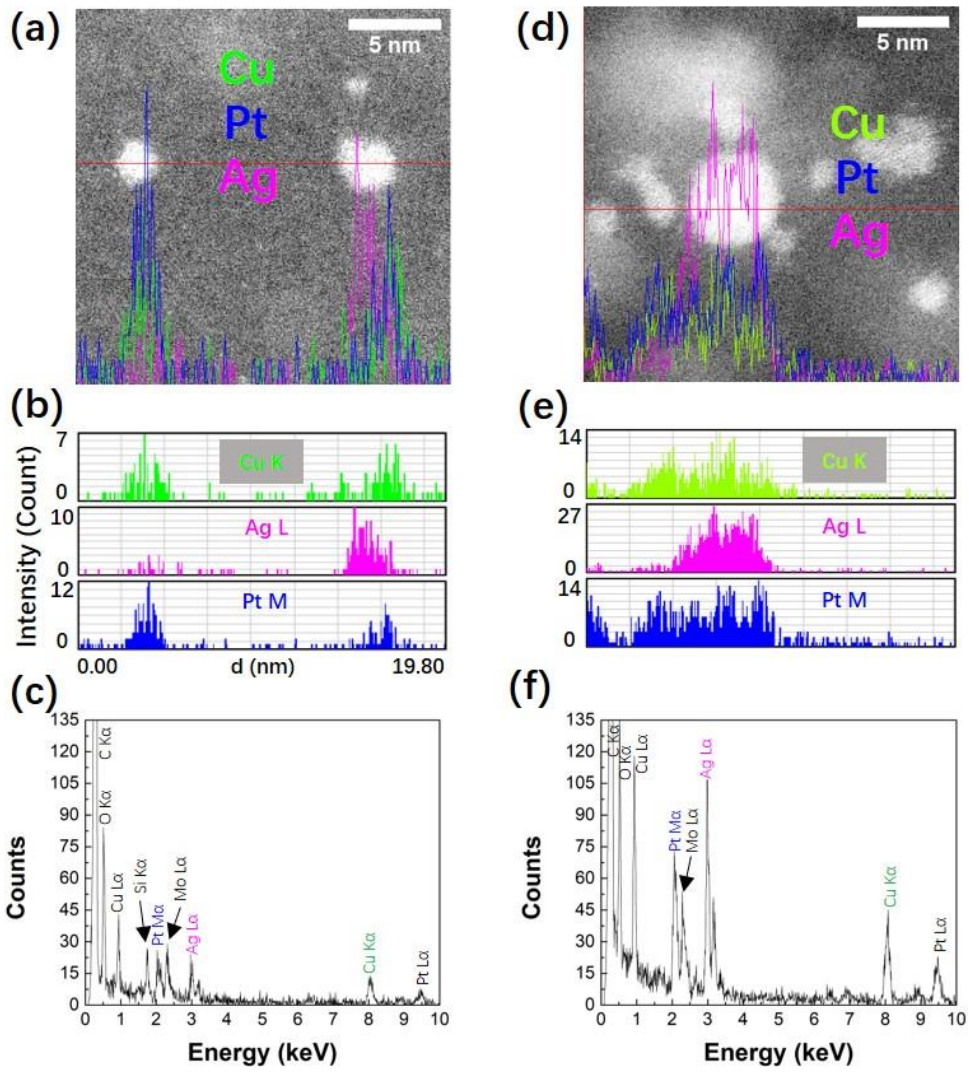

Figure 3.10 EDS elemental line profiles of (a,b) (CuPt)50Ag10 and (d,e) (CuPt)50Ag30 NPs sputtered onto PEG at the positions marked by red lines crossing the NPs in (a,d) HAADF images. EDS spectra corresponding to the line profile of (c) (CuPt)50Ag10 NPs shown in (a) and (f) (CuPt)50Ag30 NPs shown in (d). Color code in line profile and EDS spectra: green, blue, and magenta are for Cu Kα, Pt Mα, and Ag Lα, respectively.

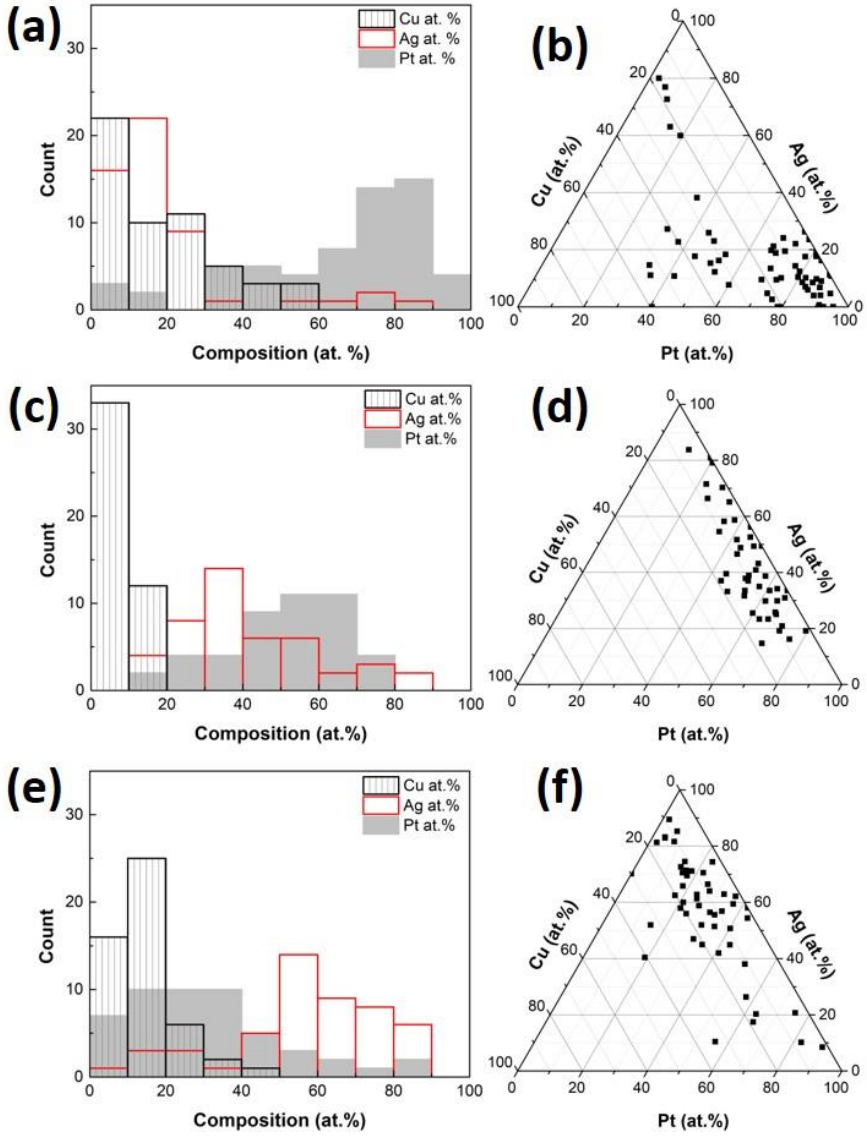

Figure 3.11 Composition distributions of the co-sputtered CuPt/Ag samples: (a,b) (CuPt)50Ag10, (c,d) (CuPt)50Ag30, and (e,f) (CuPt)50Ag50. Each data point in the scatter plot of Fig. 6b, 6d, and 6f represents the composition of a single NP measured by STEM-EDS and their locations in the triangular coordinate system represents the Cu, Pt, and Ag atom % of the NP.

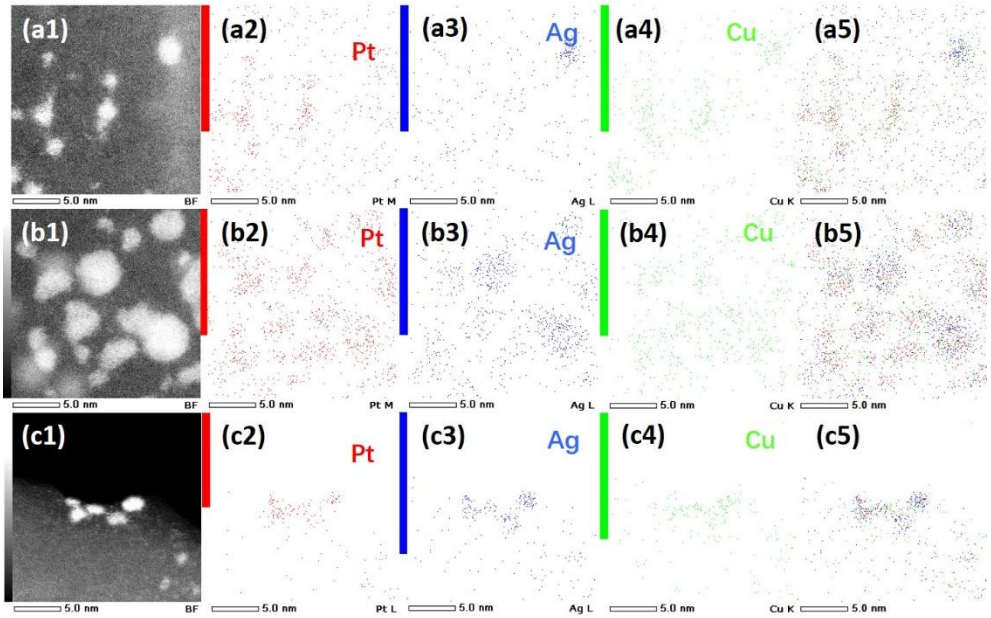

Figure 3.12 STEM-EDS mapping of (a1-a5) (PtCu)50Ag10, (b1-b5) (PtCu)50Ag30, and (c1-c5) (PtCu)50Ag50. Pt M for (a2) and (b2), Pt L for (c2), Ag L and Cu K. (a5, b5, c5) are overlapping images of Cu, Pt and Ag.

EDS elemental line profiles of samples (CuPt)50Ag10 and (CuPt)50Ag30 (Figure 3.10) show that Cu, Pt, and Ag co-exist in single NPs. The STEM-EDS mapping results of samples (CuPt)50Ag10, (CuPt)50Ag30, and (CuPt)50Ag50 are shown in Figure 3.12. The co-presence of Cu, Pt, and Ag in the NPs was confirmed. Note that the line profile of some NPs (e.g., NP on the right of Figure 3.10 a) shows that Cu, Pt, and Ag elements do not exactly overlap in the same position). This suggests that phase segregation exists in some NPs and/or the trimetallic alloy composition in single NPs is not uniform.

The compositions of single CuPt/Ag trimetallic alloy NPs sputtered onto PEG were analyzed using STEM-EDS area analysis. The number of measured NPs is 59, 45, and 50 for (CuPt)50Ag10, (CuPt)50Ag30, and (CuPt)50Ag50, respectively. Atomic

composition distributions and average compositions are shown in Figure 3.11 and Table 3.2, respectively. The metal compositions distributed in a wide range, because the atoms combine with each other randomly in the sputtering chamber and PEG. As the sputtering currents applied to Ag target increase, the Ag atom % of single NPs increases. This accompanies with the decrease of Pt atom%.

Table 3.2 Average compositions of co-sputtered CuPt/Ag samples in PEG

Composition		Samples			
		(CuPt)50Ag0	(CuPt)50Ag10	(CuPt)50Ag30	(CuPt)50Ag50
STEM -EDS	Cu (atom %)	13 ± 9	17 ± 15	7 ± 5	14 ± 8
	Pt (atom %)	87 ± 9	65 ± 24	51 ± 16	30 ± 20
	Ag (atom %)	0	18 ± 18	42 ± 18	56 ± 20
	Cu:Pt (mol/mol)	0.16:1	0.29:1	0.15:1	0.46:1
	Ag:Pt (mol/mol)	0:1	0.30:1	0.83:1	1.9:1
ICP-AES	Cu (atom %)	67.7	63.5	52.2	42.5
	Pt (atom %)	32.3	30.3	24.8	21.2

Ag (atom %)	0	6.2	23	36.3
Cu:Pt (mol/mol)	2.09:1	2.09:1	2.10:1	2.01:1
Ag:Pt (mol/mol)	0:1	0.20:1	0.93:1	1.72:1

However, the Cu atom % varies randomly among the samples. Moreover, the Cu contents (17 ± 15 atom% or less) are lower than Pt atom% (30 ± 20 atom% or more) with Cu:Pt of 0.46:1 (mol/mol) or less. These results are not expected because Cu and Pt were sputtered from a CuPt alloy target with higher Cu atom% than Pt atom% (75.4 atom% Cu, 24.6 atom% Pt, and Cu:Pt = 3.07:1 (mol/mol)). Previously, we obtained sputtered CuPt alloy with composition close to that of the CuPt target (76 atom % Cu) using a single head target sputtering onto glass for 30 min (70 atom% Cu as measured by XRF), on TEM grids for 30 s (72 - 76 atom% as measured by TEM-EDS), and onto PEG for 30 min (71 atom% Cu as inferred from lattice spacing from high resolution-TEM image of CuPt NPs of 2.2 ± 0.6 nm).[39] Note that the NPs which could be analyzed using STEM-EDS area analysis with accuracy in the present study are ≈ 0.8 nm or more. Thus, we suspected that the Cu composition of NPs measured in the present study could be affected by the limitation in the STEM-EDS analysis for small NPs (low signal and particle decomposition during observation) and the non-uniformity of the composition among single NPs in the samples. To verify the hypothesis, composition of

(CuPt)50Ag0 NPs of 1.3 ± 0.3 nm, which were sputtered using only CuPt alloy target in the double head sputtering system, was also measured. The sample has an average 13 ± 9 atom% Cu and 87 ± 9 atom% Pt (Table 3.2, Figure 3.13), which also shows lower Cu atom% than that of the alloy target. This confirms that the CuPt NPs measured using STEM-EDS with particles size of about 1.3 nm are Pt-rich. Small NPs of below ≈0.8 nm could have higher Cu content but could not be measured in STEM-EDS area analysis. We could not rule out a possibility that not all the sputtered Cu formed trimetallic alloy with Pt and Ag. In addition, to confirm the existence of Cu and/or Cu-rich trimetallic NPs in PEG dispersion, the average compositions of all sputtered NPs in PEG dispersion were measured using ICP-OES. The ICP results (Table 3.2) show that with the increase of the sputtering currents applied to Ag target, both Pt and Cu compositions decreased whereas Ag compositions increased as expected. Nevertheless, the ratios of Cu:Pt = 2:1 (mol/mol) remains similar in all the CuPt/Ag trimetallic samples and similar to that of the sputtered bimetallic Cu/Pt NPs obtained from only CuPt alloy target. This reflects the fact that the Cu:Pt molar ratio in the co-sputtered NPs/PEG dispersions is fixed as expected. This ratio is smaller than the Cu:Pt molar ratio of CuPt target (Cu:Pt = 3.07:1 (mol/mol)), further research is essential for understanding of this phenomenon.

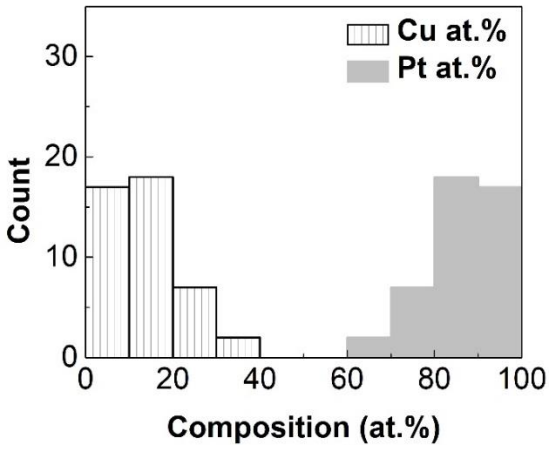

Figure 3.13 Composition distribution of sample (PtCu)50 sputtered onto PEG using Pt/Cu alloy target. The average compositions of Pt and Cu in the single particles of this sample are 87.2 ± 9.4 and 13.7 ± 9.1, respectively.

3.3.3 Catalytic performance

The co-sputtered (CuPt)50Ag30 NPs were loaded onto carbon as the support, henceforth labeled as (CuPt)50Ag30/C, for examining their ORR catalytic performance. The performance of CuPt/Ag trimetallic alloy NPs was compared with that of sputtered mono- (Pt) and bi-metallic ((CuPt)50Ag0 and Pt/Ag) NPs. Pt NPs (Pt50) were produced by sputtering of a Pt target onto PEG whereas Ag/Pt NPs (Ag50Pt50) were produced by co-sputtering of Ag and Pt targets onto PEG. Both samples were obtained using double-target head system with sputtering currents applied to metal target of 50 mA. Figure 3.14 shows the STEM-HAADF images of the catalysts on carbon. Except for Ag50Pt50 NPs which appeared aggregated on carbon (Figure 3.14 c), the other catalysts have NPs well dispersed on carbon (Figures 3.14 a, b, and d). Besides NPs, some atoms and small clusters of (CuPt)50Ag30 and (CuPt)50Ag0 samples are also visible.

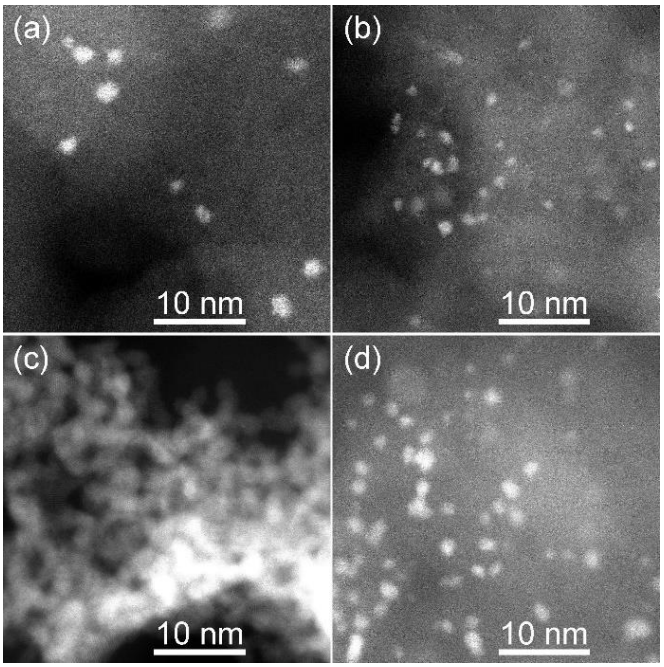

Figure 3.14 STEM-HAADF images of the sputtered NPs after loading onto carbon for (a) (CuPt)50Ag30/C, (b) (CuPt)50Ag0/C, (c) Ag50Pt50/C, and (d) Pt50/C catalys.

ORR catalytic performance of the NPs/C catalysts, *i.e.*, onset potentials and average electron transfer numbers (n) (Table 3.3), was estimated from CV (Figure 3.15 a and b) and LSV results at different rotation speeds and K-L plots (Figures 3.15 c and 3.16, Table 3.4). The results were compared with those of commercial Pt/C reference catalyst. The onset potentials of the catalysts decrease in order of Pt/C reference > Ag50Pt50 > Pt50 > (CuPt)50Ag30 > (CuPt)50Ag0. In addition, the electron transfer numbers decrease in order of Pt/C reference > Pt50 > Ag50Pt50 > (CuPt)50Ag30 > (CuPt)50Ag0.

Table 3.3 Electrochemical test results of the sputtered samples

Sample	(CuPt)50Ag30	(CuPt)50Ag0	Pt50Ag50	Pt50	Pt ref.
ORR onset potential (V)	0.71	0.58	0.74	0.72	0.77

Average eletron transfer number, n	2.9	-	3.3	3.6	4.0

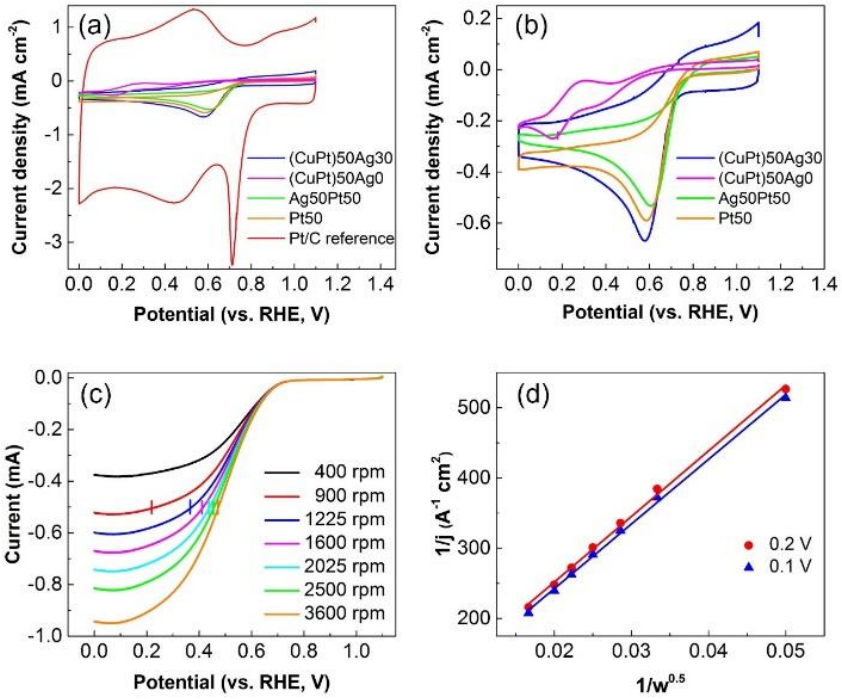

Figure 3.15 (a) CV curves of (CuPt)50Ag30/C (blue), (CuPt)50Ag0/C (magenta), Pt50Ag50/C (green), Pt50/C (orange), and Pt/C reference (red) catalysts. (b) Enlarged part from 0 to 1.2 V of CV curves in (a). (c) LSV curves at different rotation speeds and (d) K-L plot from results in (c) of (CuPt)50Ag30/C catalyst for calculating the electron transfer number.

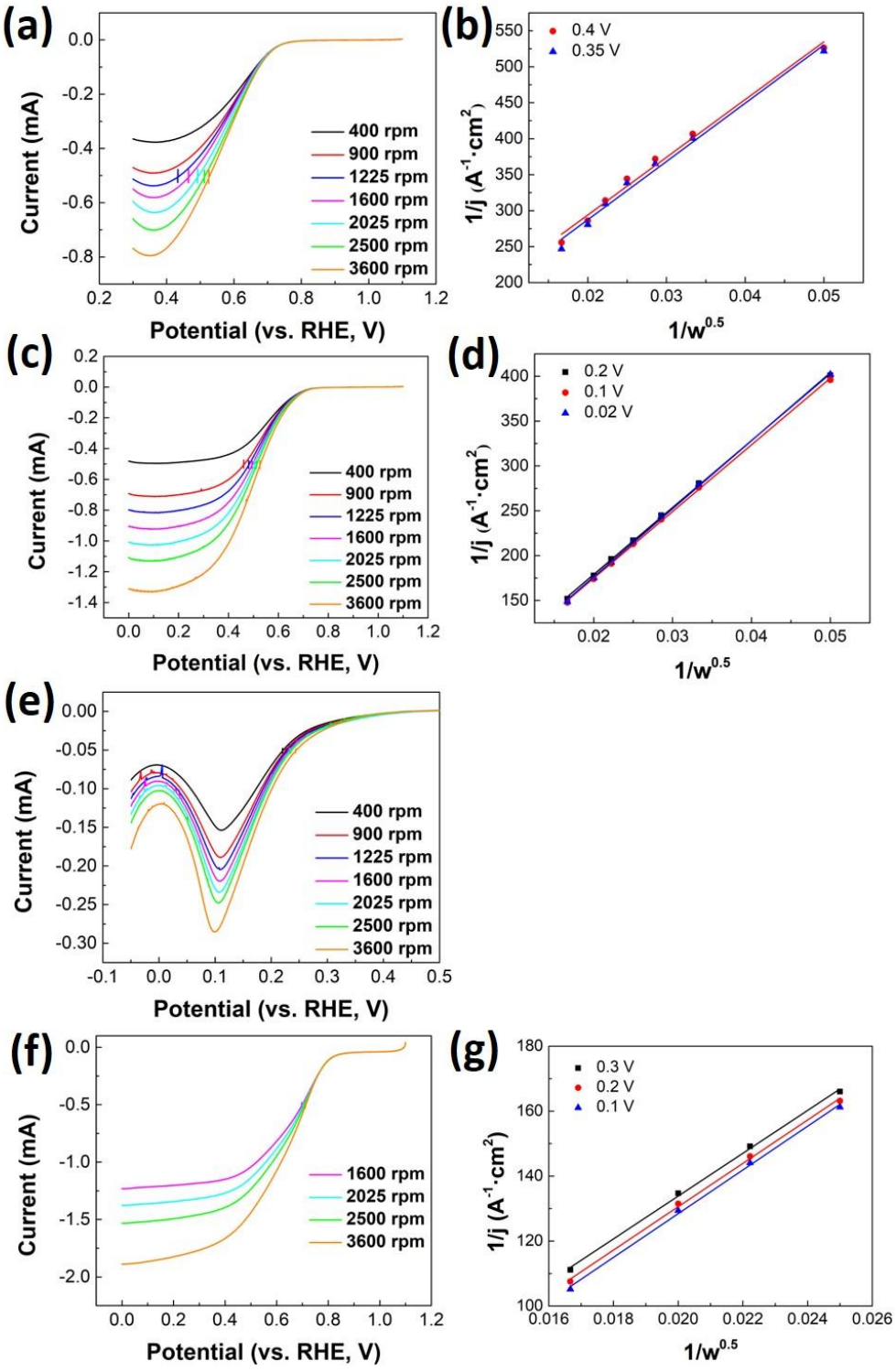

Figure 3.16 LSV curves at different rotation speeds for ORR and K-L plots of: (a,b) Ag50Pt50/C, (c,d) Pt50/C, (e) (PtCu)50/C, and (f,g) Pt/C reference catalysts.

Table 3.4 Electron transfer number (n) estimated at certain potential from LSV in Figure 3.16

Sample	(CuPt)50Ag30/C		Ag50Pt50/C		Pt50/C			Pt/C reference		
Potential (V)	0.2	0.1	0.4	0.35	0.2	0.1	0.02	0.3	0.2	0.1
n	2.8	2.9	3.3	3.3	3.6	3.6	3.5	4.0	4.0	3.9
Average	2.9		3.3		3.6			4.0		

Overall, our sputtered NP catalysts performed worse than the Pt/C reference catalyst. Among all the synthesized samples, (CuPt)50Ag0/C is the worst with the smallest onset potential and electron transfer number. Below 0.3 V in the CV curve of (CuPt)50Ag0, Cu reduction occurs (Figure 3.15 b). This indicates Cu in the (CuPt)50Ag0/C catalyst was oxidized and possibly contributed to its poor catalytic performance. Moreover, the dispersions of (CuPt)50Ag0 NPs on carbon significantly changed before and after electrochemical tests (Figure 3.17). Before the test (CuPt)50Ag0 NPs distributed evenly on carbon (Figure 3.17 a). However, after the test, although few NPs remain dispersed, most NPs aggregated (Figure 3.17 b and c). Furthermore, after electrochemical tests the STEM-EDS area analysis of the catalyst indicates that there is almost no Pt and only small amount of Cu (Figure 3.18). This means Pt and Cu dissolved in the electrolyte during the electrochemical tests. Previous reports also show that both Pt and the non-noble metal of Pt-based alloys dissolved into the electrolyte.[59,60] In our case, the amount of Cu in the catalysts is twice that of Pt (Table 3.2). This explains the observation that after dissolution of Cu and Pt, some Cu remained on the electrode whereas the small

amount of Pt could not be measured by EDS area analysis. The dissolution of Pt and Cu also contributed to the low catalytic performance of (CuPt)50Ag0/C catalyst.

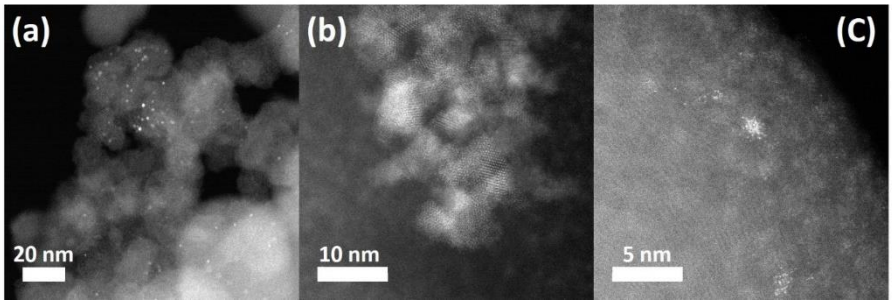

Figure 3.17 STEM-HAADF images of (a) (CuPt)50/C before electrochemical test and (b,c) (CuPt)50/C after electrochemical test.

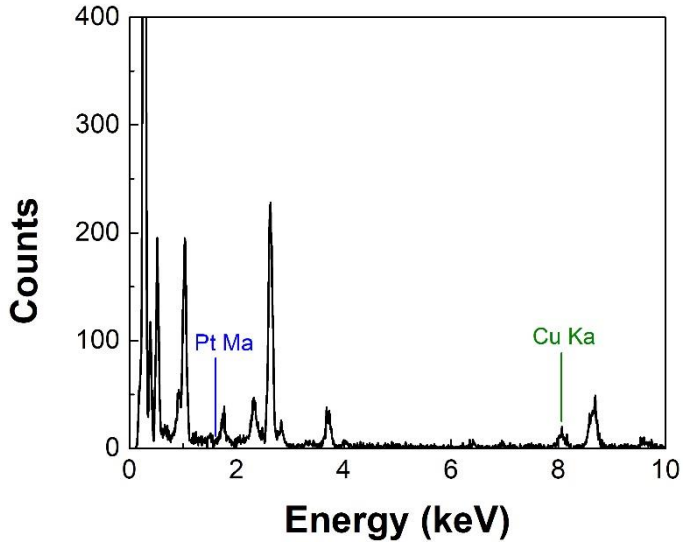

Figure 3.18 STEM-EDS area analysis spectrum of sample (CuPt)50Ag0, measured after electrochemical test. There is small amount of Cu remained, but Pt was not detected.

Trimetallic alloy (CuPt)50Ag30/C catalyst containing Ag outperformed the bimetallic alloy (CuPt)50Ag0/C one. It is noted that Cu:Pt molar ratio of the latter is higher than that of the former one (Table 3.5), suggesting more severe oxidation of Cu in the latter catalyst. Good dispersion of the trimetallic alloy NPs on carbon support and both Cu and Ag present in the trimetallic alloy NPs before and after ORR catalytic tests were confirmed in STEM-HAADF images and EDS line profiles (Figures 3.19-3.21). The trimetallic structure still existed in the NPs, and no significant shape or structure change was found, indicating that the NPs remained intact. This suggests that (CuPt)50Ag30 NPs have good composition and structure durability during ORR measurement, and alloying of CuPt with Ag improves the stability and performance of the catalyst compared with (CuPt)50Ag0/C.

Table 3.5 Metal loading on the carbon support of the catalysts before ORR from ICP results and Pt mass activity

Catalyst sample	**Metal loading on carbon (wt. %)**			**Cu:Pt (mol/mol)**	**Ag:Pt (mol/mol)**	**Pt mass activity ($A \cdot mg^{-2}$)**
	Cu	Pt	Ag			
(CuPt)50Ag30/C	0.121	0.138	0.095	2.69:1	1.24:1	3.9
(CuPt)50Ag0/C	0.123	0.0661	-	5.71:1	0	-
Ag50Pt50/C	-	0.682	0.246	0	0.65:1	0.6

Pt50/C	-	0.337	-	0	0	1.4
Pt/C reference	-	5	-	0	0	1.1

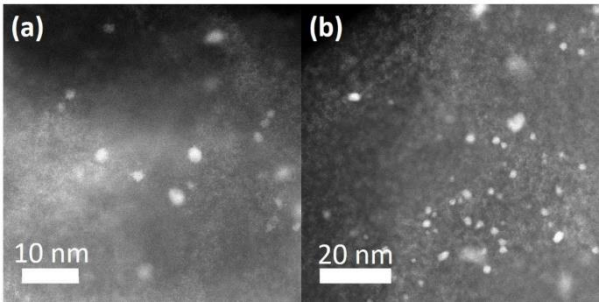

Figure 3.19 STEM-HAADF images of sample (CuPt)50Ag30/C after electrochemical test.

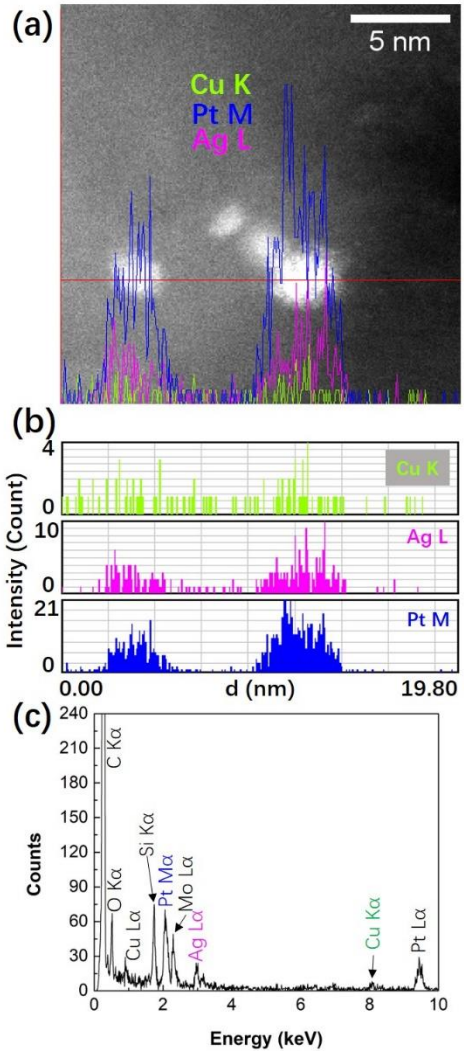

Figure 3.20 (a,b) EDS elemental line profiles of sample (CuPt)50Ag30/C before electrochemical test at the positions marked by red line crossing the NPs in (a) the HAADF image. (c) EDS spectrum of the line profile shown in (a,b).

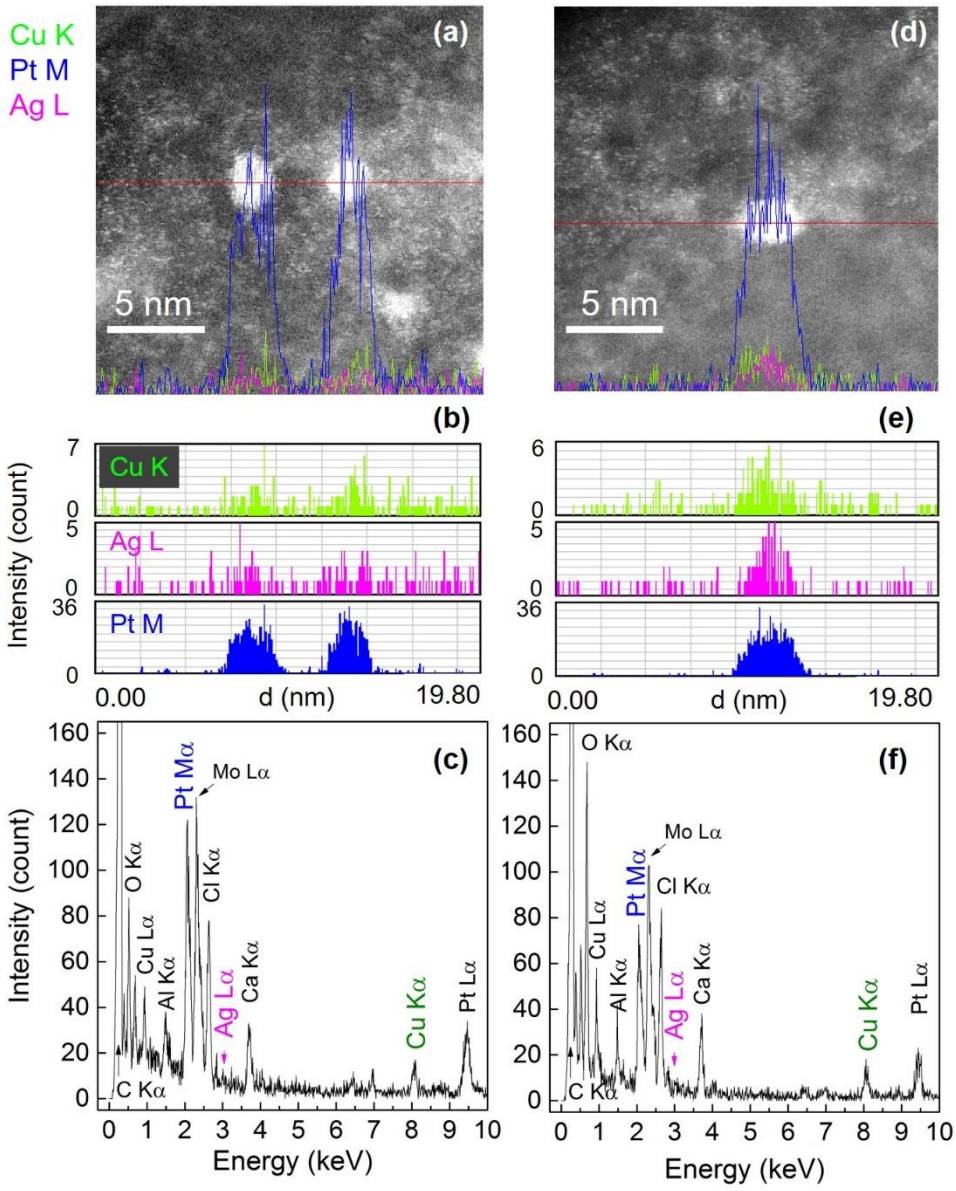

Figure 3.21 EDS elemental line profiles of sample (CuPt)50Ag30/C after electrochemical test for (a,b) two NPs and (d,e) one NP at the positions marked by red lines crossing the NPs in (a, d) HAADF images. EDS spectra corresponding to the line profile of (c) two NPs shown in (a) and (f) one NP shown in (d).

Regarding the onset potential, the sputtered Ag50Pt50 has a higher onset potential (0.74 V) than that of sputtered Pt50 (0.72 V) and (CuPt)50Ag30 (0.71 V). It is significant that although Ag50Pt50 NPs contain 40 atom% Ag (Table 3.5), they outperform Pt50 NPs.

It has been reported that the geometric (e.g., Pt-Pt interatomic distances) and electronic (ligand) parameters influence the catalyst's ORR activity via varying the adsorption of Pt with O_2 and the intermediate oxygenated species and suitable interaction is needed for enhanced catalytic performance.[62,63] These two factors can be present in our catalyst and can be considered in discussion of the obtained results. In our previous work[13], the sputtered Ag/Pt alloy NPs were found to have Pt 4f binding energy positively shifted and Ag 3d binding energy negatively shifted, according to the XPS results. This suggests the change of electronic structure of Pt by alloying with Ag with an increase of electron deficiency (e.g. Pt 5d-band vacancy), which is also reported by Feng et al.[62] Pure and/or small Pt NPs adsorb O_2 too strongly. Increased Pt electron deficiency would reduce electron back-donation from the Pt 5d-orbital to the adsorbed O_2, resulting in a weaker Pt–O interaction.[62] Appropriate weakening of Pt–O interaction can help improve the Pt activity toward the ORR.[62,63] Hence, the modification of the electronic structure of Pt and Ag via alloying can improve ORR performance of the Pt50Ag50 catalysts. In addition to the electronic effect caused by alloying, geometric effects, that is, a tensile strain of the lattice causes the d-band center of Pt to shift up, can affect the catalytic activity.[62,63] Since the lattice spacing of Ag is larger than that of Pt, the mismatch between Pt and Ag would lead to expansion of Pt lattice spacing with tensile strain, thus resulting in an upshift of the d-band center.[62] This upshift of the Pt d-band center would strengthen the binding of the oxygenated intermediates. This can decrease ORR activity by lowering the surface coverage.62,63 However, it should be noted that both d-band downshift and d-band upshift to improve ORR catalytic activity have been

suggested by researches[62–69] and the overall impact of the electronic structure modification of Pt and geometric effect by alloying on ORR activity remains a matter of debate. Possibly, the net impact of the electronic structure, geometric effect, particle size, and structural stability in Ag50Pt50 alloy NPs make them activate the ORR better than Pt in term of the overpotential. In addition, in order to obtain more detailed information, sample Ag50Pt50/C was chosen to for XPS measurements because of the highest metal loading on the carbon supports and its relatively higher catalytic activity among all the samples. The XPS results are shown in Figure 3.22. The Pt 4f and Ag 3d peaks can be seen in the XPS spectra of the sample before electrochemical tests. The spin–orbit splitting of the Pt 4f peaks are 3.3 eV (Pt $4f_{5/2}$ at 74.2 eV and Pt $4f_{7/2}$ at 70.9 eV), which is the characteristic of Pt. The XPS spectrum of Pt 4f after the electrochemical test was observed with similar intensity and peak position to that before the test. This indicates the chemical state of Pt is likely unchanged.

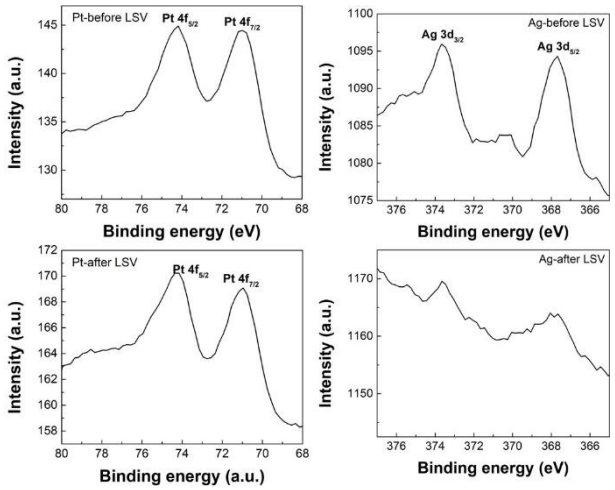

Figure 3.22 XPS spectra of sample Ag50Pt50/C before and after electrochemical tests.

However, the Ag 3d peaks after electrochemical tests were broad with low intensity compared with that before the test. This indicates that the Ag content is relatively lower. The Ag/Pt ratio of the sample after the electrochemical test measured by ICP is 0.33 : 1 (mol/mol), smaller than that of the catalyst before the experiments (0.65 : 1 (mol/mol)). The result is consistent with XPS results, suggesting that Ag was possibly dissolved in the electrolyte during the electrochemical tests. This may also account for the reason why sample Ag50Pt50/C performs worse than Pt50/C. (CuPt)50Ag30 NPs are also alloys, however, the onset potential is lower than that of Ag50Pt50. For one thing, the average particle size of (CuPt)50Ag30 NPs (1.6 nm) is smaller than that of Ag50Pt50 (1.8 nm), making them less active catalyst in the ORR; for another, the Cu oxidation in (CuPt)50Ag30 NPs also reduces their catalytic properties.

The electron transfer numbers (n) of (CuPt)50Ag30/C, Ag50Pt50/C, and Pt50/C are 2.9, 3.3 and 3.6, respectively, lower than that of commercial reference Pt (4.0). One possible reason is that the particle sizes of our sputtered samples (< 2 nm) are smaller than that of Pt/C reference catalyst (3.5 nm, Figure 3.23). It has been reported that Pt NPs with diameter of 3 nm have the optimized catalytic performances, because the NPs with this size have a maximum in mass activity.[1,61] The active sites for ORR of Pt NPs below 3 nm located on the terrace sites of the NPs decreases with particle size. Thus, decrease of particle size will decrease catalytic activity.[61] The average particle sizes of synthesized NPs are smaller than 2 nm whereas that of Pt reference is 3.5 nm. The size of Pt reference is closer to the ideal particle size for optimal ORR catalytic activity. For

the sputtered NPs, the average size of samples (CuPt)50Ag30 is 1.6 nm (Table 3.1), and the average sizes of Pt50 and Ag50Pt50 are 1.6 and 1.8 nm,[13] respectively. But electron transfer number of the Ag50Pt50 sample (n=3.3) is lower than that of Pt50 (n = 3.6). Further research is essential to shed light on these aspects for better understanding. One possibility is that geometric effects is more significant than the electronic effect caused by alloying of Pt with Ag, reducing the ORR in the 4-electron pathway. Moreover, the Pt compositions of the NPs decrease in the order of Pt50 > Ag50Pt50 > (CuPt)50Ag30. The NPs with higher Pt compositions, that is, more Pt nearby another Pt for simultaneous activation of two O, help enable the 4-electron pathway.[62] This may account for the fact that the electron transfer numbers of alloy NPs ((CuPt)50Ag30 and Ag50Pt50) are smaller than that of Pt50 NPs, and that of (CuPt)50Ag30 is smaller than that of Ag50Pt50. The oxidation of Cu in (CuPt)50Ag30 also leads to its smaller n compared to Pt50. The n values of the sputtered samples are between 2 and 4, which means during the electrochemical tests, two-electron and four-electron ORR occurred at the same time. However, the occurrence of Cu reduction reaction could reduce the calculated electron transfer number. Cu dissolved in the acidic electrolyte and the Cu oxides of sample (CuPt)50Ag30 were reduced during the ORR possibly skewing the electron transfer number towards 2. The best (Pt50Ag50) and the worst ((PtCu)50) performing catalysts in acid electrolyte were chosen to measure catalytic performance in 1 M KOH electrolyte. The results are shown in Figure 3.24. (CuPt)50Ag0 didn't dissolve in KOH, however, the onset potential (0.84 V) and electron transfer (n = 3.5) number of (CuPt)50Ag0 are still lower than that of Pt50Ag50 (0.88 V, n = 3.6).

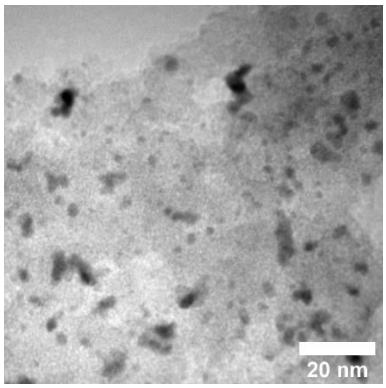

Figure 3.23 TEM image of commercial Pt/C reference catalyst. The average particle size is 3.5 ± 1.4 nm.

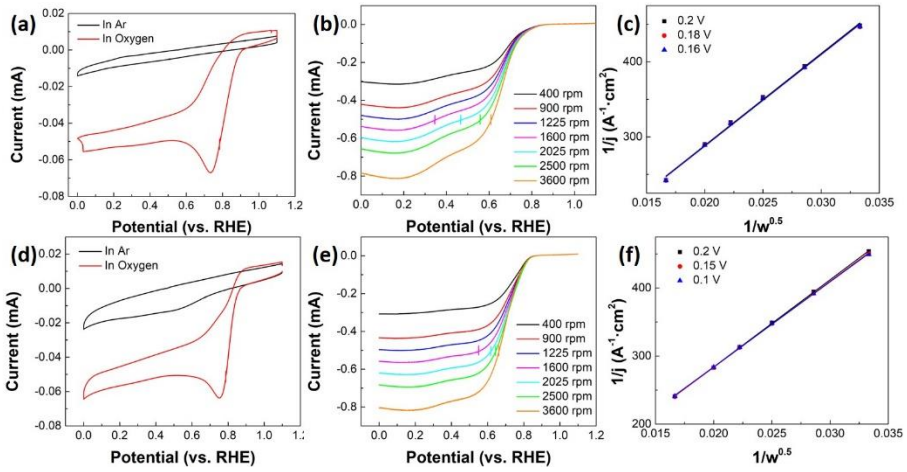

Figure 3.24 Electrochemical test results of Pt50Ag50/C (a, b, c) and (CuPt)50Ag0 (d, e, f) in 1 M KOH: (a, d) CV curves, (b, e) LSV curves, and (c, f) K-L plots.

So far, the detail mechanism of the ORR catalytic activity of the Ag/Pt alloy and CuPt/Ag NPs in our study is complicated, which is the topic for future study to address the contribution of electronic and geometrical structures, particle dispersion, alloy structure stability, and particle sizes on the catalytic performance.

3.4 Conclusion

Trimetallic CuPt/Ag alloy NPs were synthesized by co-sputtering onto liquid PEG using the CuPt alloy target and Ag target. The Ag compositions of NPs increase as the sputtering currents applied to the Ag target increase while the Cu : Pt molar ratios of NPs are lower than that of the CuPt alloy target. This is because the NPs with higher Cu compositions are too small to be detected by STEM-EDS area analysis, or some sputtered Cu atoms did not alloy with Ag and Pt. Thus the analyzed NPs that are bigger than 0.8 nm have lower Cu compositions. The trimetallic (CuPt)50Ag30 alloy NPs, bimetallic (CuPt)50Ag0 and Ag50Pt50 NPs, and Pt50 NPs were evaluated as ORR catalysts. Better catalytic activities of trimetallic (CuPt)50Ag30 NPs compared with bimetallic (CuPt)50Ag0 NPs came from better dispersion of the trimetallic NPs in the carbon support and a more stable alloying structure. However, bimetallic (CuPt)50Ag0 and trimetallic (CuPt)50Ag30 NPs performed worse than Pt50 and Ag50Pt50 NPs because of Cu oxidation. The synergy between Pt and Ag in the Ag50Pt50 alloy NPs is thought to enhance the catalytic properties of the bimetallic alloy NPs compared with only Pt NPs.

3.5 References

1 I. Y. Cha, M. Ahn, S. J. Yoo and Y. Sung, *RSC Adv.*, **2014**, *4*, 38575-38580.

2 B. R. Cuenya, *Thin Solid Films*, **2010**, *518*, 3127-3150.

3 D. Du, Q. Geng, L. Ma, S. Ren, J. Li, W. Dong, Q. Hua, L. Fan, R. Shao, X. Wang, C. Li, Y. Yamauchi, *Chem. Sci.*, **2022**, *13*, 3819-3825.

4 C. Li, M. Lqbal, J. Lin, X. Luo, B. Jiang, V. Malgras, K. C. Wu, J. Kim, Y. Yamauchi, *Acc. Chem. Res.*, **2018**, *51*, 1764-1773.

5 C. Li, H. Tan, J. Lin, X. Luo, S. Wang, J. You, Y. Kang, Y. Bando, Y. Yamauchi, J. Kim, *Nanotoday*, **2018**, *21*, 91-105.

6 C. Li, B. Jiang, N. Miyamoto, J. H. Kim, V. Malgras, Y. Yamauchi, *J. Am. Chem. Soc.*, **2015**, *137*, 11558-11561.

7 C. Li, M. Lqbal, B. Jiang, Z. Wang, J. Kim, A. K. Nanjundan, A. E. Whitten, K. Wood, Y. Yamauchi, *Chem. Sci.*, **2019**, *10*, 4054-4061.

8 J. Li, H. Yin, Q. Geng, D. Du, L. Ma, L. Fan, Q. Hua, C. Li, *J. Mater. Chem. A*, **2022**, *10*, 6569-6575.

9 P. Song, H. Xu, B. Yan, J. Wang, F. Gao, Y. Zhang, Y. Shiraishi and Y. Du, *Inorg. Chem. Front.*, **2018**, *5*, 1174-1179.

10 G. Zhang, Z. Yang, W. Zhang, H. Hu, C. Wang, C. Huang and Y. Wang, *Nanoscale*, **2016**, *8*, 3075-3084.

11 L. Zheng, D. Yang, R. Chang, C. Wang, G. Zhang and S. Sun, *Nanoscale*, **2017**, *9*, 8918-8924.

12 Z. Li, Y. Li, C. He and P. K. Shen, *J. Mater. Chem. A*, **2017**, *5*, 23158-23169.

13 M. Zhu, M. T. Nguyen, Y. R. Chau, L. Deng and T. Yonezawa, *Langmuir*, **2021**, *37*, 6096-6105.

14 P. J. Kelly and R. D. Arnell, *Vacuum,* **2000**, *56*, 159-172.

15 H. Wender, P. Migowski, A. F. Feil, S. R. Teixeira and J. Dupont, *Coord. Chem. Rev.,* **2013**, *257*, 2468-2483.

16 G. Bräuer, B. Szyszka, M. Vergöhl and R. Bandorf, *Vacuum,* **2010**, *84*, 1354-1359.

17 O. K. Alexeeva and V. N. Fateev, *Int. J. Hydrogen Energy*, **2016**, *41*, 3373-3386.

18 M. T. Nguyen and T. Yonezawa, *Sci. Technol. Adv. Mater.*, **2018**, *19*, 883-898.

19 M. Wagener and B. Günther, *J. Magn. Magn. Mater.*, **1999**, *201*, 41-44.

20 T. Torimoto, K. Okazaki, T. Kiyama, K. Hirahara, N. Tanaka and S. Kuwabata, *Appl. Phys. Lett.,* **2006**, *89*, 243117.

21 Y. Oda, K. Hirano, K. Yoshii. S. Kuwabata, T. Torimoto and M. Miura, *Chem. Lett.,* **2010**, *39*, 1069-1071.

22 S. C. Hamm, R. Shankaran, V. Korampally, S. Bok, S. Praharaj, G. A. Baker, D. Robertson, B. D. Lee, S. Sengupta, K. Gangopadhyay and S. Gangopadhyay, *ACS Appl. Mater. Interfaces,* **2012**, *4*, 178-184.

23 K. Yoshii, K. Yamaji, T. Tsuda, H. Matsumoto, T. Sato, R. Izumi, T. Torimoto and S. Kuwabata, *J. Mater. Chem. A,* **2016**, *4*, 12152-12157.

24 K. Okazaki, T. Kiyama, K. Hirahara, N. Tanaka, S. Kuwabata and T. Torimoto, *Chem. Commun.,* **2008**, 691-693.

25 H. Wender, L. F. de Oliveira, A. F. Feil, E. Lissner, P. Mingowski, M. R. Meneghetti, S. R. Teixeira, and J. Dupont, *Chem. Commun.*, **2010**, *46*, 7019-7021.

26 Y. Hatakeyama, T. Morita, S. Takahashi, K. Onishi and K. Nishikawa, *J. Phys. Chem. C*, **2011**, *115*, 3279-3285.

27 M. T. Nguyen, L. Deng, and T. Yonezawa, *Soft Matter*, **2022**, *18*, 19-47.

28 Y. Ishida, A. Morita, T. Tokunaga, and T. Yonezawa, *Langmuir*, **2018**, *34*, 4024-4030.

29 Y. Ishida, R. Nakabayashi, R. D. Corpuz, and T. Yonezawa, *Colloids Surf. A*, **2017**, *518*, 25-29.

30 M. Porta, M. T. Nguyen, T. Tokunaga, Y. Ishida, W.-R. Liu, and T. Yonezawa, *Langmuir*, **2016**, *32*, 12159-12165.

31 Y. Ishida, I. Akita, T. Sumi, M. Matsubara, and T. Yonezawa, *Sci. Rep.*, **2016**, *6*, 29928.

32 Y. Ishida, R. D. Corpuz, and T. Yonezawa, *Acc. Chem. Res.*, **2017**, *50*, 2986-2995.

33 S. Suzuki, T. Suzuki, Y. Tomita, M. Hirano, K. Okazaki, S. Kuwabata and T. Torimoto, *CrystEngComm*, **2012**, *14*, 4922-4926.

34 M. Hirano, K. Enokida, K. Okazaki, S. Kuwabata, H. Yoshida and T. Torimoto, *Phys.Chem. Chem. Phys.*, **2013**, *15*, 7286-7294.

35 D. König, K. Richter, A. Siegel, A. Mudring and A. Ludwig, *Adv. Funct. Mater.*, **2014**, *24*, 2049–2056.

36 M. T. Nguyen, T. Yonezawa, Y. Wang and T. Tokunaga, *Mater. Lett.*, **2016**, *171*, 75-78.

37 A. Chauvin, A. Sergievskaya, A. E. Mel, A. Fucikova, C. A. Corrêa, J. Vesely, E. Duverger-Nédellec, D. Cornil, J. Cornil, P. Tessier, M. Dopita and S. Konstantinidis, *Nanotechnology*, **2020**, *31*, 455303.

38 L. Deng, M. T. Nguyen, J. Shi, Y. R. Chau, T. Tokunaga, M. Kudo, S. Matsumura, N. Hashimoto and T. Yonezawa, *Langmuir*, **2020**, *36*, 3004−3015.

39 L. Deng, M. T. Nguyen, S. Mei, T. Tokunaga, M. Kudo, M. Matsumura and T. Yonezawa, *Langmuir*, **2019**, *35*, 8418-8427.

40 M. T. Nguyen, H. Zhang, L. Deng, T. Tokunaga and T. Yonezawa, *Langmuir*, **2017**, *33*, 12389-12397.

41 Y. R. Chau, M. T. Nguyen, M. Zhu, A. Romier, T. Tokunaga and T. Yonezawa, *New J. Chem.*, **2020**, *44*, 4704-4712.

42 X. Cai, C. Liu, Y. Lu, Y. Zhong, K. Nie, J. Xu, X. Gao, X. Sun and S. Wang, *Nano-Micro Lett.*, **2017**, *9*, 48.

43 F. Kong, Z. Ren, M. N. Banis, L. Du, X. Zhou, G. Chen, L. Zhang, J. Li, S. Wang, M. Li, K. Doyle-Davis, Y. Ma, R. Li, A. Young, M. Markiewicz, Y. Tong, G. Yin, C. Du, J. Luo and X. Sun, *ACS Catal.*, **2020**, *10*, 4205-4214.

44 H. A. Gasteiger, S. S. Kocha, B. Sompalli and F. T. Wagner, *Appl. Catal. B*, **2005**, *56*, 9-35.

45 A. U. Nilekar, Y. Xu, J. Zhang, M. B. Vukmirovic, K. Sasaki, R. R. Adzic, M. Mavrikakis, *Topics in Catalysis*, **2007**, *46*, 276-284.

46 J. Luo, P. N. Njoki, Y. Lin, L. Wang, C. J. Zhong, *Electrochem. Commun.*, **2006**, *8*, 581–587.

47 C. Gümeci, Z. R. Li, D. J. Casadonte Jr., C. Korzeniewski, *J. Electrochem. Soc.*, **2012**, *159*, F35– F41.

48 C. Wang, M. Chi, G. Wang, D. van der Vliet, D. Li, K. More, H.-H. Wang, J. A. Schlueter, N. M. Markovic, V. R. Stamenkovic, *Adv. Funct. Mater.*, **2011**, *21*, 147 –152.

49 J. Sha, S. Paul, F. Dumeignil, R. Wojcieszak, *RSC Adv.*, **2019**, 9, 29888-29901.

50 M. Liu, F. Chi, J. Liu, F. Wang, *RSC Adv.*, **2016**, *6*, 62327-62335.

51 N. Toshima, T. Yonezawa, *New Journal of Chemistry*, **1998**, *22*, 1179-1201.

52 F. H. Lima, C. D. Sanches, E. A. Ticianelli, *Journal of The Electrochemical Society*, **2005**, *152*, A1466-A1473.

53 H. Liu, F. Ye, Q. Yao, H. Cao, J. Xie, J. Y. Lee, J. Yang, *Scientific Reports*, **2014**, *4*, 3969.

54 R. C. Sekol, X. Li, P. Cohen, G. Doubek, M. Carmo, A. D. Taylor, *Applied Catalysis B: Environmental*, **2013**, *138*, 285-293.

55 F. Qu, N. B. Li and H. Q. Luo, *J. Phys. Chem. C*, **2013**, *117*, 3548-3555.

56 A. Campos, N. Troc, E. Cottancin, M. Pellarin, H. Weissker, J. Lermé, M. Kociak and M. Hillenkamp, *Nature Phys.*, **2019**, *15*, 275-280.

57 S. Baset, H. Akbari, H. Zeynali and M. Shafie. *Dig. J. Nanomater. Biostructures*, **2011**, *6*, 709-716.

58 D. Nafday, S. Sarkar, P. Ayyub and T. Saha-Dasgupta. *ACS Nano,* **2018**, *12*, 7246-7252.

59 H. R. Colón-Mercado and B. N. Popov, *J. Power Sources,* **2006**, *155*, 253-263.

60 M. Watanabe, K. Tsurumi, T. Mizukami, T. Nakamura and P. Stonehart, *J. Electrochem. Soc.,* **1994**, *141*, 2659-2668.

61 F. J. Perez-Alonso, D. N. McCarthy, A. Nierhoff, P. Hernandez-Fernandez, C. Strebel, I. E. L. Stephens, J. H. Nielsen and I. Chorkendorff, *Angew. Chem. Int. Ed.,* **2012**, *51*, 4641-4643.

62 Y. Feng, G. Zhang, J. Ma, G. Liu, B. Xu, Phys. *Chem. Chem. Phys.*, **2011**, *13*, 3863-3872.

63 F. Ando, T. Gunji, T. Tanabe, I. Fukano, H. D. Abrun˜a, J. Wu, T. Ohsaka and F. Matsumoto, ACS Catal., 2021, 11, 9317–9332.

64 V. T. T. Ho, C. Pan, J. Rick, W. Su and B. Hwang, J. Am. Chem. Soc., 2011, 133, 11716–11724.

65 C. T. Campbell, Nat. Chem., 2012, 4, 597–598.

66 Q. Jia, S. Ghoshal, J. Li, W. Liang, G. Meng, H. Che, S. Zhang, Z. Ma and S. Mukerjee, J. Am. Chem. Soc., 2017, 139, 7893–7903.

67 W. Gao, Z. Zhang, M. Dou and F. Wang, ACS Catal., 2019, 9, 3278–3288.

68 F. B. Ometto, E. A. Carbonio, E´. Teixeira-Neto and H. M. Villullas, J. Mater. Chem. A, 2019, 7, 2075–2086.

69 C. Xu, J. Yang, E. Liu, Q. Jia, G. M. Veith, G. Nair, S. DiPietro, K. Sun, J. Chen, P. Pietrasz, Z. Lu, M. Jagner, K. K. Gath, S. Mukerjee and J. R. Waldecker, J. Power Sources, 2020, 451, 227709.

4. Synthesis of fluorescent Au alloy NPs by sputtering

4.1 Introduction

Au NPs have been extensively studied due to their high stability to oxidation, optical and size-correlated electronic properties.[1-3] Therefore, the Au NPs possess a wide range of applications such as sensing, optoelectronics, cellular labelling, and imaging.[4-6] The sensing of Au NPs is originated from the state-dependent surface plasmon resonance (SPR) absorption property, that is, SPR of Au NPs solutions shifts to longer wavelength when then NPs are in aggregated state.4 Another optical property of Au NPs, the fluorescence, has also attracted much interests. The fluorescent property of Au NPs is due to the quantum confinement effect,[7-9] thus the property can be controlled by adjusting the size and shape of the NPs.[6] After decades of development, Au NPs are able to be synthesized by several methods for better properties at present. For example, C. Huang et al. introduced different alkanethiols ligands onto the surfaces of the Au NPs with diameters of ~2.9 nm. By changing the chain length of the alkanethiols, the fluorescence wavelength of Au NPs can be controlled.[10] W. Chen et al. prepared glutathione-capped fluorescent Au NPs via a one-step synthesis method using Glutathione (GSH) as stabilizer and reducing agent. The prepared fluorescent Au NPs can be used as a fluorescence ‘‘turn-off’’ sensor for Cu^{2+} ion due to the high sensitivity and selectivity.[4]

However, despite of the development and improvement of synthesis for the fluorescent

Au NPs, the fluorescence Au alloy NPs are rarely studied.[11-14] Q. Luo et al. Rhodamine B (RB) modified silver/gold bimetal nanoparticles (RB-Ag/Au NPs), making it low-cost and highly sensitive and selective sensors towards organophosphorus pesticides (OPs).[11] However, the compositions, morphologies, and the size/composition-correlated fluorescent property of Au alloy NPs still remains to be studied.

Sputtering, as a simple and environmentally friendly physical synthesizing approach, is a promising method for fabricating NPs.[15,26] To make metal alloy NPs, co-sputtering employs two or more metal targets at the same time. The alloy production is not restricted by the difference in redox potentials of metals, and this process does not require harmful chemical reductants.[17-19] Furthermore, by modifying factors such as the relative location of the liquid substrate with regard to the target, the applied sputtering powers, and currents, the metal compositions of the alloy NPs may be regulated with high flexibility and diversity.

In this paper, Au mono- and bimetallic fluorescence NPs are synthesized by co-sputtering onto PEG with MUA. The structures and optical properties of resulted alloy NPs are characterized using TEM, UV-Vis, and PL. The size-related fluorescent property of the alloy NPs are investigated, and the fluorescence wavelength of the alloy NPs are measured and compared with the monometallic counterparts.

4.2 Experimental section

4.2.1 Materials

PEG (M. W. = 600, Junsei, Japan), Au target, Pt target, Ag target, transmission electron microscope (TEM) grids (Nisshin EM, Japan), and MUA.

4.2.2 Synthesis of fluorescent Au alloy NPs

Firstly, MUA was dissolved in 10 mL PEG. And then, the PEG with MUA was stirred under vacuum at 650 rpm in a flask in an oil bath for at least 2 h to remove water and gases; the temperature of the oil bath was set at 90 °C. After that the PEG with MUA was added into a petri dish with a diameter of 60 mm. The petri dish was then placed horizontally in the center of the sputtering vacuum chamber. A stirrer was put in the petri dish under the surface of PEG. To synthesize Au/Pt and Au/Ag alloy NPs, Au target and Pt (Ag) target were co-sputtered. The elemental ratios of the alloy NPs were controlled by adjusting the sputtering currents applied to Pt (Ag) target (0-50 mA) while keeping the electrical current applied to Au target constant at 50 mA. The center of the petri dish was located at a distance of 110 mm from the two metal targets. PEG was stirred at 80 rpm. After several times of vacuum and purging with inert Ar to remove O_2, the pressure of the vacuum chamber was kept at 2 Pa. Cooling ethanol of 4 °C was used for cooling the metal targets during sputtering. Before collecting the NPs, the metal targets were sputtered for 10 min to clean the surfaces. During cleaning, removable shutters were located in front of the metal targets and above the petri dish to prevent contamination from falling onto the PEG. The sputtering time was 30 min for collecting NPs in PEG. The sputtering system was

equipped with a thermocouple and a temperature-controlled system to keep the substrate temperature at 30 °C.

4.2.3 Characterization

UV-Vis spectra were collected immediately after sputtering deposition using a JASCO V-630 spectrophotometer and a quartz cuvette with an optical path of 1 mm. The baseline was collected using an empty quartz cuvette. The size and shape of the NPs were analyzed using TEM (JEOL JEM-2000FX, 200 kV) and scanning TEM (STEM, JEOL JEM-ARM200F, 200 kV and FEI Titan3 G2 60-300, 300 kV). Samples for TEM and STEM analysis were prepared by immersing TEM grids into NPs/PEG dispersions for 10 s, then immediately immersing the grids into ethanol for at least 20 min to remove excess PEG, and finally drying in air at room temperature for a few minutes. The size distributions were collected from TEM and STEM images by measuring approximately 150 particles in at least three different regions of the grid using ImageJ software. Area analysis using energy-dispersive X-ray spectroscopy (EDS) coupled with STEM (JEOL JEM-ARM200F) was carried out to verify the existence of CuPt/Ag alloy NPs and their compositions. The metal compositions of NPs/PEG dispersions and metal loading on carbon of the catalysts were obtained by Inductively Coupled Plasma-Atomic Emission Spectrometer (ICP-AES, Shimadzu ICPE-9000). For preparing the samples, aqua regia or nitric acid was added into 1 mg of NPs/PEG dispersion or 10 mg catalyst powders. Aqua regia was used to prepare samples for measuring Pt and Cu, and nitric acid was used to prepare samples for

measuring Ag. The mixtures were then kept for at least 30 min. After the metals were entirely dissolved, the mixtures were centrifuged, the precipitates were discarded, and the supernatants were diluted to 10 mL for ICP-AES measurements

4.3 Results and Discussion

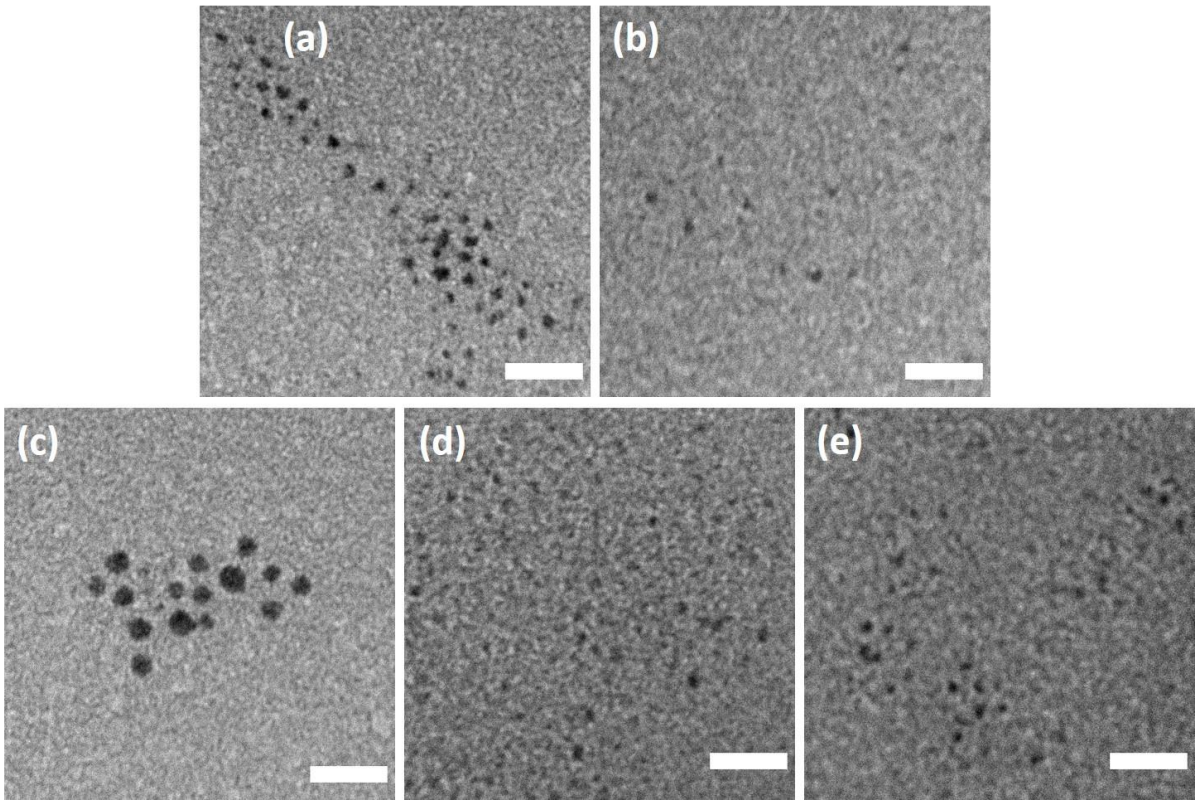

Figure 4.1 TEM images of the NPs sputtered onto MUA/PEG: (a) Au50, (b) Pt50, (c) Au50Pt10, (d) Au50Pt30 and (e) Au50Pt50. The scale bar is 10 nm.

In order to check the impact of sputtering current on the fluorescent property of the NPs, samples Au50, Pt50, Au50Pt10, Au50Pt30 and Au50Pt50 sputtered onto PEG with 50 mg MUA were synthesized by double-target system. Figure 4.1 shows the TEM images. The average particle sizes of Au50 (Figure 4.1 a) and Au50Pt50 (Figure

4.1 e) are both 1.6 ± 0.3 nm, and that of Au50Pt10 is 2.4 ± 0.7 nm. The NPs of samples Pt50 and Au50Pt30 (Figure 4.1 c and d) are too small to be checked the sizes. The NPs disperse in MUA/PEG, because the ligands surrounding NPs can prevent the agglomeration.

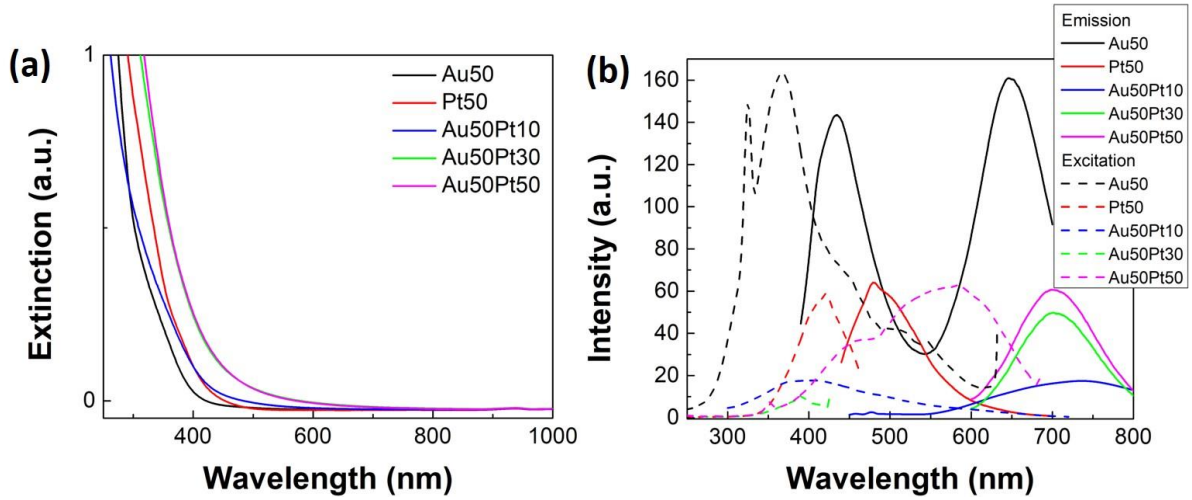

Figure 4.2 (a) UV-Vis spectra and (b) Emission and excitation spectra of monometallic Au, Pt, and alloy Au50Pt30, Au50Pt50 NPs sputtered onto MUA/PEG dispersions.

Table 4.1 Fluorescent peak position of the sputtered Au, Pt and AuPt alloy samples

Sample	Emission spectra		Excitation spectra	
	Ex (nm)	Emission peak (nm)	Em (nm)	Excitation peak (nm)
Au50	390	647	647	390
Pt50	420	480	480	420
Au50Pt10	420	744	744	420
Au50Pt30	580	700	700	580

Au50Pt50	580	700	700	580

The samples were measured UV-Vis, emission and excitation spectra to characterize the fluorescent property. Figure 4.2 a shows UV-Vis spectra of samples Au50, Pt50, Au50Pt10, Au50Pt30 and Au50Pt50 NPs sputtered onto MUA/PEG. There is no absorption peak observed in the spectra, as expected, so that the fluorescent spectra can be further measured. The emission peaks of the samples are 647, 480, 744, 700, 700 for Au50, Pt50, Au50Pt10, Au50Pt30 and Au50Pt50, respectively (Table 4.1). Notice that the emission peaks of Au50Pt30 and Au50Pt50 are located at the same position, this is consistent with the UV-Vis result that the spectra of these two samples overlap. On the other hand, the emission peak of sample Au50Pt10 is at 744 nm, longer than that of the other two alloy samples. Possible reason could be the bigger particle size of Au50Pt10, which can also be checked from TEM images (Figure 4.1 c-e). Compared to the monometallic Au and Pt NPs, the fluorescent peaks of the alloy Au/Pt NPs shift to longer wavelength, even though the particle sizes of Au50 and Au50Pt50 are the same. This result indicates the formation of Au/Pt alloy, and that the particle size is not the only factor to determine the emission wavelength. The instinct of alloy may also determine the fluorescent property of the samples, to some extent.

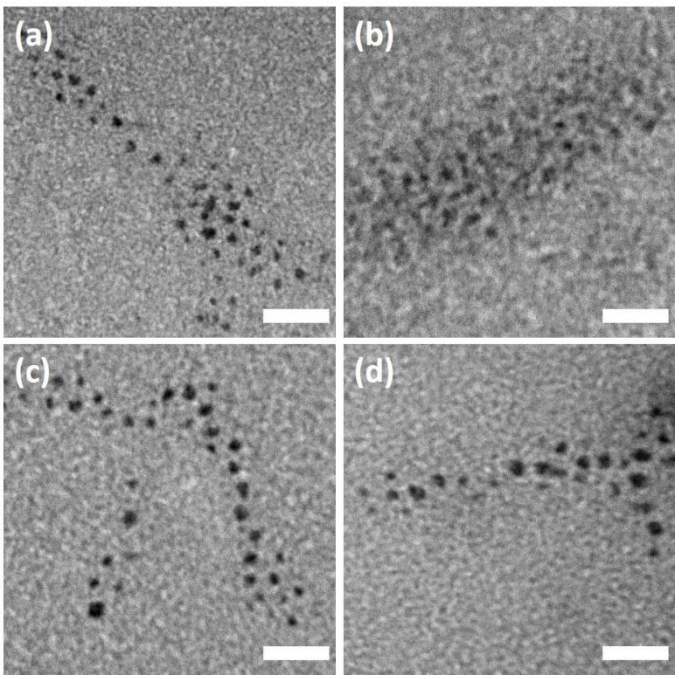

Figure 4.3 TEM images of the NPs sputtered onto PEG with 50 mg MUA: (a) Au50, (b) Ag50, (c) Au50Ag10, and (d) Au50Ag50. The scale bar is 10 nm.

In order to further verify the hypothesis of the fluorescent wavelength, the synthesis of AuAg alloy NPs sputtered onto PEG with 50 mg MUA was carried out. The TEM images of monometallic Au50 NPs, and alloy Au50Ag10, Au50Ag50 NPs are shown in Figure 4.3. The average particle sizes are 1.6 ± 0.3, 1.6 ± 0.5, and 1.9 ± 0.5 nm for Au50, Au50Ag10 and Au50Ag50, respectively. The Ag50 NPs are very small (Figure 4.3 b) and aggregated, thus the particle size of this sample was not measured. The size distributions of Au/Ag alloy NPs are shown in Figure 4.4.

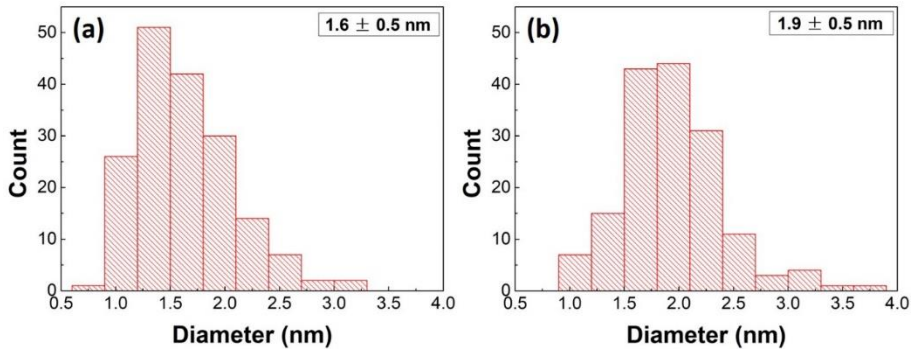

Figure 4.4 Size distributions of Au/Ag alloy NPs sputtered onto PEG with 50 mg MUA: (a) Au50Ag10, (b) Au50Ag50.

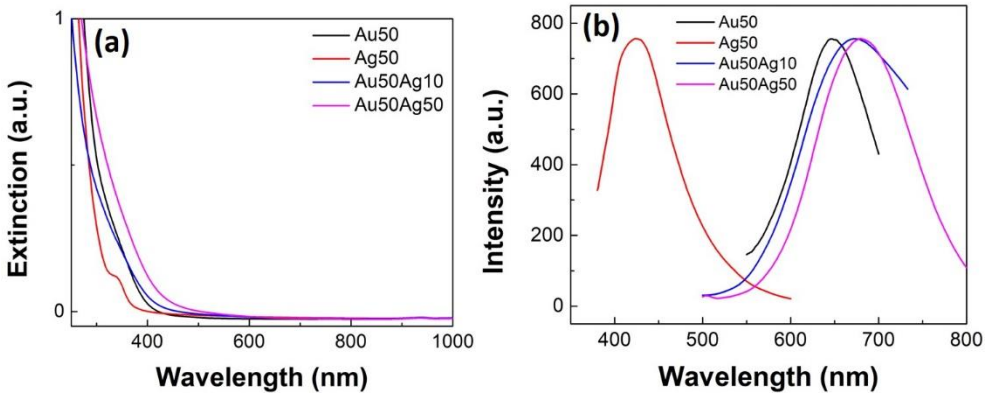

Figure 4.5 (a) UV-Vis spectra and (b) Normalized fluorescent spectra of samples Au50, Ag50, Au50Ag10 and Au50Ag50 sputtered onto PEG with 50 mg MUA.

Table 4.2 Fluorescent peak position of the sputtered Au, Ag and AuAg alloy samples

Sample	Emission spectra		Excitation spectra	
	Ex (nm)	Emission peak (nm)	Em (nm)	Excitation peak (nm)
Au50	390	647	647	390
Ag50	360	423	423	360

Au50Ag10	374	674	674	374
Au50Ag50	440	680	680	440

Figure 4.5 illustrates the UV-Vis spectra and normalized emission spectra of samples Au50, Ag50, Au50Ag10 and Au50Ag50. The vibration of a group of free electrons in the surface region of NPs causes surface plasmon absorption, which has an absorption peak matching to their vibration frequency. As a result, plasmon absorption requires a specific particle size to be generated.[21] In Figure 4.5 a, Au50 and Au/Ag alloy NPs don't show absorption peak, as expected. And an absorption shoulder appears at ~350 nm in the spectrum of sample Ag50 due to the existence of very small Ag NPs or clusters[21,22]. On the other hand, the disappearance of this absorption shoulder in samples Au50Ag10 and Au50Ag50 preliminarily proves the formation of the alloy.

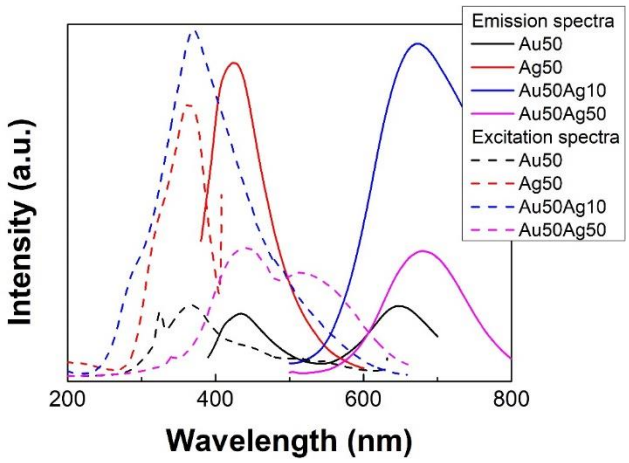

Figure 4.6 Emission and excitation spectra of Au50, Ag50, Au50Ag10 and Au50Ag50.

The emission and excitation spectra before normalization are shown in Figure 4.6, and the emission peak positions are listed in Table 4.2. The emission peaks of alloy Au/Ag NPs are at 674 and 680 nm, longer than monometallic Au50 (647 nm) and Ag50 (423 nm). This result is consistent with the situation of Au/Pt alloy NPs. As for bimetallic Au/Ag alloy NPs, the emission peak wavelength of Au50Ag50 is found to be longer than that of Au50Ag10, which is reasonable because the average particle size of Au50Ag50 (1.9 nm) is bigger than that of Au50Ag10 (1.6 nm). However, the particle sizes of Au50 and Au50Ag10 NPs are the same, whereas the emission wavelength of these samples still shows obvious difference. The fluorescent results of Au/Ag alloy NPs are similar to that of Au/Pt alloy NPs, further demonstrates the hypothesis that the particle size and the instinct of alloy together determine the fluorescent properties.

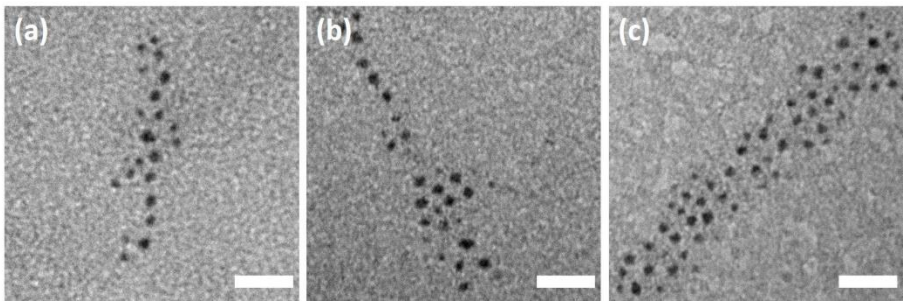

Figure 4.7 TEM images of Au50Ag50 NPs sputtered onto PEG with (a) 50 mg MUA, (b) 100 mg MUA, (c) 500 mg MUA. The scale bar is 10 nm.

Except for the alloy and size effects on the fluorescent properties of sputtered NPs, the relationship between the amount of MUA and fluorescent peak wavelength is also investigated. As is known to all, the fluorescent peak of monometallic NPs originates

from quantum size effect[23], thus the peak shift in fluorescence corresponds to the particle sizes. However, whether this conclusion works for the alloy NPs still remains unknown. So the sample Au50Ag50 was chosen to sputtered onto PEG with different amount of MUA and the fluorescent properties are characterized. Figure 4.7 shows the TEM images of the sputtered Au50Ag50 NPs onto PEG with 50, 100 and 500 mg of MUA. The size distributions of the samples are presented in Figure 4.8. The particle sizes of the Au50Ag50 NPs are measured to be 1.9 ± 0.5 nm, 1.8 ± 0.3 nm, and 1.6 ± 0.3 nm for the samples sputtered onto PEG with 50 mg, 100 mg and 500 mg MUA, respectively. As the amount of MUA in PEG increases, the particle size of Au50Ag50 NPs decreases with narrower size distributions, indicating more uniformed particle sizes. This is because the MUA can suppress the aggregation of the NPs.[6,22]

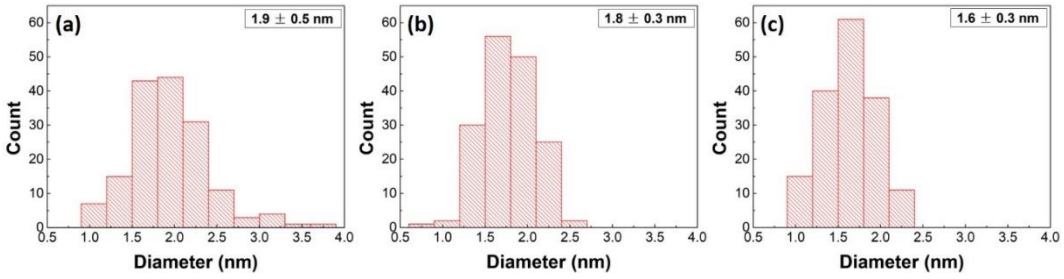

Figure 4.8 Size distributions of Au50Ag50 NPs sputtered onto PEG with (a) 50 mg MUA, (b) 100 mg MUA, (c) 500 mg MUA.

The optical properties of the samples are also characterized to study the impact of the amount of MUA. Figure 4.9 illustrates the UV-Vis spectra and fluorescent spectra of the Au50Ag50 NPs sputtered onto PEG with different amount of MUA. The excitation wavelength and emission peak positions are listed in Table 4.3.

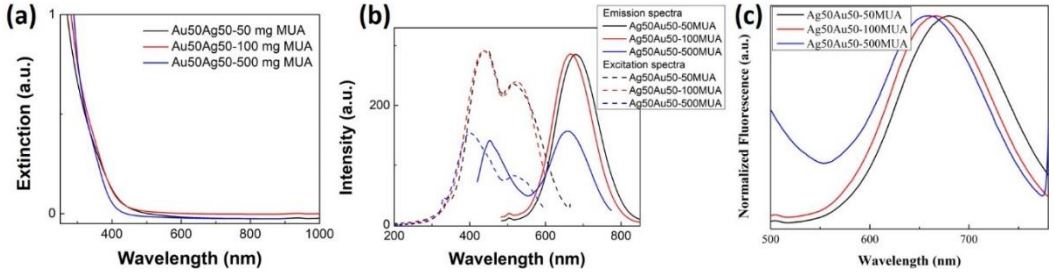

Figure 4.9 (a) UV-Vis spectra, (b) Emission and excitation spectra, and (c) Normalized emission spectra of Au50Ag50 NPs sputtered onto PEG with 50, 100 and 500 mg MUA.

Table 4.3 Fluorescent peak position of the sputtered Au50Ag50 NPs in PEG with different amount of MUA

Amount of MUA	Ex (nm)	Emission peak wavelength (nm)
50 mg	440	680
100 mg	440	665
500 mg	400	658

In Figure 4.9 a, there is no absorption peak in the UV-Vis spectra, because of the small particle sizes. Figure 4.9 c shows the normalized emission spectra of the samples, the emission peak positions are 680 nm, 665 nm, and 658 nm for Au50Ag50 sputtered onto PEG with MUA of 50, 100 and 500 mg, respectively. It's obvious that the emission spectra of the sputtered Au/Ag NPs show blue shift with the increase of

MUA amount. That is, the spectra shift to shorter wavelength as the particle size decreases. This result reveals that the quantum size effect still works for alloy NPs.

Furthermore, the different Au alloy with the same particles, Au50Pt50 alloy NPs sputtered onto PEG with 50 mg MUA, and Au50Ag50 alloy NPs sputtered onto PEG with 500 mg MUA, are also compared. The particle sizes of these two samples are both 1.6 ± 0.3 nm, however, the fluorescent wavelengths of the samples are different (700 nm for Au50Pt50 and 658 nm for Au50Ag50). The difference of fluorescent spectra also suggests that the particle sizes and the instinct of alloy together depend the fluorescent properties, which is consistent with the results above.

4.4 Conclusion

Au, Ag and Pt monometallic and Au/Pt, Au/Ag bimetallic alloy NPs are synthesized by sputtering onto liquid PEG with 50 mg MUA. And Au/Ag samples are sputtered onto PEG with different amount of MUA. It's concluded that not only monometallic NPs, but also alloy NPs have size-dependent fluorescent properties due to the quantum size effect. Apart from this, the fluorescent properties are also found to be related to the instinct of alloy by comparing the different kinds of Au alloy. And the bimetallic alloy NPs usually possess longer fluorescence wavelengths when compared to the single-metal NPs of which they are composed.

4.5 References

1. N. Zhang, Y. Liu, L. Tong, K. Xu, L. Zhuo, B. Tang. A novel assembly of Au NPs–b-CDs–FL for the fluorescent probing of cholesterol and its application in blood serum. *Analyst* **2008**, *133*, 1176-1181.
2. E. Oh, M.-Y. Hong, D. Lee, S.-H. Nam, H. C. Yoon and H.-S. Kim. Inhibition Assay of Biomolecules based on Fluorescence Resonance Energy Transfer (FRET) between Quantum Dots and Gold Nanoparticles. *J. Am. Chem. Soc.* **2005**, *127*, 3270-3271.
3. 9 R. Hong, G. Han, J. M. Fernandez, B.-j Kim, N. S. Forbes and V. M. Rotello. Glutathione-Mediated Delivery and Release Using Monolayer Protected Nanoparticle Carriers. *J. Am. Chem. Soc.* **2006**, *128*, 1078-1079.
4. W. Chen, X. Tu, X. Guo. Fluorescent gold nanoparticles-based fluorescence sensor for Cu^{2+} ions. *Chem. Commun.* **2009**, 1736-1738.
5. G. Yue, S. Su, N. Li, M. Shuai, X. Lai, D. Astruc, P. Zhao. Gold nanoparticles as sensors in the colorimetric and fluorescence detection of chemical warfare agents. *Coordination Chemistry Reviews* **2016**, *311*, 75-84.
6. Y. Ishida, I. Akita, T. Sumi, M. Matsubara, T. Yonezawa. Thiolate–Protected Gold Nanoparticles Via Physical Approach: Unusual Structural and Photophysical Characteristics. *Scientific reports* **2016**, *6*, 29928.
7. N. Schaeffer, B. Tan, C. Dickinson, M. J. Rosseinsky, A. Laromaine, D. W. McComb, M. M. Stevens, Y. Wang, L. Petit, C. Barentin, D. G. Spiller, A. I. Cooper, R. Lévy. Fluorescent or not? Size-dependent fluorescence switching for polymer-

stabilized gold clusters in the 1.1–1.7 nm size range. *Chem. Commun.* **2008**, 3986-3988.

8. Z. Wu, R. Jin. On the Ligand's Role in the Fluorescence of Gold Nanoclusters. *Nano Lett.* **2010**, *10*, 2568-2573.
9. G. Wang, R. Guo, G. Kalyuzhny, J. Choi, R. W. Murray. NIR Luminescence Intensities Increase Linearly with Proportion of Polar Thiolate Ligands in Protecting Monolayers of Au38 and Au140 Quantum Dots. *J. Phys. Chem. B* **2006**, *110*, 20282-20289.
10. C. Huang, Z. Yang, K. Lee, H. Chang. Synthesis of Highly Fluorescent Gold Nanoparticles for Sensing Mercury(II). *Angew. Chem.* **2007**, *119*, 6948-6952.
11. Q. Luo, J. Lai, P. Qiu, X. Wang. An ultrasensitive fluorescent sensor for organophosphorus pesticides detection based on RB-Ag/Au bimetallic nanoparticles. *Sensors and Actuators B: Chemical* **2018**, *263*, 517-523.
12. C. Wang, W. Chen, H. Chang. Enzyme Mimics of Au/Ag Nanoparticles for Fluorescent Detection of Acetylcholine. *Anal. Chem.* **2012**, *84*, 9706-9712.
13. M. N. Alam, S. Das, S. Batuta, D. Mandal, N. A. Begum. Green-nanochemistry for safe environment: bio-friendly synthesis of fluorescent monometallic (Ag and Au) and bimetallic (Ag/Au alloy) nanoparticles having pesticide sensing activity. *Journal of Nanostructure in Chemistry* **2016**, *6*, 373-395.
14. T. Som, B. Karmakar. Core-shell Au-Ag nanoparticles in dielectric nanocomposites with plasmon-enhanced fluorescence: A new paradigm in antimony glasses. *Nano Research* **2009**, *2*, 607-616.

15. M. T. Nguyen, T. Yonezawa. Sputtering onto a liquid: interesting physical preparation method for multi-metallic nanoparticles. *Sci. Technol. Adv. Mater.* **2018**, *19*, 883-898.

16. C. Liu, X. Chen, Y. Hu, T. Sham, Q. Sun, J. Chang, X. Gao, X. Sun, S. Wang. One-Pot Environmentally Friendly Approach toward Highly Catalytically Active Bimetal-Nanoparticle-Graphene Hybrids. *ACS Appl. Mater. Interfaces* **2013**, *5*, 5072-5079.

17. M. Hirano, K. Enokida, K. Okazaki, S. Kuwabata, H. Yoshida, T. Torimoto. Composition-dependent electrocatalytic activity of AuPd alloy nanoparticles prepared via simultaneous sputter deposition into an ionic liquid. *Phys.Chem. Chem. Phys.* **2013**, *15*, 7286-7294.

18. D. König, K. Richter, A. Siegel, A. Mudring, A. Ludwig. High-Throughput Fabrication of Au–Cu Nanoparticle Libraries by Combinatorial Sputtering in Ionic Liquids. *Adv. Funct. Mater.* **2014**, *24*, 2049-2056.

19. M. T. Nguyen, T. Yonezawa, Y. Wang, T. Tokunaga. Double target sputtering into liquid: A new approach for preparation of Ag–Au alloy nanoparticles. *Mater. Lett.* **2016**, *171*, 75-78.

20. Dass. Faradaurate Nanomolecules: A Superstable Plasmonic 76.3 kDa Cluster. *J. Am. Chem. Soc.* **2011**, *133*, 19259-19261.

21. Y. Ishida, R. Nakabayashi, R. D. Corpuz, T. Yonezawa. Water-dispersible fluorescent silver nanoparticles via sputtering deposition over liquid polymer using a very short thiol ligand. *Colloids and Surfaces A: Physicochem. Eng. Aspects* **2017**,

518, 25-29.

22. Y. Ishida, R. Nakabayashi, M. Matsubara, T. Yonezawa. Silver sputtering into a liquid matrix containing mercaptans: the systematic size control of silver nanoparticles in single nanometer-orders. *New J. Chem.* **2015**, *39*, 4227-4230.
23. J. A. Mclean, K. A. Stumpo, D. H. Russell. Size-Selected (2−10 nm) Gold Nanoparticles for Matrix Assisted Laser Desorption Ionization of Peptides. *J. Am. Chem. Soc.* **2005**, *127*, 5304-5305.

5 General conclusions

Sputtering is a conventional physical method for fabricating thin films on solid substrates. During decades, sputtering has been developed for wider applications, and not limited in the generation of thin films. The sputtering substrates have also realized the development from solid to liquid. Therefore, synthesizing metal NPs through sputtering onto liquid substrates has become a common and facile approach without using of toxic reductants and free of production of by-products. The synthesized NPs can also be utilized in variety of applications. The key results and conclusions can be summarized as follows:

Chapter Two used Pt and Ag metal targets to synthesize Pt/Ag alloy NPs by co-sputtering method via a double-target system. And the generated Pt/Ag alloy NPs are proved to be solid solution formation. The sputtering currents applied to the targets were found to have no impact on particle size, but it's related to the compositions of the alloy NPs, which was reflected in the XRD patterns, and confirmed by the composition and composition distributions of the Pt/Ag NPs. The size and composition distributions of the NPs co-sputtered on glass slides were more uniform than that co-sputtered onto PEG. This is because PEG hindered NPs from growing to larger sizes, which led to the broader size distributions of the NPs sputtered onto PEG. Moreover, the alloy NPs formed at the beginning of sputtering, and they continue to grow and combine with other atoms/clusters after deposition. The interaction between PEG and the NPs also contributed to the broader composition distributions of the NPs sputtered onto PEG than that on glass slides.

Chapter Three focus on the synthesis of trimetallic CuPt/Ag alloy NPs by applying a Cu/Pt alloy target and an Ag target via co-sputtering method. The compositions of alloy NPs were controlled by changing the sputtering currents applied to the targets. Ag compositions of the NPs increased with the increase of Ag sputtering currents, however, the Cu:Pt molar ratios in the NPs were lower than that in Cu/Pt alloy target. Possible reason could be the small particle sizes of the alloy NPs with higher Cu compositions that were no able to be detected by STEM-EDS area analysis, or some sputtered Cu didn't combine with Ag and Pt. The co-sputtered trimetallic CuPt/Ag alloy NPs were applied as catalyst in ORR and compared with monometallic Pt NPs, bimetallic Pt/Ag and Pt/Cu alloy NPs. It was found that the oxidation of Cu and dissolution of Pt and Cu decreased catalytic performance of samples (CuPt)50Ag0 and (CuPt)50Ag30. However, the synergy between Pt and Ag in samples (CuPt)50Ag30 and Pt50Ag50 was confirmed to enhance the catalytic activity of the alloy NPs.

Chapter Four prepared Au, Pt, Ag monometallic NPs and Au/Pt, Au/Ag bimetallic alloy NPs by sputtering onto PEG with MUA dispersed. This method successfully synthesized fluorescent mono- and bimetallic alloy NPs. By checking the optical properties of resulted NPs, it was found that the fluorescence wavelengths of the Au alloy NPs were longer than their monometallic counterparts. Within the same alloy NPs, the fluorescence wavelength can be dependent by the particle size, but when the particle sizes of the alloy NPs are the same, the sputtering currents applied to the targets didn't have obvious impact on the fluorescence wavelength.

Acknowledgements

During the past three years, I have received so many helps without witch I couldn't have reached this point. Therefore, I would like to express my sincere gratitude to the people who have helped me.

Professor Tetsu Yonezawa guided me to this laboratory, and has given me many supports. I can still remember the first day when I visited him, he showed me around the lab while explaining the experiments and instruments for me. He also introduced the weather and traffic of Sapporo, and advised me to prepare a pair of waterproof and non-slip shoes for the snowy days. Thanks to his advice, I was spared a lot of pain during the winters in Sapporo. In my research, every time when I encountered difficulties, Professor Yonezawa could always give the proper guidance to solve the problem. It's my honor to be a student of Yonezawa's group.

I also want to thank my assistant professor, Nguyen Thanh Mai, for her teaching and help. I have acquired much knowledge about experiments and characterization with her help, and she also taught me how to do research. I could always turn to her for help no matter what kind of problems I encountered. Even though sometimes she was busy, she listened to my problems with patience, to which I am grateful. I also have many thanks to our assistant professor, Yohei Ishida. His help and encouragement are cheerful, I will never forget.

My lab mates, Dr. DENG Lianlian, Dr. HUANG Zhong, Dr. ZHU Shilei, Dr. LIU Haoran and etc., gave me comfort when I feel difficult, and sincerely considered for

me all the time. Their supports helped me to get through the dark and reached the lights. It's lucky to have spent the short but precious time with them.

Thanks to my parents and family members for their supports and understanding, so that I can concentrate on pursuing my dreams. Their selfless love is what keeps me moving forward and gives me the courage to be fearless.

I would like to thank the Ministry of Education, Culture, Sports, Science and Technology-Japan (MEXT) for financial support for my stay in Sapporo.

Finally, for me. The experiences during the past three years have taught me a lot and made me grow. All the happiness, sadness and pains I experienced make up the person I am now. Thanks to time and the past, I have more confidence to step into the future.

List of publications

1st Author

1. M. Zhu, M. T. Nguyen, Y. R. Chau, L. Deng, T. Yonezawa. Pt/Ag Solid Solution Alloy Nanoparticles in Miscibility Gaps Synthesized by Cosputtering onto Liquid Polymers. *Langmuir* **2021**, *37*, 6096−6105.
2. M. Zhu, M. T. Nguyen, Wei Jian Sim, T. Yonezawa. Co-sputtered CuPt/Ag alloy nanoparticles and comparative catalytic performance of mono-, bi-, and tri-metallic nanoparticles in oxygen reduction reaction. *Mater. Adv.* **2022**, *3*, 8967-8976.

Co-Authored

1. Y. R. Chau, M. T. Nguyen, M. Zhu, A. Romier, T. Tokunaga, T. Yonezawa. Synthesis of composition-tunable Pd–Cu alloy nanoparticles by double target sputtering. *New J. Chem.* **2020**, *44*, 4704-4712.

List of conferences

Conference	Date	Title
第 56 回 応用物理学会北海道支部	January 9, 2021	Pt/Ag solid solution alloy nanoparticles synthesized by co sputtering onto liquid polymer
日本化学会北海道支部 2021 年夏季研究発表会	July 17, 2021	Composition controllable Pt/Ag alloy nanoparticles synthesized by co-sputtering onto liquid polymer
The 72nd Divisional Meeting of Division of Colloid and Surface Chemistry	September 21, 2021	Synthesis of Pt/Ag solid solution alloy nanoparticles on liquid polymer by co-sputtering
IVC-22	September, 2022	Pt/Ag Solid Solution Alloy Nanoparticles Co-sputtered onto Liquid Polyethylene Glycol Substrate